# Cooper pairing and fluctuations in Fe-based superconductors

Dissertation
Daniel Jost

Advisor: Priv.-Doz. Dr. Rudolf Hackl
Garching, October 2019

Technische Universität München

TECHNISCHE UNIVERSITÄT MÜNCHEN

Fakultät für Physik
Lehrstuhl E23 für Technische Physik

Walther-Meißner-Institut für Tieftemperaturforschung
der Bayerischen Akademie der Wissenschaften

# Cooper pairing and fluctuations in Fe-based superconductors

Daniel Jost

Vollständiger Abdruck der von der Fakultät für Physik der Technischen
Universität München zur Erlangung des akademischen Grades eines

**Doktors der Naturwissenschaften**

genehmigten Dissertation.

| | | |
|---|---|---|
| Vorsitzender: | | Prof. Dr. Wilhelm Zwerger |
| Prüfer der Dissertation: | 1. | Priv.-Doz. Dr. Rudolf Hackl |
| | 2. | Prof. Dr. Peter Böni |

Die Dissertation wurde am 30.10.2019 bei der Technischen Universität München
eingereicht und durch die Fakultät für Physik am 12.12.2019 angenommen.

# Abstract

Unconventional superconductivity generally occurs in proximity to magnetic phases. Raman spectroscopy affords a window into most of the related excitations including pairing interactions. Thus, the superconducting ground state and putative sub-leading pairing tendencies can be probed along with magnetic excitations and fluctuations. Here, Raman spectroscopy identifies the hierarchy of pairing channels in $\mathrm{CaKFe_4As_4}$ and critical fluctuations in $\mathrm{Ba(Fe_{1-x}Co_x)_2As_2}$. The fluctuations are analysed using a novel method tailored for the low energy Raman response.

# Kurzzusammenfassung

Supraleitung in Hochtemperatursupraleitern könnte durch eine Vielzahl ineinadergreifender Mechansimen entstehen. Ramanspektroskopie stellt eine Möglichkeit dar diese Mechanismen zu untersuchen: einerseits durch die direkte Untersuchung des supraleitenden Grundzustands und andererseits durch die Messung von kritischen Fluktuationen. Diese Arbeit zeigt die Vielseitigkeit der Ramanspektroskopie auf, indem ein subdominanter Paarungskanal in $\mathrm{CaKFe_4As_4}$ und quantenkritische Fluktuationen in $\mathrm{Ba(Fe_{1-x}Co_x)_2As_2}$ identifiziert werden. Zusätzlich wird eine neue Methode zur Analyse des Niedrigfrequenz-Ramanspektrums der Fluktuationen präsentiert.

# Contents

# Chapter 1

# Introduction

*If it turns out it's like an onion with millions of layers and we're just sick and tired of looking at the layers, then that's the way it is, but whatever way it comes out, its nature is there and she's going to come out the way she is, and therefore when we go to investigate it we shouldn't predecide what it is we're trying to do except to try to find out more about it.*

R. P. Feynman [1]

The discovery of LaOFeP in 2006 [2] marked the beginning of the "iron-age of superconductivity" [3]. The Fe-based superconductors (FeSC) exhibit high transition temperatures $T_\mathrm{c}$ [4–9] similar to the cuprates [10, 11]. However, the mechanisms behind superconductivity in the FeSC are not entirely disentangled. To reveal these mechanisms one usually tries to pin down the symmetry of the superconducting order parameter and the momentum dependence of the gap function $\Delta_\mathbf{k}$ first [12]. In the early stages of the FeSC, the order parameter was quickly proposed to have $s^\pm$ symmetry [12–15] in which superconductivity is mediated by spin fluctuations. Yet, at the same time, it was suggested, that such an $s^\pm$ ground state may be competing with $d$-wave pairing [16–18], thereby painting a more intricate picture.

The investigation into these pairing mechanisms is facilitated by the wealth of different phase transitions which one can generate by chemical substitution [4,19]. For instance $BaFe_2As_2$ [20] exhibits a magneto-structural transition at $T_\mathrm{s} = 135\,\mathrm{K}$. Upon substituting Fe with Co [21], the two transitions split giving rise to a nematic phase with a structural distortion and a magnetic spin-density-wave transition [22]. Further doping destabilises these transitions and superconductivity emerges.

This concomitant doping dependence is observed in K doped $Ba_{1-x}K_xFe_2As_2$ as well where the magneto-structural transition temperature decreases and superconductivity develops [4,19]. $Ba_{1-x}K_xFe_2As_2$ represents an interesting case study due to the anisotropy of its pairing potential [23,24] which highlights the aforementioned intricacies of the Cooper pairing in the FeSC. In $Ba_{1-x}K_xFe_2As_2$ the ground state is most likely dominated by an interaction having $s^{\pm}$-symmetry [25,26]. Additionally, spectroscopic fingerprints of competing interactions with $d$-wave symmetry were detected [24,27,28] revealing a hierarchy of pairing channels. It is not clear, if these subdominant pairing channels are a generic feature of FeSC with a dominant $s^{\pm}$ ground state as theoretically argued [16–18] or unique to $Ba_{1-x}K_xFe_2As_2$. To test this experimentally, the stoichiometric $CaKFe_4As_4$ [29] proves to be a good candidate due to its similarities with optimally doped $Ba_{1-x}K_xFe_2As_2$ [30] including possibly the $s^{\pm}$-symmetry of the superconducting ground state [30–32]. $CaKFe_4As_4$ belongs to the recently discovered 1144-$AeA$$Fe_4As_4$ compounds with $Ae$ = Ca, Sr and $A$ =K, Rb, Cs having superconducting transition temperatures around 35 K [29].

Superconductivity in $CaKFe_4As_4$ may not be influenced by an $s^{\pm}$ interaction only. One can substitute Fe with Ni which yields $CaK(Fe_{1-x}Ni_x)_4As_4$ [33]. Here, a putative magnetic quantum critical point (QCP) was found [34] close to $x = 0$ which may affect the superconducting pairing [35]. The investigation of a QCP is challenging due to its nature as a second-order phase transition at $T = 0\,K$ [36]. Thus, investigating a QCP itself is possible only via the observation of the associated critical fluctuations which may play a role in mediating the pairing [35] or enhancing $T_c$ [37]. Such fluctuations leading up to a QCP have been discussed to exist in $Ba(Fe_{1-x}Co_x)_2As_2$ as well [38,39] but these findings were subsequently called into question [40,41].

This leaves us with the two objectives of this thesis: (i) answering the question, if subleading pairing channels are observable in compounds other than $Ba_{1-x}K_xFe_2As_2$, and (ii) if it is possible to make a case for a QCP in $Ba(Fe_{1-x}Co_x)_2As_2$ after all. To this end, the inelastic scattering of light (Raman spectroscopy) is utilised. Raman spectroscopy provides access to the energy and symmetry of the subleading interactions in the superconducting state [24,27,42] on the one hand. On the other, critical fluctuations and magnetic excitations can be probed [43,44].

This thesis is structured as follows: Chapter 2 presents the material class of the FeSC with an emphasis on the doped $BaFe_2As_2$ compounds and the stoichiometric $CaKFe_4As_4$. Chapter 3 introduces the method of inelastic light (Raman) scattering. Chapter 4 shows the experimental setup used for the Raman scattering experiments. The characterisation of the samples is described and an overview of the measured samples is given. Chapter 5 expands on the work in Ref. [45], arguing in favour of a subleading interaction in $CaKFe_4As_4$. Chapter 6 discusses the evolution from thermal to quantum fluctuations in $Ba(Fe_{1-x}Co_x)_2As_2$. A summary is given in chapter 7.

# Chapter 2

# The iron-based superconductors

The following chapter gives an overview over the FeSC, and in particular the doped $BaFe_2As_2$ [20] and stoichiometric $CaKFe_4As_4$ [29] compounds. It places the properties of $CaKFe_4As_4$ alongside those of K-doped $Ba_{1-x}K_xFe_2As_2$ [4] on the one hand and Co-doped $Ba(Fe_{1-x}Co_x)_2As_2$ [21] on the other, introducing the three main actors of this thesis.

## 2.1 Crystallography - unit cells and Brillouin zone

$CaKFe_4As_4$ and $BaFe_2As_2$ share the $D_{4h}$ point group of the tetragonal lattice. Fig. 2.1 shows the crystallographic unit cells next to each other. The tetragonal unit cell of the $BaFe_2As_2$ is made up of Ba atoms at the corner and in the centre separating the Fe-As layers. Superconductivity emerges, if, for instance, the Fe atoms are replaced by Co in $Ba(Fe_{1-x}Co_x)_2As_2$ [21] which is akin to electron doping or Ba atoms are replaced by potassium giving rise to hole doped $Ba_{1-x}K_xFe_2As_2$ [4]. These replacements take up equivalent crystallographic sites preserving the $I4/mmm$ space group [29] as the atomic radii between Ba and K or Fe and Co do not deviate substantially from each other[1].

---

[1] The deviations between the radii are of the order of $\sim 5\,\text{pm}$: $r_{\text{Ba}} = 215$ pm, $r_{\text{K}} = 220$ pm; $r_{\text{Co}} = 140$ pm, $r_{\text{Fe}} = 135$ pm. From Ref. [46].

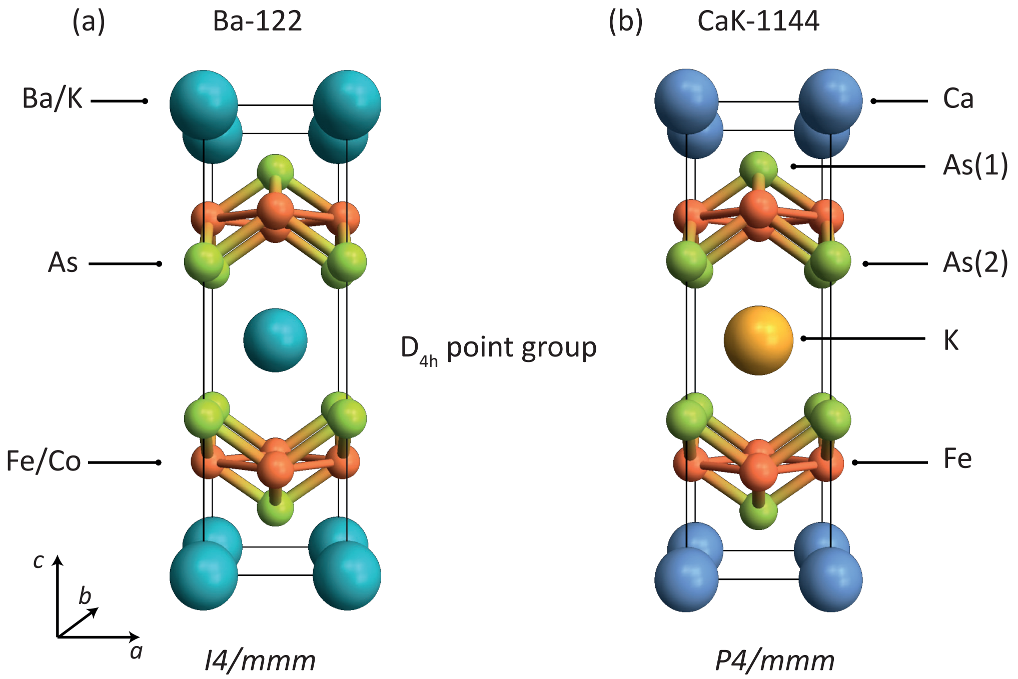

Figure 2.1: Tetragonal unit cells of $BaFe_2As_2$ and $CaKFe_4As_4$ as indicated. (a) The Ba atoms (cyan) occupy the corners as well as the centre of the unit cell. The Fe (red) and As (green) atoms of the Fe-As layers in the a-b plane. Ba (Fe) atoms can be randomly replaced by K (Co) yielding $Ba_{1-x}K_xFe_2As_2$ ($Ba(Fe_{1-x}Co_x)_2As_2$) which preserves the $I4/mmm$ space group. (b) The Fe-As layers are separated by alternating layers of Ca (blue) and K atoms (yellow) giving rise to the $P4/mmm$ space group in which the upper As atoms As(1) are to be distinguished from the lower As(2) atoms.

In contrast, the mismatch of the atomic radii of Ca and K of the order $\sim 40\,\mathrm{pm}$ facilitates the formation of the $P4/mmm$ space group [29] in which the Fe-As layers are separated by alternating layers of Ca and K. Thus, the positions of the As atoms become distinguishable and the following notation is introduced: As(1) indicates the As atoms associated with the Ca layers and the As(2) the As atoms closer to K layer. Thus, the primitive unit cell of $CaKFe_4As_4$ is twice as large as that of $BaFe_2As_2$. This has a profound effect on the number of Raman-active phonons as described in Ref. [47] and appendix A.

As the electronic interactions contributing to superconductivity in the FeSC lie in the focus of this thesis, we turn to the Fe-As layers which carry the electronic properties [48].

The pseudo-3D representation of these Fe-As layers is drawn in Fig. 2.2 (a) with the As atoms in green (out-of-plane) and the Fe atoms in red (in-plane). At this point, it is useful to define two unit cells: the crystallographic 2-Fe unit cell (red) and the electronic 1-Fe unit cell (dark blue). The electronic properties are dominated by the Fe $3d$ orbitals [26] depicted in panel (c). Therefore, the 1-Fe unit cell captures the essential electronic properties [49] discussed throughout this thesis. For completeness: the magnetic SDW phase present in the $BaFe_2As_2$ compounds, but not in $CaKFe_4As_4$, where hopping via the As atoms occurs [26] requires the use of the 2-Fe unit cell. Here, the As superstructure introduces an additional translational symmetry with the vector $(\pi, \pi)$. As the SDW phase was not subject of scrutiny in this thesis, the results are given with respect to the 1-Fe unit cell, if not indicated otherwise.

The first Brillouin zone (BZ) of this 1-Fe unit cell is presented in Fig. 2.2 (b). For both, $BaFe_2As_2$ and $CaKFe_4As_4$, three hole pockets $h^+$ are located at the $\Gamma$ point [30, 50–52] represented as idealised circular Fermi surfaces in blue.

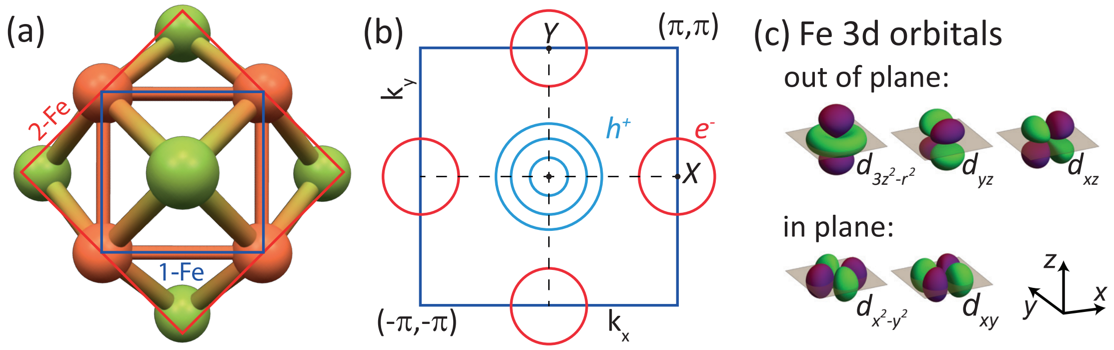

Figure 2.2: (a) Quasi-2D unit cell from the Fe-As layers with the crystallographic 2-Fe unit cell (black) and the electronic 1-Fe unit cell (dark blue). (b) Brillouin zone of the 1-Fe unit cell with schematics of the idealised hole (blue) and electron (red) pockets at the $\Gamma$, $X$ and $Y$ points. (c) $3d$ orbitals contributing to the electronic structure of $BaFe_2As_2$ and $CaKFe_4As_4$ from Ref. [23].

At the $X$ and $Y$ points, in turn, one finds two electron pockets $e^-$ [30, 50–52], where the shape of these pockets differ from each other in $BaFe_2As_2$ and

$CaKFe_4As_4$. In the $BaFe_2As_2$ compounds, they are more elliptic, while being rather isotropic in $CaKFe_4As_4$. For hole and electron pockets, the experimental evidence [30, 50–52] is well in agreement with theoretical band structure calculations [53, 54]. Additionally, the effect of atomic substitution in the $BaFe_2As_2$ compounds showed a drastic effect on the topology of the Fermi surfaces. In the hole-doped $Ba_{1-x}K_xFe_2As_2$ the K substitution expands the pockets at the $\Gamma$ point and shrinks the electron pockets [50, 55]. In contrast, electron doping in $Ba(Fe_{1-x}Co_x)_2As_2$ yields the opposite effect [56, 57]. This drastic change of the Fermi surface topology due to doping is accompanied by a variety of phases described in the next section.

## 2.2 Phase diagram

The phase diagrams of $Ba_{1-x}K_xFe_2As_2$ and $Ba(Fe_{1-x}Co_x)_2As_2$ are depicted in Fig. 2.3, where the phase separation lines are drawn as a function of the normalised doping $x/x_c$. At the critical doping $x_c$ the superconducting transition temperature $T_c$ is maximal and reaches 38 K for $Ba_{1-x}K_xFe_2As_2$. $CaKFe_4As_4$ is similar to optimally or overdoped $Ba_{1-x}K_xFe_2As_2$, when it comes to the transport and thermodynamic properties [58]. These similarities include the electronic structure. In particular the Fermi surfaces and the superconducting energy gaps can be treated in a similar fashion [30]. Upon doping $CaKFe_4As_4$, $T_c$ decreases [33] suggesting $CaKFe_4As_4$ to be intrinsically optimally doped. Concomitantly, $CaKFe_4As_4$ exhibits no other phase transition apart from superconductivity.

For electron-doped $Ba(Fe_{1-x}Co_x)_2As_2$, the superconducting dome has its maximum at $T_c = 24.6\,K$ for $x_c \approx 0.060$. This critical concentration coincides with the end point of the phase separation line of the nematic phase at $T = 0$. In contrast to $Ba_{1-x}K_xFe_2As_2$ [59], the nematic and SDW phase have two separate transition lines for $x > 0$ and the nematic transition is of second order [60, 61].

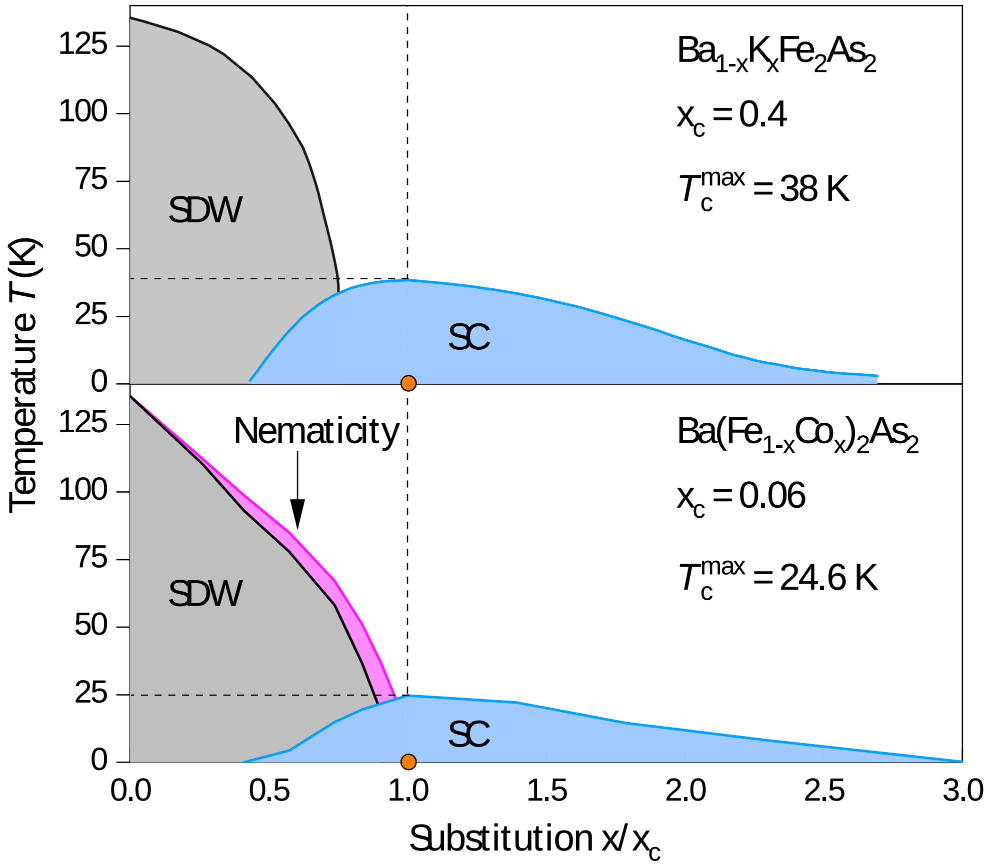

Figure 2.3: Phase diagrams of hole doped $Ba_{1-x}K_xFe_2As_2$ and electron doped $Ba(Fe_{1-x}Co_x)_2As_2$ as a function of the normalised doping $x/x_c$. The maximum transition temperature $T_c^{max}$ is 38 K and 24.6 K for $Ba_{1-x}K_xFe_2As_2$ and $Ba(Fe_{1-x}Co_x)_2As_2$, respectively. The orange circles indicate the position of the QCP beneath the superconducting dome [62]. The grey area indicates the spin-density-wave and the magenta stripe is the nematic phase. These transitions coincide in $Ba_{1-x}K_xFe_2As_2$. Data adopted from Ref. [19] and Ref. [22].

Fluctuations can be observed over a wide doping range, preceding the magneto-structural transition in $Ba_{1-x}K_xFe_2As_2$ and the nematic phase in $Ba(Fe_{1-x}Co_x)_2As_2$. These fluctuations are most likely magnetic in origin for underdoped $Ba(Fe_{1-x}Co_x)_2As_2$ [44] and may give relevant information about the superconducting ground state [63].

### 2.2.1 Spin-density-wave and nematicity

The interplay of the nematic and magnetic order in iron-based superconductors are well described by Fernades *et al.* in Ref. [63]. On the basis of this article, these transitions shall be outlined here. The SDW phase is a stripe-like magnetic order breaking the spin-rotational $O(3)$ symmetry. This is illustrated in Fig. 2.4 (a). The corresponding ordering vectors are either $\mathbf{Q}_\mathrm{X} = (\pi, 0)$ or $\mathbf{Q}_\mathrm{Y} = (0, \pi)$ in momentum space. The SDW phase is characterised by the spins being oriented parallel along one direction and anti-parallel along the other. This breaks the $Z_2$ symmetry as below $T_\mathrm{SDW}$ the system decides between one of the two directions. One can express the breaking of these symmetries in terms of the order parameters in momentum space

$$\mathbf{M}_\mathrm{X} = \sum_{\mathbf{k}} c^\dagger_{\mathbf{k}+\mathbf{Q}_\mathrm{X},\alpha} \sigma_{\alpha,\beta} c_{\mathbf{k},\beta} \tag{2.1a}$$

$$\mathbf{M}_\mathrm{Y} = \sum_{\mathbf{k}} c^\dagger_{\mathbf{k}+\mathbf{Q}_\mathrm{Y},\alpha} \sigma_{\alpha,\beta} c_{\mathbf{k},\beta} \tag{2.1b}$$

associated with the directions $\mathbf{Q}_\mathrm{X}$ and $\mathbf{Q}_\mathrm{Y}$, where $c^\dagger_{\mathbf{k}+\mathbf{Q}_\mathrm{X},\alpha}$ is the fermionic creation operator for a particle having momentum $\mathbf{k}+\mathbf{Q}_\mathrm{X}$ and spin $\alpha$, and $\sigma_{\alpha,\beta}$ are the Pauli spin operators. Below $T_\mathrm{SDW}$, the magnetisation $\langle \mathbf{M}_\mathrm{X} \rangle$ is different from zero along the ferromagnetically ordered axis and zero along the anti-ferromagnetically ordered axis $\langle \mathbf{M}_Y \rangle$ or vice versa. The breaking of the $Z_2$ symmetry corresponds to unequal magnetisations: $\langle \mathrm{M}_\mathrm{X}^2 \rangle \neq \langle \mathrm{M}_\mathrm{Y}^2 \rangle$. It is convenient to describe this in terms of the order parameters of two sublattices with $\mathbf{M}_1 = \mathbf{M}_\mathrm{X} + \mathbf{M}_\mathrm{Y}$ and $\mathbf{M}_2 = \mathbf{M}_\mathrm{X} - \mathbf{M}_\mathrm{Y}$ as indicated in green and yellow in Fig. 2.4 (a). Thus, within the magnetic phase, these are $\langle \mathbf{M}_i \rangle \neq 0$ and $\langle \mathbf{M}_1 \cdot \mathbf{M}_2 \rangle = \pm 1$. Nematic order can be placed in this framework as a state in which the $Z_2$ symmetry is broken and therefore $\langle \mathbf{M}_1 \cdot \mathbf{M}_2 \rangle = \pm 1$ holds. Yet at the same time, the spin-rotational symmetry is preserved as $\langle \mathbf{M}_i \rangle = 0$.

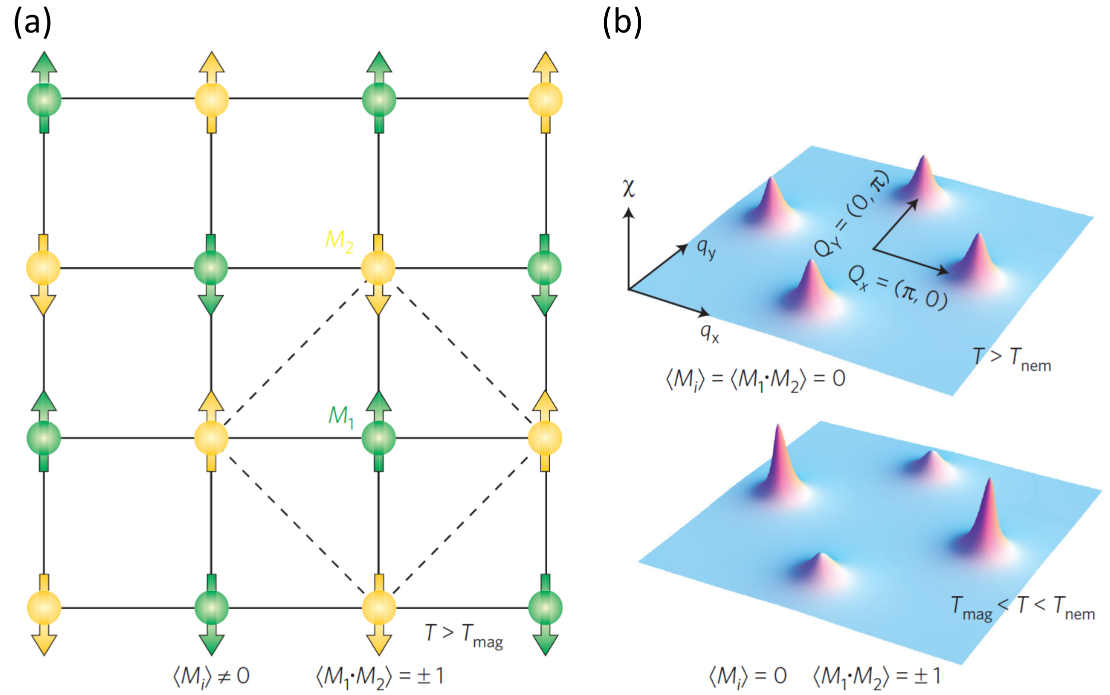

Figure 2.4: Real and momentum space nematic order representation. (a) The stripe-like order in real space consists of two interlocked Neél sublattices with magnetisations $\mathbf{M}_1$ and $\mathbf{M}_2$ which are given by the magnetic order parameters in momentum space $\mathbf{M}_X$ and $\mathbf{M}_Y$ with $\mathbf{M}_{1,2} = \mathbf{M}_X \pm \mathbf{M}_Y$. (b) Magnetic susceptibility $\chi(\mathbf{q})$ in the BZ. Above $T_s$ $\langle M_X^2 - M_Y^2 \rangle \equiv \langle \mathbf{M}_1 \cdot \mathbf{M}_2 \rangle = 0$. For $T_{SDW} < T < T_s$ $\langle M_X^2 - M_Y^2 \rangle \equiv \langle \mathbf{M}_1 \cdot \mathbf{M}_2 \rangle \neq 0$. From [63].

Fig. 2.4 (b) illustrates nematic order by means of the magnetic susceptibility $\chi(\mathbf{q})$ which is plotted within the first BZ. Above the nematic transition, the susceptibility is equal $\chi(\mathbf{Q}_X) = \chi(\mathbf{Q}_Y)$ at the ordering vectors and $\langle \mathbf{M}_i \rangle = \langle \mathbf{M}_1 \cdot \mathbf{M}_2 \rangle = 0$. This means, that both directions are equivalent, and no long-range order is established. Below the nematic transition temperature $T_{nem}$, $\chi(\mathbf{Q}_X)$ is not equivalent to $\chi(\mathbf{Q}_Y)$ and $\langle \mathbf{M}_1 \cdot \mathbf{M}_2 \rangle = \pm 1$ but $\langle \mathbf{M}_i \rangle = 0$. Within this spin-driven scenario, it is the spin-nematicity which gives rise to the orthorhombic distortion of the lattice corresponding to the structural transition at $T_s$.

Nematicity in FeSC could be explained in terms of orbital [64–66] or charge [67, 68] degrees of freedom rather than spin degrees of freedom as well. A previous study [44] favours a spin-driven scenario at least for $Ba(Fe_{1-x}Co_x)_2As_2$.

### 2.2.2 Superconductivity

Superconductivity, in turn, might be influenced by the same kind of interaction which affect the magneto-nematic transition and interrelated with nematicity as illustrated in Fig. 2.5.

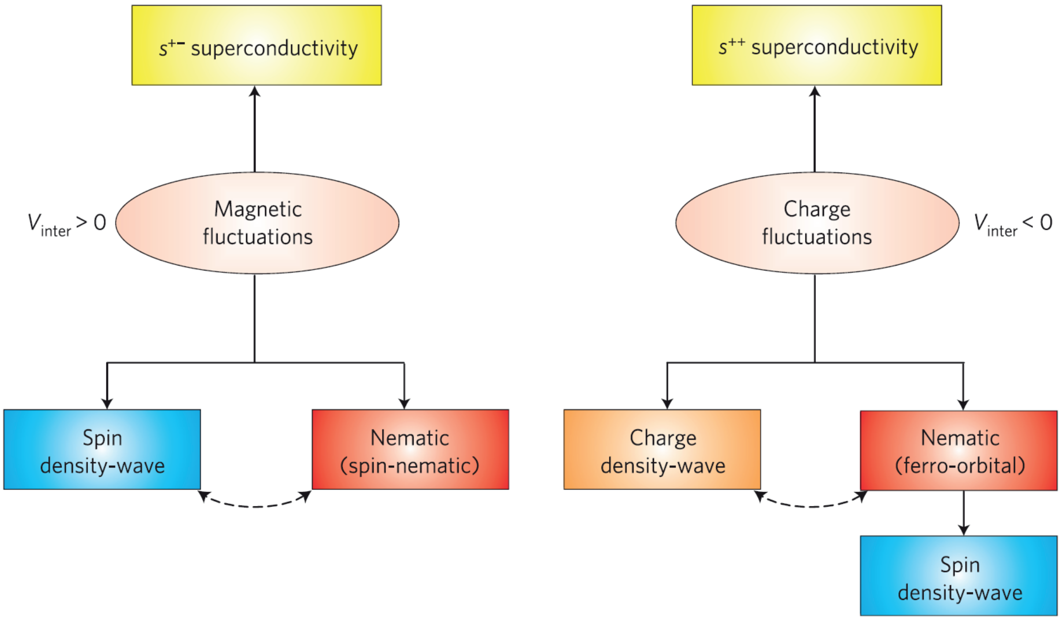

Figure 2.5: Magnetic versus charge fluctuations dominating the phase transitions in the pnictides. On the left hand side, the SDW phase as well as the spin-nematic state come about due to spin-fluctuations. The corresponding superconducting ground state has $s^{\pm}$ symmetry. On the right hand side, charge fluctuations lead to a charge-density-wave and a ferro-orbital nematic phase. This ferro-orbital ordering leads to the SDW. The superconducting ground state corresponding to charge fluctuations has $s^{++}$ symmetry. From Ref. [63].

On the left side, the dominant interaction in form of spin fluctuations may lead to both, the SDW as well as the spin-nematic state connecting the Fermi sheets at the $\Gamma$ and $X, Y$ points with the ordering vector $\mathbf{Q}_{X,Y}$. Then a superconducting state having $s^{\pm}$ symmetry forms due to the same repulsive interband interaction. On the other hand, the orbital or charge fluctuations with an attractive interaction could yield a charge-density-wave (CDW) and a ferro-orbital state. The nematic order yields the SDW phase. Consequently, the superconducting ground state arising from this interaction would have $s^{++}$ symmetry.

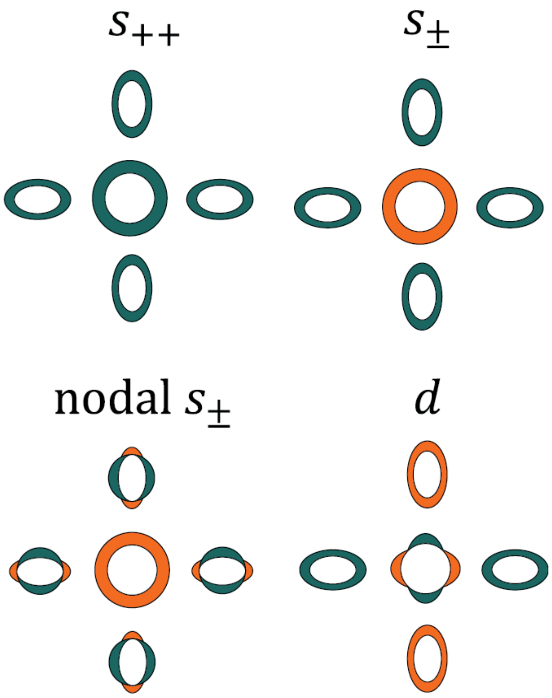

Figure 2.6: Superconducting order parameter for different pairing symmetries on Fermi surfaces in a quasi-2D BZ. The colours indicate the different signs of the order parameter. From [26].

Generally, the symmetry of the order parameter in the pnictides is not universally agreed on. This makes the situation here distinct from the situation in the cuprates where the $d$-wave nature of the order parameter is well established [69, 70]. In the case of the $BaFe_2As_2$ systems, the candidates describing the dominant interaction generally boil down to $s$-wave symmetry, i.e. transforming like $A_{1g}$ [26, 71]. This can either mean an $s^{\pm}$ or an $s^{++}$ ground state, depending on the sign of the interaction mediating the Cooper pairing. In Fig. 2.6 different order parameters are displayed within the first BZ. The $s^{++}$ ground state is characterised by the same sign on the different FS sheets which is in contrast to the sign-changing character of the $s^{\pm}$ ground state. For nodal $s^{\pm}$ symmetry, the order parameter changes sign within individual bands. The $d$-wave symmetry, although not dominating the interaction in the $BaFe_2As_2$ compounds, may be present as a subleading interaction in at least some of the pnictides such as $Ba_{1-x}K_xFe_2As_2$ and $CaKFe_4As_4$ which will be discussed in chapter 5.

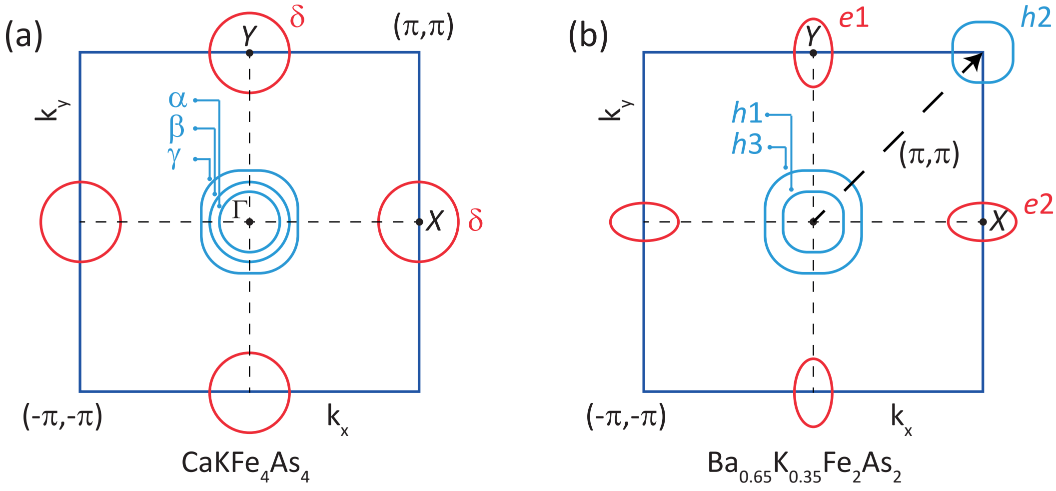

Figure 2.7: BZ of the 1-Fe unit cell with sketches of the band structure as derived from ARPES experiments for $CaKFe_4As_4$ and $Ba_{0.65}K_{0.35}Fe_2As_2$. (a) Three hole bands ($\alpha, \beta, \gamma$) at the $\Gamma$ point were resolved for $CaKFe_4As_4$ by Mou *et al.* [30]. One single electron band ($\delta$) was found at the $X$ point. (b) For $Ba_{0.65}K_{0.35}Fe_2As_2$, two hole bands ($h1, h3$) were resolved at the $\Gamma$ point. Two electron bands $e1$ and $e2$ were found at the $X$ and $Y$ point, respectively. From Nakayama *et al.* [72].

To prelude these results, a qualitative comparison of the band structure in $CaKFe_4As_4$ and $Ba_{0.65}K_{0.35}Fe_2As_2$ is given in Fig. 2.7 as derived from angle-resolved photo emission spectroscopy (ARPES). Greek letters correspond to the bands in $CaKFe_4As_4$. In $Ba_{0.65}K_{0.35}Fe_2As_2$, the hole and electron bands are indexed as ($h1, h2, h3$) and ($e1, e2$), respectively. The band $h2$ was not resolved by Nakayama *et al.* [72], and is most likely similar in size as $h1$ [23]. The comparison between the gap energies of $CaKFe_4As_4$ and $Ba_{0.65}K_{0.35}Fe_2As_2$ found by ARPES are summarised in Tab. 2.1. The ARPES gap energies are similar in magnitude. This is true particularly for the $\beta$ band of $CaKFe_4As_4$ and the $h1$ band of $Ba_{0.65}K_{0.35}Fe_2As_2$ and the electron bands.

Thus, the similarities between $CaKFe_4As_4$ and $Ba_{0.65}K_{0.35}Fe_2As_2$ inferred earlier extend to their electronic band and gap structure. Chapter 5 explores the spectroscopic similarities found in the inelastic light scattering data.

Table 2.1: Comparison of twice the gap energies from ARPES data on CaKFe$_4$As$_4$ [30] and Ba$_{0.65}$K$_{0.35}$Fe$_2$As$_2$ [72].

| CaKFe$_4$As$_4$ | | Ba$_{0.65}$K$_{0.35}$Fe$_2$As$_2$ | |
|---|---|---|---|
| band index $i$ | $2\Delta_i^{\text{ARPES}}$ (meV) | band index $i$ | $2\Delta_i^{\text{ARPES}}$ (meV) |
| $\alpha$ | 21 | h1 | 24.6 |
| $\beta$ | 24 | | |
| $\gamma$ | 16 | h3 | 12 |
| $\delta$ | 24 | e1 | 24.4 |
| | | e2 | 23 |

The second part of this thesis is the investigation of fluctuations above the superconducting dome in the electron doped Ba(Fe$_{1-x}$Co$_x$)$_2$As$_2$ which may originate from a quantum critical point (QCP) located at optimal doping [73,74].

QCPs in metals have been discussed for many years [75–79] and are thought to enhance superconductivity. Recently, it has been suggested, that this enhancement might be present close to a nematic QCP as well [37] which may reside underneath the superconducting dome. This will be described in the next section.

### 2.2.3 Quantum phase transitions

A quantum critical point (QCP) [80] is a second order phase transition at $T = 0$. While the QCP itself is inaccessible by its very nature, the QCP leads to quantum fluctuations which can extend over a wide temperature range and may be probed by different methods [73,74,81–83].

QCPs might be relevant to the formation of superconducting domes [84]. Their fluctuations may play the role of exchange bosons mediating the Cooper pairing [78,85]. In fact, there are theoretical calculations [35,84] which suggest, that a QCP always leads to superconductivity. To illustrate this in a qualitative manner[2], consider Fig. 2.8.

---

[2] The description is based on a talk by A. Chubukov [86] where the general ideas behind Ref. [35] are outlined.

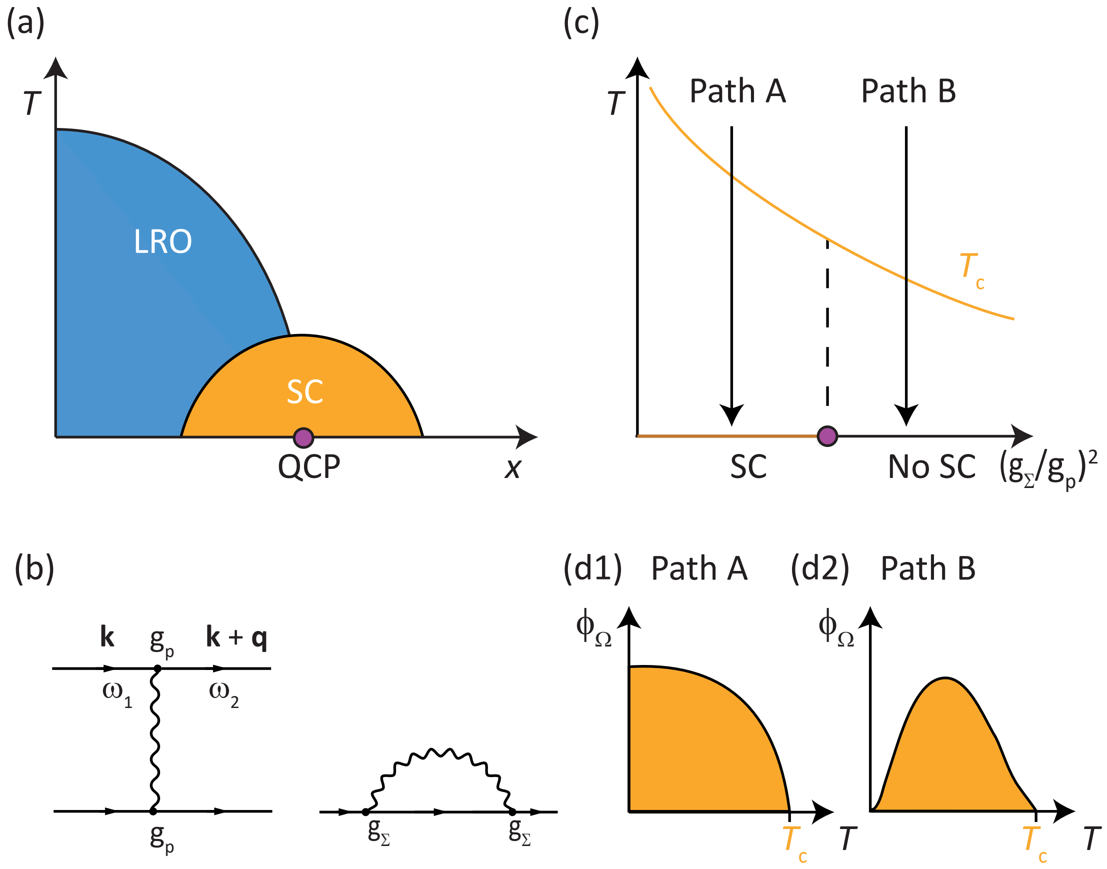

Figure 2.8: (a) Phase diagram. The blue area represents a long-range order (LRO). The orange area is the superconducting dome. The purple circle indicates the location of the QCP. (b) Feynman diagrams of the competing mechanisms: the pair bonding of fermions (arrows) via a bosonic mode (wavy line) with interaction constant $\mathrm{g_p}$ leading to superconductivity and fermionic self energy effects with interaction constant $g_\Sigma$. (c) The $T$-$(g_\Sigma/g_p)^2$ phase diagram. Below a critical threshold indicated by the purple circle the system develops superconductivity at $T = 0$. Above this threshold, superconductivity is present for $T > 0$ and vanishes at $T = 0$. The qualitative behaviour of the anomalous vertex $\phi_\Omega$ along the path A and path B is depicted in (d1) and (d2). Path A develops superconductivity down to $T = 0$. Path B develops superconductivity for $0 < T < T_c$ which vanishes at $T = 0$. Adapted from Ref. [86].

In panel (a) we find a $T$-$x$ phase diagram with a tuning parameter $x$ being, e.g. pressure or doping. Within the blue phase, the system exhibits a magnetic long-range order (LRO). Following the phase separation line of this second order phase transition down to zero temperature, one finds a quantum critical point (QCP) above which a superconducting dome may exist. The competing interactions at $T = 0$ are depicted in panel (b). The first diagram represents the pair bonding interaction of two fermions (straight lines) via a bosonic mode (wavy line) with interaction constant $g_p$. This pairing mechanism competes with self-energy effects depicted in the second diagram (Schwinger-Dyson, *cf.* [87, 88]) in which the interaction constant is $g_\Sigma$. The self-energy effects are destroying fermionic coherence, thereby preventing a superconducting ground state from forming. Using an Eliashberg-like approach for this problem, one can calculate the anomalous vertex $\phi$ which is not explicitly shown here. The reader is referred to Ref. [35] for details instead. The conclusion of this calculation is represented in Fig. 2.8 (c). Here, $(g_\Sigma/g_p)^2$ is drawn as a function of temperature $T$. At $T = 0$ one finds two distinct regimes: superconductivity below and Fermi liquid behaviour above a certain threshold marked by the purple circle. The calculations of the anomalous vertex $\phi$ however gives a finite $T_c$ for $T > 0$ regardless of the ratio $(g_\Sigma/g_p)^2$. This becomes clear by considering the two paths A and B through the phase diagram which yield a different temperature dependence of $\phi$ as depicted in panels (d1) and (d2). Along path A, $\phi_\Omega$ is finite for $T < T_c$ and especially at $T = 0$. Path B [panel (d2)] exhibits superconductivity only for the temperature window $0 < T < T_c$. At $T = 0$, the self-energy effects destroy the fermionic coherence and $\phi_\Omega = 0$. One is left with a non-

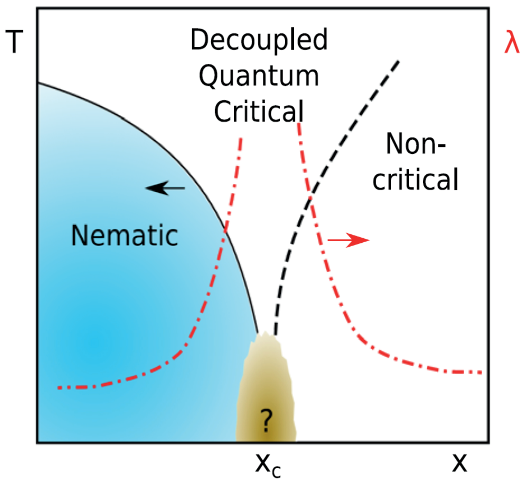

Figure 2.9: Nematic quantum critical point. The blue shaded area shows the nematic phase as a function of the tuning parameter x. A nematic QCP is found at $x_c$. The red dashed line shows the pairing eigenvalue $\lambda$. From [37]. The black-dashed line indicates the disordered regime.

superconducting ground state at $T = 0$. Thus: a QCP may induce superconductivity at temperature $T > 0$, even if the destruction of fermionic coherence at $T = 0$ yields a non-superconducting state.

Not only is a QCP considered to induce superconductivity at finite $T_\mathrm{c}$, it may also play a role by just enhancing $T_\mathrm{c}$. Lederer *et al.* [37] investigated the enhancement of superconductivity due to a nematic quantum critical point (NQCP). A sketch of the weak-coupling scenario is depicted in Fig. 2.9 where we follow the nematic phase down to zero transition temperature. Again, we find a quantum critical point, this time associated with the nematic long-range order. From this NQCP, a critical interaction $V^{(\mathrm{ind})}$ contributes to the effective interaction

$$V^{(\mathrm{eff})}_{k,k'} = V^{(0)}_{k,k'} + V^{(\mathrm{ind})}_{k,k'} \tag{2.2}$$

in which $V^{(0)}$ is the direct interaction between the electrons of a Cooper pair. $V^{(\mathrm{ind})}$ results from fluctuations of the NQCP which play the role of the interaction bosons. This interaction is attractive in all channels, therefore contributing to the pairing regardless of the exact form of $V^{(0)}$. With this, one finds the gap equation

$$\int \mathrm{d}\hat{k}'\, \tilde{V}^{(\mathrm{eff})}_{\hat{k},\hat{k}'} \phi^{(a)}_{\hat{k},\hat{k}'} = -\lambda_a \phi^{(a)}_{\hat{k}} \tag{2.3}$$

where $\phi^{(a)}_{\hat{k},\hat{k}'}$ is the pair wave function, and $\lambda_a$ are the eigenvalues. $\tilde{V}^{(\mathrm{eff})}_{\hat{k},\hat{k}'}$ is the effective renormalised interaction, now consisting of an renormalised interaction term

$$V^* = \frac{V^{(0)}}{1 + V^{(0)} \log(W/\Omega)} \tag{2.4}$$

which introduces a high energy cutoff $W$ and in which $\Omega$ results from Landau damping. From Eqn. 2.3, $T_\mathrm{c}$ is determined by the largest $\lambda_a \equiv \lambda$ via

$$T_\mathrm{c} \sim \exp\left[-1/\lambda\right]. \tag{2.5}$$

Treating the indirect interaction by means of first order perturbation theory, one can write $\lambda_a$ as

$$\lambda_a = \lambda_a^{(*)} + \delta\lambda_a^{(\mathrm{ind})} \tag{2.6}$$

with $\lambda_a^{(*)}$ being the eigenvalue of the renormalised direct interaction and $\delta\lambda_a^{(\mathrm{ind})}$ of the indirect direction being treated as perturbative term. $T_\mathrm{c}$ is then renormalised

$$T_\mathrm{c} \sim T_\mathrm{c}^{(0)} \exp\left[\delta\lambda^{(\mathrm{ind})}/(\lambda^{(0)})^2\right]. \tag{2.7}$$

with $\lambda^{(0)}$ being the eigenvalue of $V^{(0)}$. This means, that $T_\mathrm{c}$ can grow considerably for $\delta\lambda^{(\mathrm{ind})} >> (\lambda^{(0)})^2$ if one approaches the nematic quantum critical point [37].

Generally, the rules of the superconducting pairing in systems having a QCP are not entirely understood [89]. This motivates the experimental work on this phenomenon. As shall be seen in chapter 6, Raman spectroscopy proves to be a tool to investigate quantum critical fluctuations.

# Chapter 3

# Raman spectroscopy

The following chapter gives an overview of Raman spectroscopy [90–93] with an emphasis on inelastic light scattering from electrons, and how experimental quantities are derived from general arguments about the crystal symmetry. For an in-depth analysis, the reader is referred to Ref. [94].

## 3.1 Principles of Raman scattering

Raman scattering represents an inelastic photon-in photon-out process. To illustrate the underlying effect (see Fig. 3.1), we assume an isolated, non-interacting electron to be in a state $|i\rangle$ with corresponding energy $E_i$. At $t_1 = 0$, a photon with momentum $\mathbf{k}_i$, energy $\omega_i$ and polarisation $\mathbf{e}_i$ induces a first transition of the electron into a virtual state $|\nu\rangle$ with energy $E_\nu$. This transition leaves a hole in the state $|i\rangle$. As the virtual state is short lived by nature, the second transition occurs within a time $\Delta t < \hbar/\Delta E$. Upon emitting a photon with momentum $\mathbf{k}_s$, energy $\omega_s$ and polarisation $\mathbf{e}_s$, the electron relaxes from $|\nu\rangle$ into its final state $|f\rangle$ having energy $E_f$. Electron and hole form a quasiparticle, an exciton, with frequency $\Omega$ and momentum $\mathbf{q}$ which are given by the conservation laws for energy and momentum:

$$\Omega = \omega_i - \omega_s \tag{3.1}$$

$$\mathbf{q} = \mathbf{k}_i - \mathbf{k}_s \tag{3.2}$$

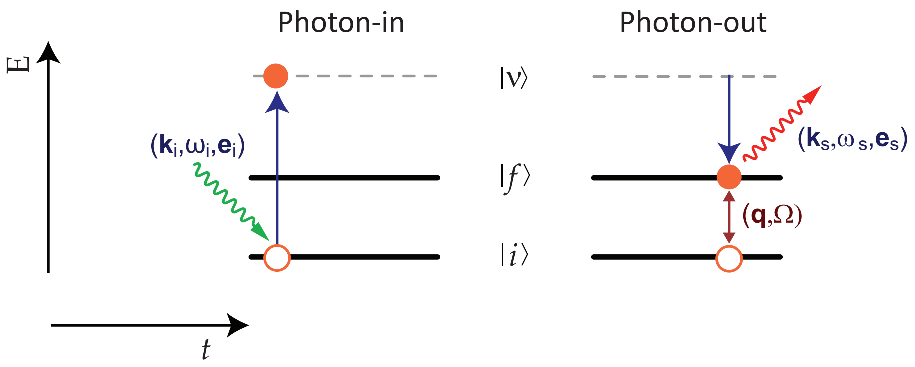

Figure 3.1: Sketch of the Raman effect with energy E vertically and time $t$ horizontally. The incident photon of momentum $\mathbf{k}_i$, energy $\omega_i$ and polarisation vector $\mathbf{e}_i$ excites an electron (orange) from the initial state $|i\rangle$ into a virtual state $|\nu\rangle$ leaving a hole (orange circle) in state $|i\rangle$. Upon relaxation into a final state $|f\rangle$ with $E_f \neq E_i$, a photon is emitted with momentum $\mathbf{k}_s$, energy $\omega_s$ and polarisation vector $\mathbf{e}_s$ creating an electron-hole pair (exciton) having momentum $\mathbf{q}$ and energy $\Omega$.

$\Omega$ represents the shift in frequency which is called the Raman shift. It is a quantity measured relative to the initial energy $\omega_i$ and thus may be negative for $\omega_s > \omega_i$. This is called anti-Stokes process in contrast to the Stokes process for $\omega_s < \omega_i$. The probability for the former is decreased by a factor $\exp[-\beta\Omega]$. The anti-Stokes process will not be used in this thesis.

## 3.2 Theory

The observation of real many-body states by Raman spectroscopy demands a more sophisticated mathematical approach. Experimentally, one measures the rate of the photons $\dot{N}(\Omega, T)$ scattered from the many-body electronic system into a solid angle $[\tilde{\Omega}, \tilde{\Omega} + \mathrm{d}\tilde{\Omega}]$ and a frequency window of $[\omega_s, \omega_s + \mathrm{d}\omega_s]$. A schematic of a Raman spectrum is shown in 3.2 in which $\dot{N}$ is measured as a function of the Raman shift. The yellow shaded area results from elastic scattering (Rayleigh). The red shaded area corresponds to particle-hole excitations (excitons) and the blue peaks indicate vibrational excitations (phonons) which sit on top of the particle-hole continuum. The anti-Stokes regime ($\omega_s > \omega_i$) is accessible but is

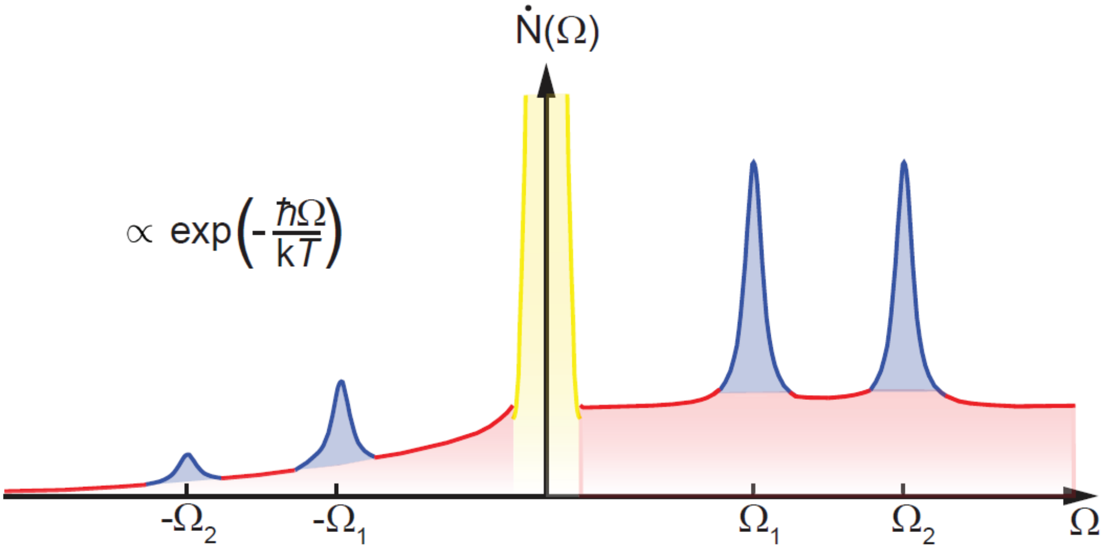

Figure 3.2: Schematic of a Raman spectrum. The yellow line shows the response from elastic scattering at $\Omega = 0$ due to Rayleigh scattering. Phonon modes (blue) at $\Omega_1$ and $\Omega_2$ may sit superimposed on top of a particle-hole continuum (red). If these phonons are already thermally activated, they can be destroyed, yielding the response at $-\Omega_1$ and $-\Omega_2$. As these processes are exponentially damped down, they are challenging to detect in an experiment. From Ref. [97].

used only for temperature determination or special applications such as coherent anti-Stokes Raman scattering (CARS) [95,96].

Now it will be outlined how the scattering rate $\dot{N}$ is related to the effective density-density correlation function. It is started with the fact, that $\dot{N}$ is proportional to the differential cross section

$$\dot{N}(\Omega, T) \propto \frac{\partial^2 \sigma}{\partial \tilde{\Omega} \partial \omega_s}. \tag{3.3}$$

The differential cross section is connected to the transition rate $\mathcal{R}$

$$\frac{\partial^2 \sigma}{\partial \tilde{\Omega} \partial \omega_s} = \hbar r_0^2 \frac{\omega_s}{\omega_i} \mathcal{R} \tag{3.4}$$

with the Planck constant $\hbar$ and the Thomson radius $r_0$. $\mathcal{R}$ is given by Fermi's golden rule

$$\mathcal{R} = \frac{1}{\mathcal{Z}} \sum_{I,F} \exp\left[-\beta E_I\right] | \langle F | M | I \rangle |^2 \delta(E_F - E_I - \hbar\Omega) \tag{3.5}$$

with the partition function $\mathcal{Z}$ and the inverse temperature $\beta = 1/k_B T$. The energies $E_I$ and $E_F$ correspond to the initial and final state $|I\rangle$ and $|F\rangle$, respectively. The $\delta$ function ensures energy conservation. The differential cross section is depending on the square of the Raman matrix element $M_{F,I} = \langle F | M | I \rangle$ in which $M$ is the transition operator. In an electronic many-body state, this transition operator is determined by the interaction terms which are part of the Hamiltonian [94,98,99]

$$\mathcal{H} = \mathcal{H}' + \underbrace{\frac{e}{2mc} \sum_i \{\hat{\mathbf{p}}_i, \hat{\mathbf{A}}(\mathbf{r}_i)\}}_{\text{current–photon interaction}} + \underbrace{\frac{e^2}{2mc^2} \sum_i \hat{\mathbf{A}}(\mathbf{r}_i) \cdot \hat{\mathbf{A}}(\mathbf{r}_i)}_{\text{charge–photon interaction}} \tag{3.6}$$

where $e$ is the electric charge, $m$ the electron mass, $c$ the speed of light, $\hat{\mathbf{p}}$ the momentum operator and $\hat{\mathbf{A}}$ the vector potential operator. $\mathcal{H}' = \mathcal{H}_0 + \mathcal{H}_{\text{fields}}$ is the Hamiltonian of the electronic many-body state with $\mathcal{H}_0 = 1/2m \sum_i \hat{\mathbf{p}}_i^2 + \mathcal{H}_{\text{Coulomb}}$ and the free electromagnetic part $\mathcal{H}_{\text{fields}}$. The two underbraces in Eqn. 3.6 indicate the current interaction and the charge interaction. The explicit form of the vector potential operator $\hat{\mathbf{A}}(\mathbf{r}_i)$ is

$$\hat{\mathbf{A}}(\mathbf{r}_i) = \sum_{\mathbf{q}} \sqrt{\frac{hc^2}{\omega_{\mathbf{q}} V}} \exp\left[i\mathbf{q} \cdot \mathbf{r}_i\right] \left[\hat{\mathbf{e}}_{\mathbf{q}} a_{-\mathbf{q}} + \hat{\mathbf{e}}^*_{\mathbf{q}} a^\dagger_{\mathbf{q}}\right] \tag{3.7}$$

with $\omega_{\mathbf{q}}$ being the photon frequency and $\hat{\mathbf{e}}_{\mathbf{q}}$ the polarisation direction. $a^\dagger_{\mathbf{q}}$ and $a_{\mathbf{q}}$ are the creation and annihilation operators of the photons, respectively. The polarisation dependence of the electromagnetic field operator appears in the derivation of the Raman cross section and is encapsulated in the Raman scattering amplitude $\gamma(\mathbf{k}, \mathbf{q})$ [100]. In the case of weakly interacting fermions, the current-photon and charge-photon interaction in Eqn. 3.6 can be treated by means of second and first order perturbation theory, respectively. Simplifying by using commutator algebra, one finds an expression for $M_{F,I}$ of the form

$$M_{F,I} = \sum_{\alpha,\beta} \gamma_{\alpha,\beta} \langle F| c^{\dagger}_{\alpha} c_{\beta} |I\rangle \tag{3.8}$$

in which $c^{\dagger}_{\alpha}$, $c_{\beta}$ are fermionic creation and annihilation operators. The factor $\gamma_{\alpha,\beta}$ is

$$\gamma_{\alpha,\beta} = \rho_{\alpha\beta}(\mathbf{q})\, \hat{\mathbf{e}}_i \cdot \hat{\mathbf{e}}_s + \frac{1}{m} \sum_{\beta'} \left( \frac{p^{s}_{\alpha,\beta'} p^{i}_{\beta',\beta}}{E_{\beta} - E_{\beta'} + \hbar\omega_i} + \frac{p^{i}_{\alpha,\beta'} p^{s}_{\beta',\beta}}{E_{\beta} - E_{\beta'} - \hbar\omega_s} \right). \tag{3.9}$$

The matrix element is thus connected to the matrix element of the single particle density fluctuation $\rho_{\alpha,\beta}(\mathbf{q}) = \langle\alpha| \exp[\mathrm{i}\mathbf{q}\cdot\mathbf{r}] |\beta\rangle$ and the momentum density matrix $p^{i,s}_{\alpha,\beta}(\mathbf{q}) = \langle\alpha| \mathbf{p}\mathbf{e}_{i,s} \exp[i\mathbf{q}_{i,s}\mathbf{r}] |\beta\rangle$. Indexing the states with momentum quantum numbers, the matrix element $M_{F,I}$ may be transformed into the effective density

$$\tilde{\rho}(\mathbf{q}) = \sum_{\mathbf{k},\sigma} \gamma(\mathbf{k},\mathbf{q}) c^{\dagger}_{\mathbf{k}+\mathbf{q},\sigma} c_{\mathbf{k},\sigma} \tag{3.10}$$

with momentum index $\mathbf{k}$ and spin $\sigma$. Here, $c^{\dagger}_{\mathbf{k}+\mathbf{q},\sigma}$ and $c_{\mathbf{k},\sigma}$ describe the scattering of a fermion from a state $(\mathbf{k},\sigma)$ into a state $(\mathbf{k}+\mathbf{q},\sigma)$ which is weighted by the Raman scattering amplitude $\gamma(\mathbf{k},\mathbf{q})$. Plugging the effective density into Eqn. 3.5 and expressing the $\delta$ function as a time integral, the scattering rate is rewritten as

$$\mathcal{R} = \sum_{I} \frac{\exp\left[-\beta E_I\right]}{\mathcal{Z}} \int \mathrm{d}t\ \exp\left[\mathrm{i}\Omega t\right] \langle I| \tilde{\rho}(\mathbf{q},t)\tilde{\rho}(-\mathbf{q},0) |I\rangle\,. \tag{3.11}$$

This expression can be connected to the correlation function given by the effective density which reads

$$\tilde{S}(\mathbf{q},\mathrm{i}\Omega) = \sum_{I} \frac{\exp[-\beta E_I]}{\mathcal{Z}} \int \mathrm{d}\tau \exp[\mathrm{i}\Omega\tau] \langle I| T_{\tau}\tilde{\rho}(\mathbf{q},\tau)\tilde{\rho}(-\mathbf{q},0) |I\rangle \tag{3.12}$$

where $\tau$ is the complex time. To get a real-frequency expression, one deploys the analytic continuation from the imaginary to the real axis which is $\mathrm{i}\Omega \rightarrow \Omega + \mathrm{i}0$. The cross section is then given in terms of the effective density-density correlation function:

$$\frac{\partial^2\sigma}{\partial\tilde{\Omega}\partial\omega_s} = \hbar r_0 \frac{\omega_s}{\omega_i}\tilde{S}(\mathbf{q}, \mathrm{i}\Omega \to \Omega + \mathrm{i}0) \tag{3.13}$$

Furthermore, the differential cross section can be connected to the effective charge density susceptibility

$$\tilde{\chi}(\mathbf{q}, \Omega) = \langle\langle[\tilde{\rho}(\mathbf{q}), \tilde{\rho}(-\mathbf{q})]\rangle\rangle_\Omega \tag{3.14}$$

via the fluctuation-dissipation theorem [101], as

$$\tilde{S}(\mathbf{q}, \Omega) = -\frac{1}{\pi}(1 + n(\Omega, T))\,\mathrm{Im}[\tilde{\chi}(\mathbf{q}, \Omega)] \tag{3.15}$$

with the Bose-Einstein distribution $n(\Omega, T)$. Therefore, the response function $\chi$ can be linked to the experimentally measured scattering rate $\dot{N}$, as aimed for in the beginning of this section. The next section shall explore how one can utilise the modulation of the charge fluctuations from light scattering by using group arguments.

## 3.3 Selection rules

In the limit $\mathbf{q} \to 0$, the matrix element $M_{F,I}$ can be written as [102–106]

$$M_{F,I}(\mathbf{q} \to 0) = \sum_\mu M_\mu \Phi_\mu \tag{3.16}$$

where $\mu$ is the irreducible representation of the point group and $\Phi_\mu$ the basis functions. For the $D_{4h}$ point group which is appropriate for the materials discussed in chapter 2, this reads:

$$\begin{aligned}M_{F,I} = &\frac{1}{2}\hat{O}_{\mathrm{A}_{1\mathrm{g}}^{(1)}}(e_i^x e_s^x + e_i^y e_s^y) + \frac{1}{2}\hat{O}_{\mathrm{A}_{1\mathrm{g}}^{(2)}}(e_i^z e_s^z)\\ &+ \frac{1}{2}\hat{O}_{\mathrm{B}_{1\mathrm{g}}}(e_i^x e_s^x - e_i^y e_s^y) + \frac{1}{2}\hat{O}_{\mathrm{B}_{2\mathrm{g}}}(e_i^x e_s^y - e_i^y e_s^x)\\ &+ \frac{1}{2}\hat{O}_{\mathrm{A}_{2\mathrm{g}}}(e_i^x e_s^y - e_i^y e_s^x) + \frac{1}{2}\hat{O}_{\mathrm{E}_{\mathrm{g}}^{(1)}}(e_i^x e_s^z + e_i^z e_s^x)\\ &+ \frac{1}{2}\hat{O}_{\mathrm{E}_{\mathrm{g}}^{(2)}}(e_i^y e_s^z + e_i^z e_s^y)\end{aligned} \tag{3.17}$$

with the projected operators $\hat{O}_\mu$ and the light polarisations $e^\alpha_{i,s}$. The choice of these light polarisations selects the corresponding operators. If the light polarisations are parallel to the $a$-$b$ planes, one projects out a mixture of symmetries. For instance, the polarisation configuration $e_i^x e_i^y$ collects $\mathrm{B}_{2\mathrm{g}}$ and $\mathrm{A}_{2\mathrm{g}}$ terms. Considering, that $\langle \hat{O}^\dagger_\mu \hat{O}_{\mu'}\rangle = R_\mu \delta_{\mu,\mu'}$, the mixed terms in Eqn. 3.5 vanish and therefore $\mathcal{R} \sim R_{\mathrm{B}_{2\mathrm{g}}} + R_{\mathrm{A}_{2\mathrm{g}}}$.

The matrix element is proportional to the Raman vertex $\gamma(\mathbf{k}, \mathbf{q} \to 0)$. Therefore the crystal harmonics by and large determine the Raman cross section.

Fig. 3.3 depicts the three polarisation configurations which were mainly utilised during this thesis. The upper row shows the 1-Fe unit cell with the iron atoms as red spheres. The arrows correspond to the polarisation vectors which project out sums of symmetries. The $\mathrm{A}_{2\mathrm{g}}$ response has been shown to be weak, flat and temperature independent for the pnictide systems [23,97,107].

The dominant contributions to the scattering amplitude stem from the $\mathrm{A}_{1\mathrm{g}}$, $\mathrm{B}_{1\mathrm{g}}$ and $\mathrm{B}_{2\mathrm{g}}$ symmetries, respectively. The second row shows the BZ of the 1-Fe unit cell with idealised hole and electron pockets as black circles (see chapter 2). The colours indicate the sign of the scattering amplitude $\gamma_\mu$. This illustrates the utility of Raman spectroscopy: controlling the polarisation of the incident and scattered photons, one can target different parts of the Brillouin zone. For the $\mathrm{A}_{1\mathrm{g}}$ symmetry, the second order $\mathrm{A}_{1\mathrm{g}}$ vertex $\gamma^{(2)}_{\mathrm{A}_{1\mathrm{g}}}$ captures the situation in the pnictides more accurately [28,108].

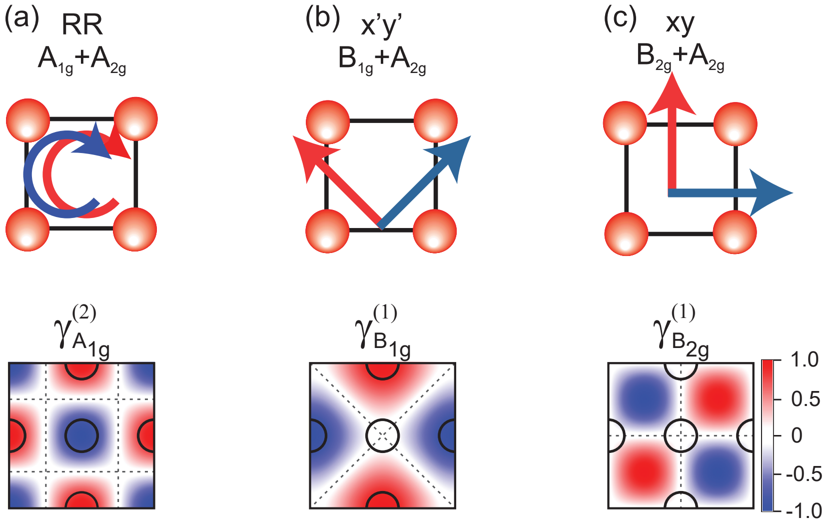

Figure 3.3: Polarisation configurations and Raman vertices in the 1-Fe unit cell and corresponding BZ, respectively. First row: the blue arrow indicates the incident polarisation, the red arrow the scattered polarisation state with respect to the Fe-Fe bonds (black lines connecting red Fe atoms). (a) $RR$ projects out symmetries $\mathrm{A}_{1g}$ + $\mathrm{A}_{2g}$, (b) $x'y'$ projects out $\mathrm{B}_{1g}$ + $\mathrm{A}_{2g}$ and (c) $xy$ correspondingly $\mathrm{B}_{2g}$ + $\mathrm{A}_{2g}$. The second row shows the momentum dependence of the Raman vertex $\gamma$.

## 3.4 Response for interacting particles

Raman spectroscopy provides access to interacting fermion systems. In particular, the superconducting response [106, 109, 110] and the response from fluctuations are outlined next.

### 3.4.1 Interband superconductivity

The superconducting interactions in the pnictides are dominated by interband interactions which can be probed by Raman scattering. Fig. 3.4 (a) shows a schematic representation of the first BZ as discussed in chapter 2. One idealised hole pocket at the $\Gamma$ point is connected via an $s$-wave interband interaction with electron pockets $\beta_1$ and $\beta_2$ at the $X$ and $Y$ points. The superconducting Raman response in lowest order can be described by the Feynman diagrams in panel (b) where $G$ is the single particle Green's function [23]

$$G(\mathbf{k}, \mathrm{i}\omega_n) = -\frac{\mathrm{i}\omega_n + E_{\mathbf{k}}}{(\mathrm{i}\omega_n)^2 + E_{\mathbf{k}} + \Delta_{\mathbf{k}}^2} \tag{3.18}$$

with the Matsubara frequencies $\omega_n$. $F$ is the Gorkov Green's function

$$F(\mathbf{k}, \mathrm{i}\omega_n) = \frac{\Delta_{\mathbf{k}}}{(\mathrm{i}\omega_n)^2 + E_{\mathbf{k}} + \Delta_{\mathbf{k}}^2}. \tag{3.19}$$

One can derive an expression for the Raman response from

$$\mathrm{Im}\left[\chi(\Omega)\right] = \mathrm{Im}\left[\sum_{n,\mathbf{k}} \gamma_n^2(\mathbf{k}) \cdot \lambda_n(\mathbf{k}, \Omega)\right] \tag{3.20}$$

with the Raman vertex $\gamma_n(\mathbf{k})$ and the Tsuneto function [100, 111, 112]

$$\lambda_n(\mathbf{k}, \mathrm{i}\Omega) = \frac{\Delta^2(\mathbf{k})}{E^2(\mathbf{k})} \cdot \tanh\left[\frac{E(\mathbf{k})}{2k_\mathrm{B}T}\right] \cdot \left[\frac{1}{2E(\mathbf{k}) + \mathrm{i}\Omega} + \frac{1}{2E(\mathbf{k}) - \mathrm{i}\Omega}\right] \tag{3.21}$$

Then, the Raman response from a single band $n$ in lowest order [100, 113] reads

$$\chi''(\Omega) = \frac{4\pi}{\Omega}\left\langle \frac{\gamma_n^2(\mathbf{k}) \cdot |\Delta_n(\mathbf{k})|^2}{\sqrt{\Omega^2 - |2\Delta_n(\mathbf{k})|^2}} \right\rangle \tag{3.22}$$

for frequencies $\Omega > 2\Delta_n$ and zero below which is depicted in Fig. 3.4 (b) for an isotropic gap $\Delta_n(\mathbf{k}) = \Delta_0$ at $T = 0$. For $T > 0$, instead of a divergence, a peak is present at approximately $2\Delta(T) < 2\Delta(T = 0)$.

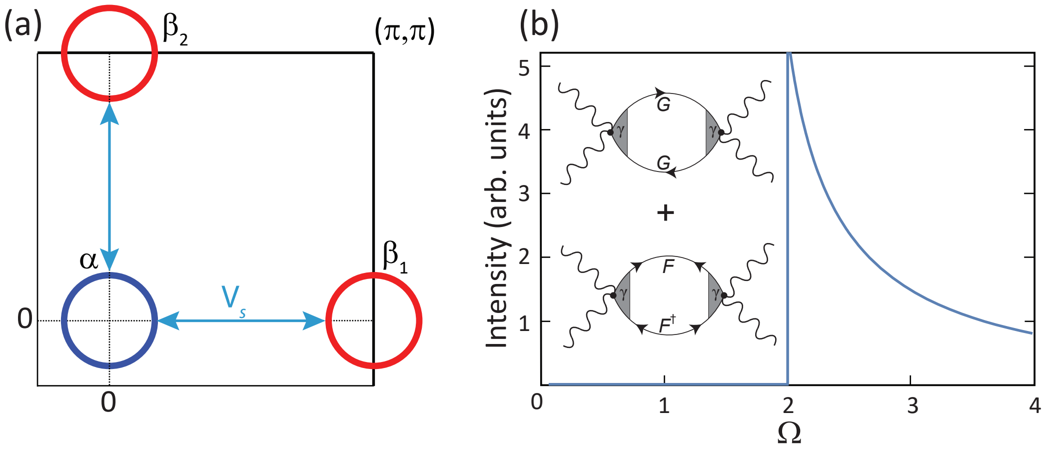

Figure 3.4: (a) An $s$-wave interband interaction $V_s$ is present between the hole pocket $\alpha$ at the $\Gamma$ point and the electron pockets $\beta_1$ and $\beta_2$ at the $X$ and $Y$ points. (b) The superconducting response at $T = 0$ is zero below $2\Delta$. The singularity at $2\Delta$ indicates the pair-breaking energy. The two Feynman diagrams build up the response. Adapted from [42].

This applies to $B_{1g}$ and $B_{2g}$ symmetries. In $A_{1g}$, the particle number conservation demands a renormalisation of the response via [23, 113]

$$\chi(\Omega) = \sum_{n,\mathbf{k}} \gamma_n^2(\mathbf{k}) \cdot \lambda_n(\mathbf{k},\Omega) - \frac{\sum_{n,\mathbf{k}} \gamma_n(\mathbf{k})\lambda_n(\mathbf{k},\Omega)}{\sum_{n,\mathbf{k}} \lambda_n(\mathbf{k},\Omega)}. \tag{3.23}$$

The processes contributing to the superconducting Raman process are depicted in Fig. 3.5 (a) and (b). In a fully gapped system, a fermion is either lifted above twice the band-gap $2\Delta$ or a Cooper pair is split.

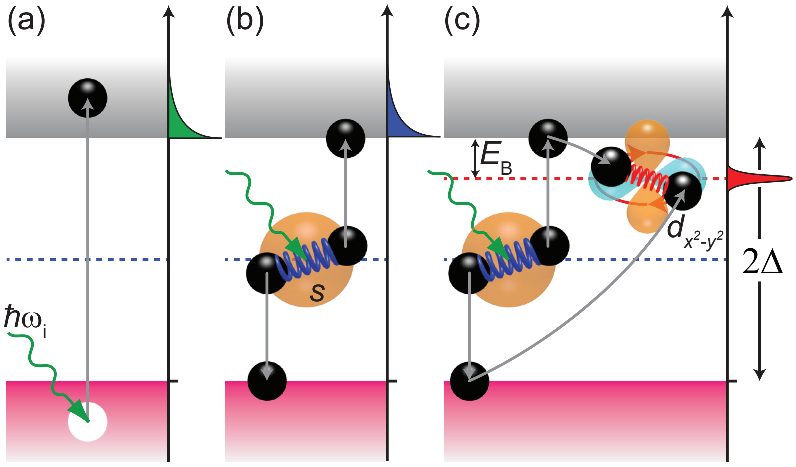

Figure 3.5: (a) A fermion is lifted above the energy gap of $2\Delta$. (b) A Cooper pair in the $s$-wave channel is broken up. (c) This Cooper pair recombines in the subdominant $d$-wave channel. From [23,27,28].

We now turn to the case, where a subdominant interaction is present. Fig. 3.5 (c) shows the underlying mechanism: additionally to the dominant $s$-wave channel, a $d$-wave channel is present. The Cooper pair is initially broken up, but recombines now in the $d$-wave channel. The additional diagram which builds up the response is presented in Fig. 3.6 with the subdominant interaction $V_d$ as the green dashed line.

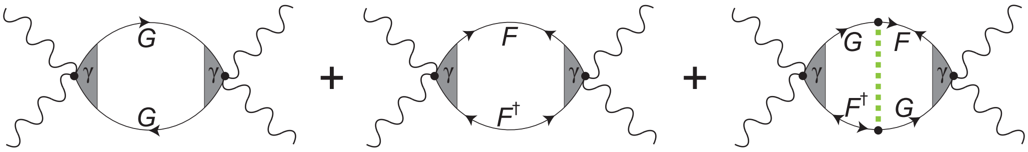

Figure 3.6: The first two Feynman diagrams are building up the response in the absence of a subdominant interaction. The last diagram gives an interacting term to the spectral function draining spectral weight from the pair breaking peak. From [23].

In the first BZ in Fig. 3.7, this subdominant interaction connects the electron pockets at the $X$ and $Y$ point. Fig. 3.7 (b) shows a sharp in-gap mode below $2\Delta$ in $B_{1g}$ symmetry. This mode occurs only in $B_{1g}$ symmetry. The argument for that follows the description in Ref. [42]: the response from the $\beta$ Fermi surfaces can be written as [42]

$$\frac{\Delta\chi(\Omega)}{N_\beta(0)} = -(N_\beta(0)\mathrm{V}_d)\cdot\left(\frac{\Delta_0}{\Omega}\right)^2\cdot\left\langle\gamma_\beta(\theta)g^d_\beta(\theta)g^s_\beta(\theta)\bar{P}(\Omega,\theta)\right\rangle^2 \tag{3.24}$$

where $N_\beta(0)$ is the density of states on the $\beta$ Fermi surface and $\mathrm{V}_d$ the subdominant interaction potential. The **k** dependency is parametrised with the angle $\theta$ and $\langle\cdot\rangle$ means the angular average. Additionally, one has

$$\bar{P}(\tilde\Omega_\theta) = \begin{cases} \frac{\tilde\Omega_\theta}{\sqrt{1-\tilde\Omega_\theta}}\arcsin\left[\tilde\Omega_\theta\right], & \left|\tilde\Omega_\theta\right| < 1 \\ \frac{\tilde\Omega_\theta}{\sqrt{\Omega_\theta^2-1}}\left[\ln\left(\left|\tilde\Omega_\theta\right| - \sqrt{\tilde\Omega_\theta - 1}\right) + \mathrm{i}\pi/2\right] & \left|\tilde\Omega_\theta\right| > 1 \end{cases} \tag{3.25}$$

with $\tilde\Omega_\theta = \Omega/2\Delta_\beta(\theta)$. The factor $\gamma_\beta(\theta)g^d_\beta(\theta)g^s_\beta(\theta)$ has to transform as $\mathrm{A}_{1g}$ in order to avoid cancellation. This is ensured, if $\gamma_\beta(\theta)$ and $g^d_\beta(\theta)g^s_\beta(\theta)$ transform as $\mathrm{B}_{1g}$. Therefore, the response is finite in the $\mathrm{B}_{1g}$ symmetry channel as the angular average does not vanish. Such an in-gap collective excitation is called a Bardasis-Schrieffer (BS) mode [27,42,104,114,115].

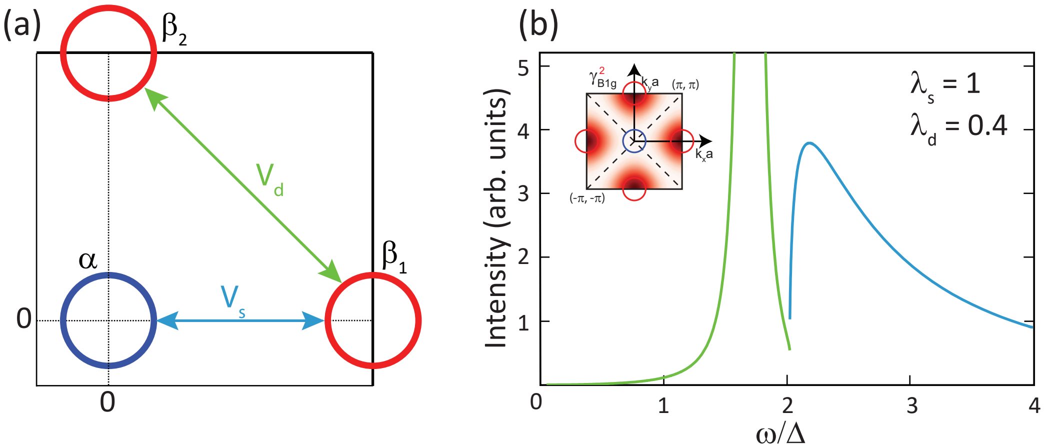

Figure 3.7: Phenomenological model for the Raman response of a BS excitonic mode. Additionally to the dominant $s$-wave interaction with interaction potential $\mathrm{V}_s$, a subdominant $d$-wave interaction connects the electron pockets at the $X$ and $Y$ point with interaction potential $\mathrm{V}_d$. (b) The Raman response in $\mathrm{B}_{1g}$ shows a sharp collective mode below $2\Delta$ which drains spectral weight from the pair breaking peak. From [42].

The total response in $B_{1g}$ is then given as

$$\chi''_{B_{1g}}(\Omega) = \frac{4\pi}{\Omega}\mathrm{Re}\left\langle \frac{\left|\Delta_\beta(\theta)\right|^2}{\sqrt{\Omega^2-(2\Delta_\beta(\theta))^2}}\right\rangle + a\,\mathrm{Im}\left[\frac{\left\langle \frac{|2\Delta_\beta(\theta)|}{\Omega}\bar{P}(\Omega,\theta)\right\rangle^2}{\lambda_d^{-1}-\lambda_s^{-1}-\langle\bar{P}(\Omega,\theta)\rangle}\right] \tag{3.26}$$

with the subdominant and dominant coupling constant $\lambda_d$ and $\lambda_s$, respectively. Raman spectroscopy thereby provides a tool to probe different pairing channels in systems with $D_{4h}$ symmetry and dominant $s$-wave interacting, regardless of $s^{++}$ or $s^{\pm}$ ground state. Nonetheless, the existence of such subdominant modes has been linked to Cooper pairing mediated by spin-fluctuations in $Ba_{1-x}K_xFe_2As_2$ [24], thereby pointing towards an $s^{\pm}$ scenario.

### 3.4.2 Fluctuations

Fluctuations can be probed by Raman scattering in a more direct way as well [44]. Charge, orbital or spin fluctuations can manifest themselves as a broad peak at low frequencies in some temperature interval $[T_f, T^*]$ above a phase transition at $T^*$ [43]. In the pnictide systems, these spectral signatures have been observed in underdoped $Ba(Fe_{1-x}Co_x)_2As_2$ as well as underdoped $Ba_{1-x}K_xFe_2As_2$ compounds [44, 62].

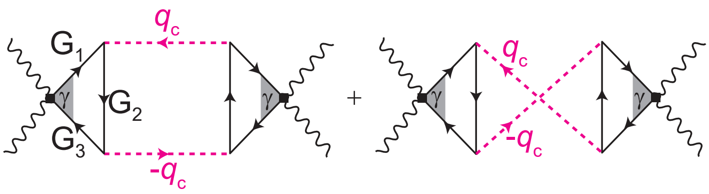

Figure 3.8: AL diagrams contributing to the Raman response. $G_i$ are fermionic propagators, $\gamma$ is the Raman vertex and the wavy lines are photonic propagators. The dashed lines are fluctuation propagators carrying momenta $\mathbf{q}_c$ and $-\mathbf{q}_c$. The triangles correspond to the electronic loop of Eqn. 3.28. From [23].

Generally, this broad signature from fluctuations is superimposed on the Raman response. The Feynman diagrams describing this response are called

Aslamazov-Larkin (AL) diagrams and were first discussed in the context of paraconductivity in superconductors [116].

The AL diagrams [43, 117–122] are depicted in Fig. 3.8. The dashed lines represent propagators carrying momenta $\mathbf{q}_c$ and $-\mathbf{q}_c$. This propagator reads [43]

$$D(\mathbf{q}, \omega_m) = \frac{1}{|\omega_m| + \nu\,|\mathbf{q} - \mathbf{q}_c|^2 + m(T)} \tag{3.27}$$

with a constant energy scale $\nu$, Matsubara frequencies $\omega_m$ and mass $m(T)$. The mass, in general, scales with the transition temperature $T^*$ at which the fluctuations vanish as a simple power law. These transition temperatures $T^*$ may correspond to the charge order in the cuprates [43] or the nematic transition in the pnictides [62]. The mass is related to the correlation length with $m(T) \propto \xi^{-2}$ [43]. The propagator becomes maximal for the critical wave vector $\mathbf{q} = \mathbf{q}_c$ of the fluctuations. The diagrams in Fig. 3.8 yield selection rules via their fermionic loops represented as solid triangles. The loop can be written as [43, 123]

$$\Lambda_{\alpha,\beta}(\Omega_l; \mathbf{q}, \omega_m) = CT \sum_n \sum_{\mathbf{k}} \gamma_{\alpha,\beta}(\mathbf{k}) G(\mathbf{k}, \epsilon_n, \Omega_l) G(\mathbf{k}-\mathbf{q}, \epsilon_n - \omega_m) G(\mathbf{k}, \epsilon_n) \tag{3.28}$$

in which $\gamma_{\alpha,\beta}(\mathbf{k})$ is the Raman vertex and $C$ is a constant. The sum over $\mathbf{k}$ space has contributions cancel out, if they originate from regions with opposite signs of the Raman vertex. To illustrate this further, the Raman vertex in first [(a1) to (c1)] and second order [(a2) to (c2)] derived solely from the crystal symmetry is depicted in Fig. 3.9 alongside the hole and electron pockets in the BZ of the 1-Fe unit cell.

The critical wave vector $\mathbf{q}_c = (\pi, 0)$ connects points on the hole pockets with points on the electron pockets indicated by the yellow ellipses. For these, the largest contribution to the fluctuation response is to be expected in the summation over all $\mathbf{k}$ vectors, but only if the sign of $\gamma_{\alpha,\beta}(\mathbf{k})$ does not change. Otherwise, the contributions cancel out. This is true for the first and second order $\mathrm{B_{1g}}$ vertex. Additionally, the first order $\mathrm{A_{1g}}$ vertex would, in principle, yield a contribution just from the point of crystal symmetry.

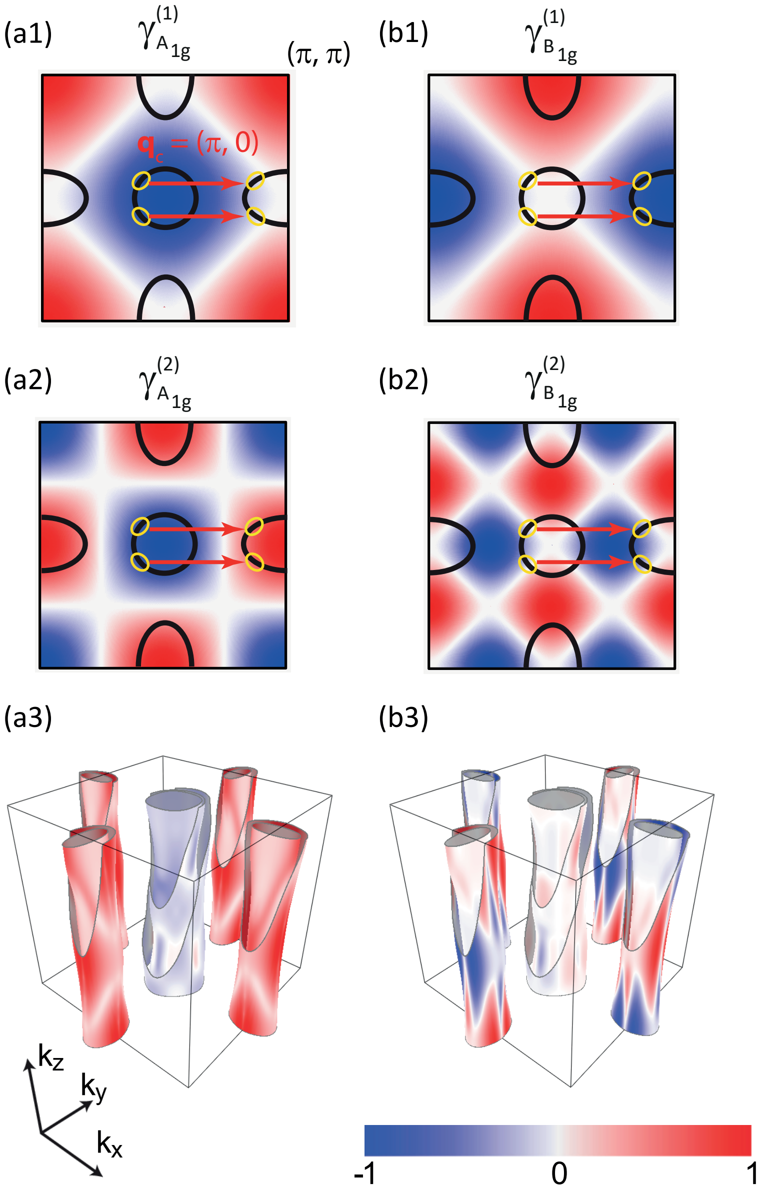

Figure 3.9: Selection rules for AL-fluctuations. (a1) to (c1) show the first order Raman vertices in the first BZ with the idealised hole pocket at the Γ point and two elliptical electron pockets at the $X$ and $Y$ point. (a2) to (c2) depict the second order vertices. The colour scheme indicates the sign of the vertex. The red arrows connect the Fermi surfaces by the critical vector $\mathbf{q}_c$. (a3) to (c3) show the projection of the Raman vertex onto the band structure using a five-band tight binding model. Adapted from [28] and [97].

However, Böhm *et al.* [28] showed, that the Raman vertex derived from the electronic band structure via an effective mass approximation changes sign between electron and hole pockets in $A_{1g}$ symmetry as can be seen in Fig. 3.9. Therefore, the only contribution to the Raman response is expected in $B_{1g}$ symmetry.

The spectral shape of this fluctuation contribution to the Raman response reads [43]

$$\chi''_{\mathrm{fluct}}(\Omega, T) = \Lambda^2_{\mathrm{B_{1g}}} \int_0^\infty \mathrm{d}z \, [b(z - \Omega/2) - b(z + \Omega/2)] \, \frac{z_+ z_-}{z_+^2 - z_-^2} \, [F(z_-) - F(z_+)] \tag{3.29}$$

with the Bose function $b(z)$ and

$$F(z) = \frac{1}{z} \arctan\left[\Omega_0/z\right] - \arctan\left[m/z\right] \tag{3.30}$$

and

$$z_\pm = (z \pm \Omega/2) \left[1 + (z \pm \Omega/2)^2/\Omega_0^2\right]. \tag{3.31}$$

$\Omega_0$ is a cutoff, $\Lambda_{\mathrm{B_{1g}}}$ is the vertex strength in $B_{1g}$ symmetry and $m(T)$ is the mass introduced with the fluctuation propagator in Eqn. 3.27.

The spectral shape of these fluctuations is drawn in Fig. 3.10 for three different temperatures $T_1 > T_2 > T_3 > T^*$. The increase of spectral weight goes along with the decrease of the mass $m(T)$ as shown in the inset. At the transition at $T^*$, the fluctuations vanish. In the case of thermal fluctuations, the mass obeys a power law of the form

$$m(T) = m_0 + a \cdot (T - T^*)^{2\nu} \tag{3.32}$$

where $T^* > 0$. For quantum fluctuations on the other hand, $T^*$ becomes zero (*cf.* Sec. 2.2.3) and the relationship simplifies to $m(T) \propto T^{2\nu}$.

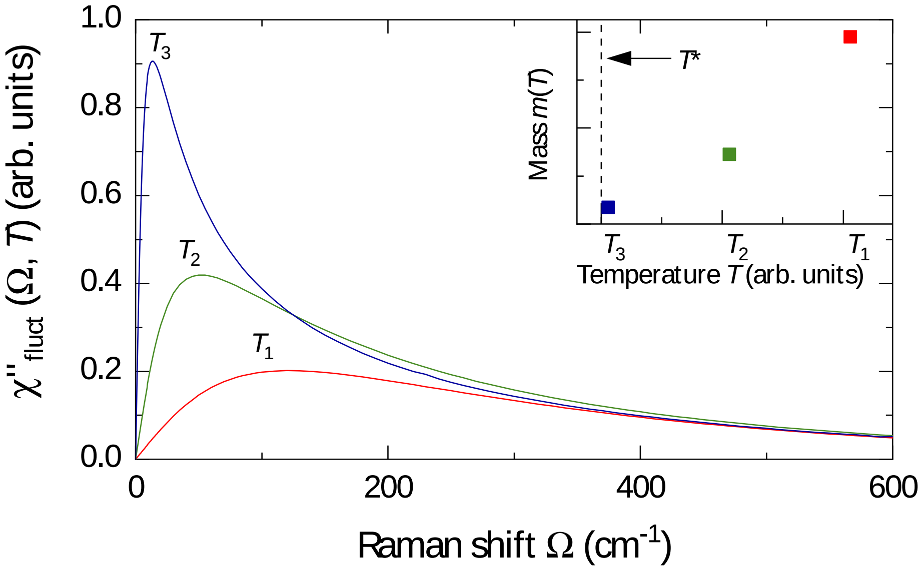

Figure 3.10: Spectral signature of AL-fluctuations for three different temperatures $T_1 > T_2 > T_3 > T^*$. The inset shows the corresponding mass $m(T)$ which decreases towards the transition.

# Chapter 4

# Experiment and samples

The following chapter outlines the optical setup and the preparation of the samples.

## 4.1 Scattering setup

The experimental setup used throughout this thesis is depicted in Fig. 4.1. The is positioned on the sample holder the position of which can be varied slightly along the $z$-axis of the laboratory frame. The surface of the sample is then moved into the confocal point of the scattering setup in Fig. 4.1. This setup is explained in the following:

The light source is a yellow solid state laser (Coherent, Genesis MX SLM) at $\lambda_{\mathrm{exc}}$ = 575 nm with a beam diameter of $\varnothing$ = 1 mm and a divergence of $\Delta_{\mathrm{div}}$ = 0.7 mrad. The beam diameter is optimised and the divergence minimised, before entering the polarisation selection and being focussed onto the sample. This is done via a variety of optical elements. It is convenient to define an optical axis along the path of the laser beam as emitted from the laser head, preferably parallel to the optical table. The centre of each optical element is positioned along this optical axis. The lenses L1 and L2 expand the beam. The mirror M1 directs it through the lens L3 of the first pinhole system (PH1). The beam is focussed onto a pinhole S1. The focal point of lens L4 coincides with the focal point of L3 and thus the position of the pinhole. Only the parallel parts of the beam are focussed onto this pinhole, while the divergent parts do not pass. Lens L4 parallelises the beam again. This process is repeated again at slit S2 ensuring a high beam quality.

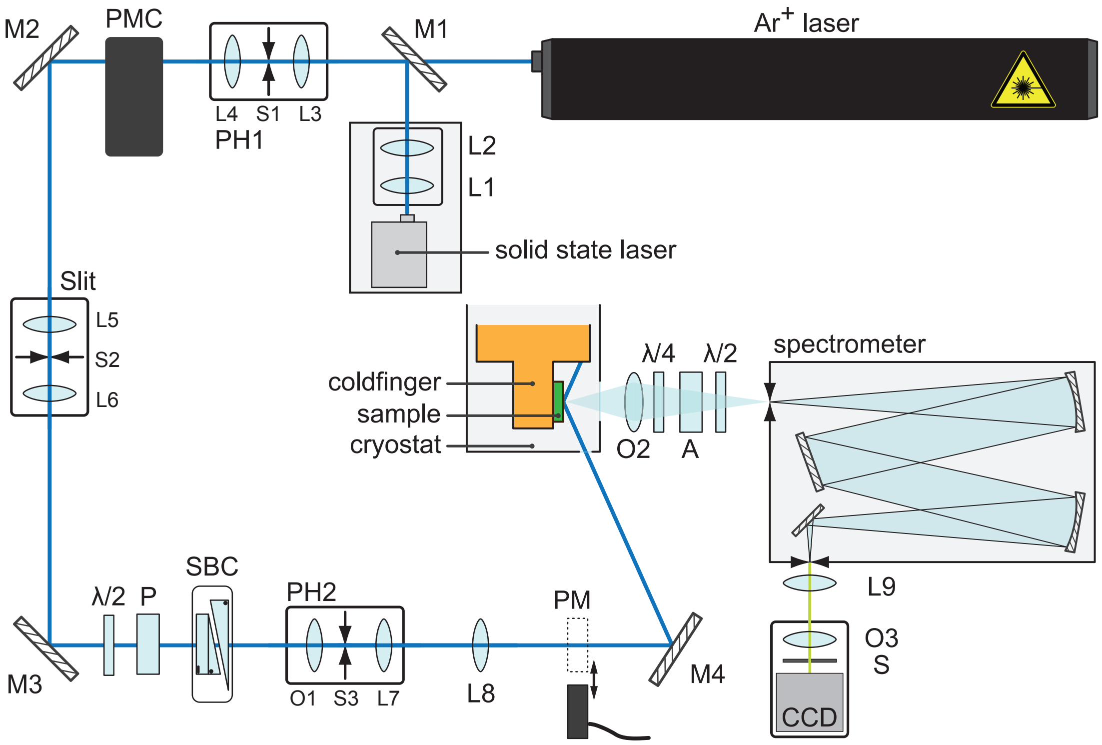

Figure 4.1: Experimental setup in the Raman Lab I. The light sources are an ion and a solid state laser. The letters refer to the following optical elements: lenses L$i$, mirrors M$i$, slits S$i$, pinhole systems PH$i$, the prism monochromator PMC and objectives O$i$. The incident intensity is set with a $\lambda/2$ waveplate and the power meter PM, and the incident polarisation with a polariser P and a Soleil-Babinet compensator SBC. The scattered light is selected with a $\lambda/4$ waveplate and an analyser A. For details, see text. From Ref. [124].

Two quantities are set before the beam is focussed onto the sample: the polarisation configuration and the intensity. The Glan-Thompson polariser P selects a linear polarisation. The Soleil-Babinet compensator (SBC) creates a well defined polarisation state. An SBC can, in principle, create elliptic polarisation states. With this combination of P and SBC, it is possible to set any desired polarisation of the incident light inside the sample, and in particular circularly and linearly polarised light. Then, the $\lambda/2$ is used to adjust the intensity measured at the power meter PM. Both, the SBC as well as the Glan-Thompson polariser, create interferences which are filtered with the second pinhole system (PH2). Lens L8 focusses the beam onto the sample. The objective O2 collects the scattered light. It passes the polarisation selection with the $\lambda/4$ waveplate and the analyser A before the $\lambda/2$ waveplate rotates the light into the preferential direction of the spectrometer. The spectrometer is a band-pass filter. The light exiting the spectrometer is parallelised at lens L9 and focussed onto a CCD chip with the objective O3. The shutter S is controlled by a measurement software developed at the WMI which determines the exposure time of the CCD.

## 4.2 Characterisation and preparation of the samples

The samples scrutinised in this thesis were superconducting single crystals of $CaKFe_4As_4$ and Co-doped $BaFe_2As_2$. The $CaKFe_4As_4$ sample was provided by the Canfield group at Ames Laboratory. The growth method is a high temperature solution growth out of FeAs flux [125], similar to the growth method of $Ba(Fe_{1-x}Co_x)_2As_2$ [19, 22, 126, 127]. The $Ba(Fe_{1-x}Co_x)_2As_2$ samples were provided by the Fisher group at Stanford University. The crystals grow such that the typical dimension of the single crystals are on the order $a \times b \times c = 5\text{mm} \times 5\text{mm} \times 1\text{mm}$ with the crystal axes $a$, $b$ and $c$ as defined in Fig. 2.1.

In the focus of this thesis stands the investigation of the superconducting phase. The knowledge of the transition temperature $T_c$ is therefore mandatory. To serve this purpose, the transition temperatures of the samples were characterised by measuring the $3^{rd}$ harmonic of the magnetic susceptibility $\chi_m$ as a function of temperature $T$. The experimental setup is described in detail in Ref. [107] and Ref. [128]. This method provides three advantages: for one, it is contactless. Two, it is more sensitive than, for instance, a regular susceptibility measurement, therefore enabling one to measure samples having a thickness in the mm range and smaller. Third, the method picks up on sample inhomogeneities.

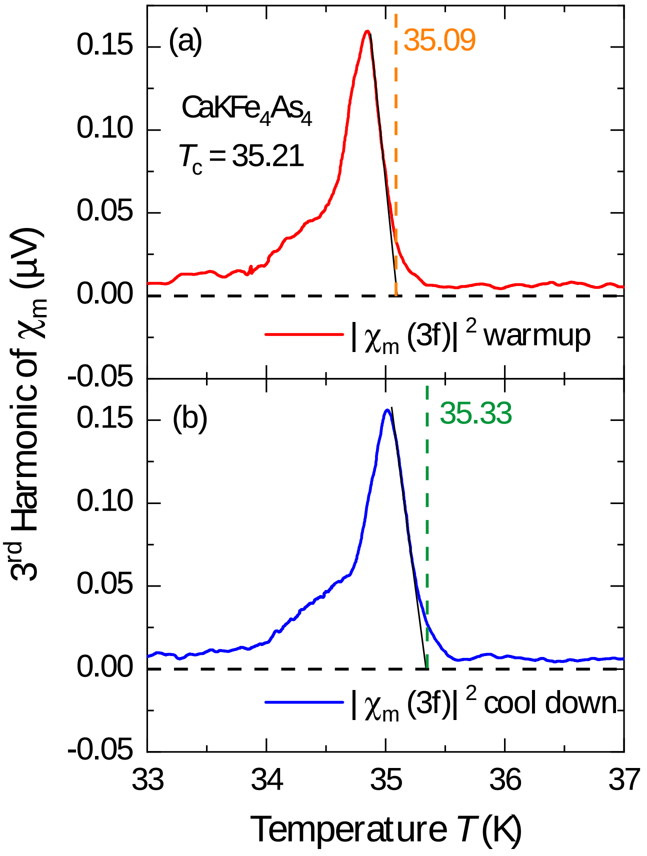

Figure 4.2: Third harmonic of the susceptibility of $CaKFe_4As_4$ measured upon heating (red) and cooling (blue).

The method utilises the occurrence of Abrikosov vortices [129] in a type-II superconductor when emerged into an external magnetic field $H_{\text{ext}}$ for which $H_{c1} < H_{\text{ext}} < H_{c2}$ (Shubnikov phase). For this phase, Bean predicted [130, 131] a constant critical current density $j_c$ flowing in some depth $\delta$ which shields the interior of the superconductor. When $H_{\text{ext}}$ is increased further, larger portions of the superconductor are penetrated by the vortices. Upon decreasing $H_{\text{ext}}$ again, an inductive current opposite to $j_c$ is created which traps a coercive magnetic field. This hysteretic behaviour leads to a sharp peak of the temperature dependence of $|\chi_{\text{m}}(3f)|^2$ for temperatures $T \lesssim T_{\text{c}}$.

This can be seen exemplarily for $CaKFe_4As_4$ in Fig. 4.2. The measurements were performed once upon heating (red) the sample and once upon cooling (blue) the sample through the superconducting transition. Both show a well-defined peak. Extrapolating the high temperature side to zero, this gives $T_c^{\text{heating}} = 35.09\,\text{K}$ upon heating and $T_c^{\text{cooling}} = 35.33\,\text{K}$ upon cooling. The average is then $T_c = 35.21\,\text{K}$. The width of the transition is therefore $\Delta T_c = 0.24\,\text{K}$.

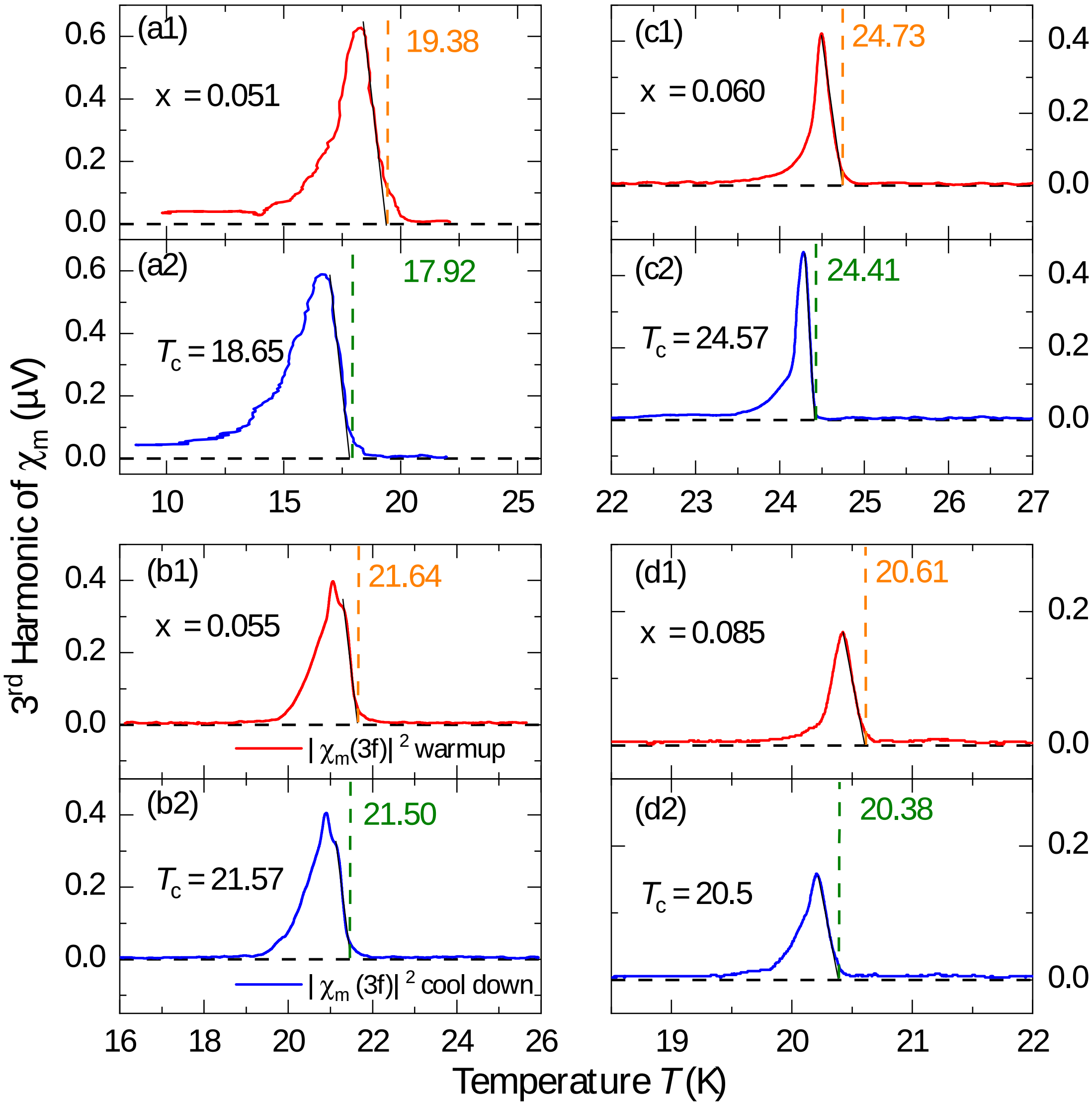

Figure 4.3: Third harmonic of the susceptibility of $Ba(Fe_{1-x}Co_x)_2As_2$ measured upon heating (red) and cooling (blue) with doping concentrations as indicated.

The small width as well as the shape of the signal indicate a homogeneous sample.

The same measurements were performed for the $Ba(Fe_{1-x}Co_x)_2As_2$ compounds. The results are presented in Fig. 4.3, where (a1) and (a2) show the results of earlier studies [23, 132]. The results of these measurements are summarised in Tab. 4.1.

Table 4.1: Summary with the superconducting transition temperature $T_c$, the magnetic transition $T_{SDW}$ and the nematic or structural transition $T_s$.

| Material | $T_c$ | $\Delta T_c$ | $T_{SDW}$ | $T_s$ |
|---|---|---|---|---|
| $CaKFe_4As_4$ | 35.21 | 0.24 | - | - |
| $Ba(Fe_{0.949}Co_{0.051})_2As_2$ | 18.65 | 1.46 | 50.0 | 60.9 |
| $Ba(Fe_{0.945}Co_{0.055})_2As_2$ | 21.57 | 0.14 | - | 50 |
| $Ba(Fe_{0.94}Co_{0.06})_2As_2$ | 24.57 | 0.32 | - | - |
| $Ba(Fe_{0.915}Co_{0.085})_2As_2$ | 20.5 | 0.23 | - | - |

After measuring $T_c$, the sample is glued onto a copper block using GE low temperature varnish. This is depicted in Fig. 4.4 (a), where the $c$-axis of the sample is parallel to the defined $c$-axis of the copper block $c_{Cu}$.

The copper block is inserted into the cylindrical sample holder in which it can be rotated around its $a_{Cu}$ axis. In order to fully utilise the Raman selection rules presented in Sec. 3.3, the orientation of the crystal's main axes relative to the sample holder has to be set ex-situ. The $c$-axis has to point perpendicular to the front of the sample holder. This is ensured by using a polarisation microscope, where the copper block is rotated until the reflection from the sample becomes maximal.

The $a$-$b$ plane is oriented using Laue diffraction with respect to the Laue coordinate system having axes $x$ and $y$[1]. These axes coincide with the laboratory system of the scattering setup discussed below. For the orientation in the Laue experiment, the sample holder is placed in an adjustment tool so that it can be rotated clock or counter-clockwise. Iteratively, the Laue diffraction pattern is

---

[1] Sometimes, cracks on the surface of the sample indicate the main axes of the crystal. This is visible under the polarisation microscope and can be used to set a starting point for the Laue diffraction experiment.

optimised so that the $a$-$b$ axes are well defined in the $x$-$y$ coordinate system.

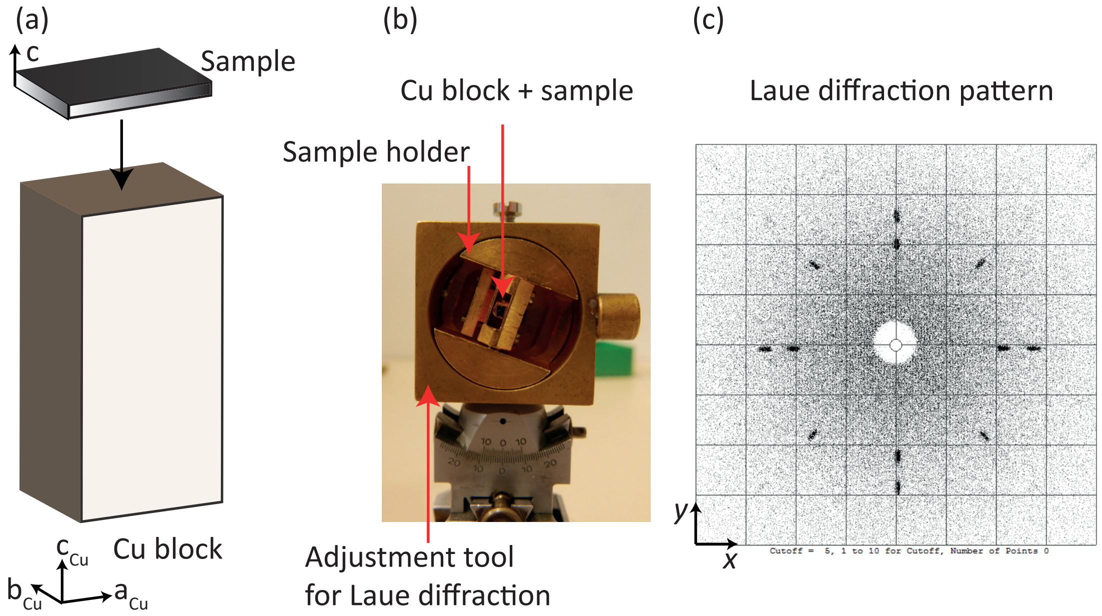

Figure 4.4: Orientation of the sample. (a) The sample is glued onto a copper block where the axes $a_{\mathrm{Cu}}$, $b_{\mathrm{Cu}}$ and $c_{\mathrm{Cu}}$ refer to the dimensions of the block as an aid for the explanation. (b) The copper block is inserted in an adjustment tool for the Laue diffraction. (c) The $a$-$b$ plane is oriented iteratively by rotating the sample holder so that the main reflexes are well defined in the $x$-$y$ coordinate system.

After preparing the orientation, the sample holder is mounted onto the coldfinger of the cryostat.

## 4.3 Checking the sample orientation and cleaving the surface

Before running the measurement schedule, the orientation of the sample is checked using Raman spectroscopy. For the 1144 as well as the 122 systems, this is can be done by probing the $B_{1g}$ phonon at 210 $\mathrm{cm}^{-1}$. If the crystal axes $a$ and $b$ are parallel to the laboratory frame with $x$ and $y$, the phonon will not appear for the light polarisation configuration $xy$. In turn, the strong phonon line will be visible for $x'y'$ polarisation.

If the surface of the sample shows poor quality, it can be cleaved using adhesive tape. Poor quality means here, that the laser spot on the surface of the sample is strongly visible. The pnictides usually exfoliate along (001).

# Chapter 5

# Subdominant $d$-wave interaction in $CaKFe_4As_4$

The dependence of the Raman response on the incoming and scattered light polarisations reveals the anisotropy of the energy gap and the existence of anisotropies of the pairing potential as discussed in Subsec. 3.4.1. This study is a litmus test for the universality of Cooper pairing in the $BaFe_2As_2$ compounds as anticipated from the band structure and earlier experiments in $Ba_{1-x}K_xFe_2As_2$ [24]. Part of the results were published in Ref. [45].

## 5.1 Overview: Raman spectra

Fig. 5.1 provides an overview over the Raman spectra of $CaKFe_4As_4$ above $T_c = 35.2\,K$ at $T = 43\,K$ (red), and below $T_c$ at $T = 11\,K$ (blue). All spectra were measured within the frequency window $\Omega \in [10, 310]$ cm$^{-1}$.

Three polarisation configurations were used as indicated by the pictograms, projecting the symmetries as described in Sec. 3.3.

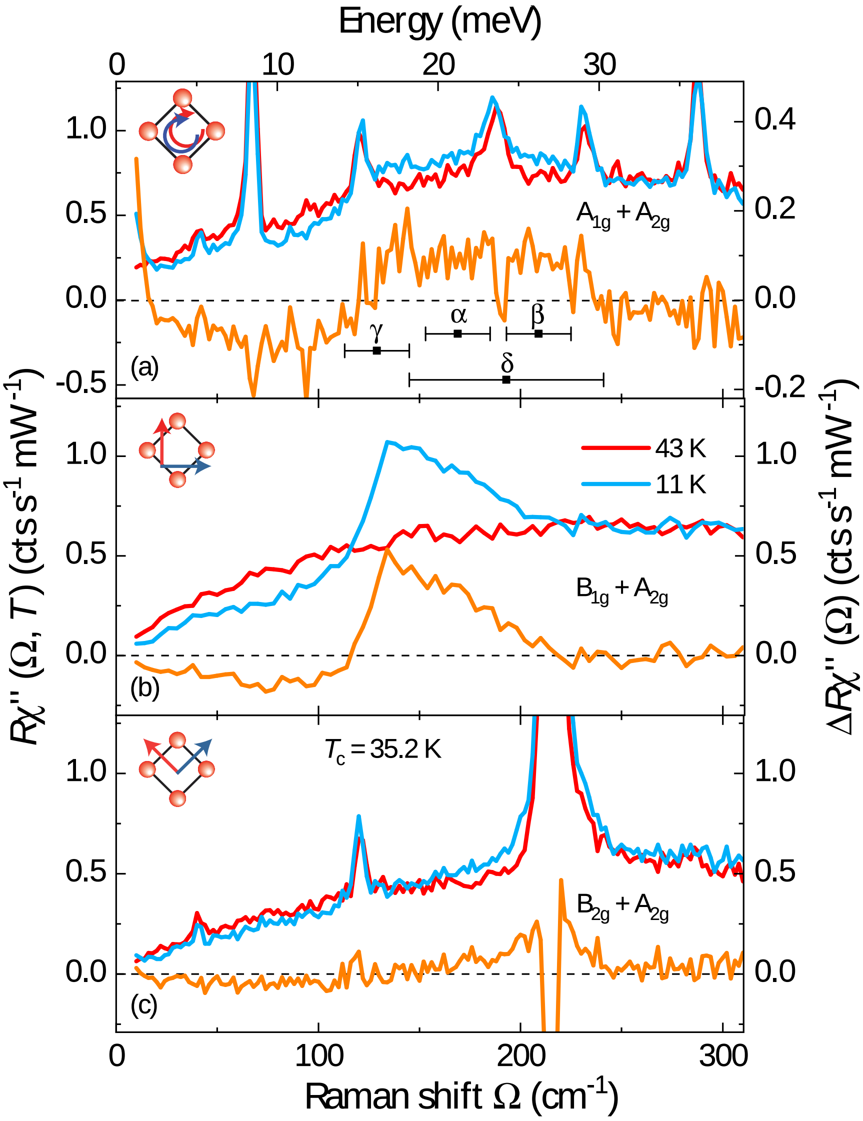

Figure 5.1: Raman response in $CaKFe_4As_4$ for symmetries and polarisations as indicated. The raw data for $T \ll T_c$ and $T > T_c$ are shown in blue and red, respectively. The difference spectra are presented in orange. Phonon modes are present in the $A_{1g}$ and $B_{2g}$ spectra. (a) In $A_{1g}$, the pair-breaking features set in at $\Omega_0^{(A1g)} = 120 \pm 2$ cm$^{-1}$ and extend to $\Omega_m \approx 230$ cm$^{-1}$. The gap energies $2\Delta_i$ for the four bands $i$ observed by angle-resolved photo emission spectroscopy (ARPES) [30] are reproduced as horizontal bars. (b) The $B_{1g}$ pair-breaking features set in at $\Omega_0^{(B1g)} = 116 \pm 5$ cm$^{-1}$. (c) The $B_{2g}$ pair-breaking response lies above $2\Delta_\beta$. The intersection of the normal and superconducting spectra is close to $\Omega_0^{(B2g)} = 130 \pm 5$ cm$^{-1}$. From Ref. [45].

Six and four phonon modes can be observed in $RR$ and $x'y'$ polarisation, respectively which will be discussed in appendix A.3.

In the normal state spectrum in $xy$ polarisation [Fig. 5.1 (b)] no phonon leakage can be detected. Moreover, the response is flat which indicates an absence of impurity scattering inferring a high quality of the crystal. In orange, the difference spectra

$$\Delta R\chi''(\Omega) = R\chi''(T = 11\,\mathrm{K}, \Omega) - R\chi''(T = 43\,\mathrm{K}, \Omega), \tag{5.1}$$

are shown where temperature independent features are subtracted out. The remaining signal stems for the most part from the superconducting response, as described in Subsec. 3.4.1, and illustrates the redistribution of spectral weight in the superconducting state.

In (a), the horizontal bars indicate the gap energies derived from the ARPES measurements by Mou *et al.* [30] (*cf.* Sec. 3.4.1). The magnitude of the superconducting gap derived from the Raman spectra is by and large consistent with the ARPES results. Additionally, the analysis of the temperature dependence below will reveal the subtle hints of a subdominant interband interaction similar to the results in $Ba_{1-x}K_xFe_2As_2$ [24].

## 5.2 Temperature dependence below $T_c$

Fig. 5.2 comprises the inelastic light scattering data $R\chi''(\Omega, T)$ at temperatures as indicated on the left. On the right, the difference spectra $\Delta R\chi''(\Omega, T)$ as defined in Eqn. 5.1 are shown.

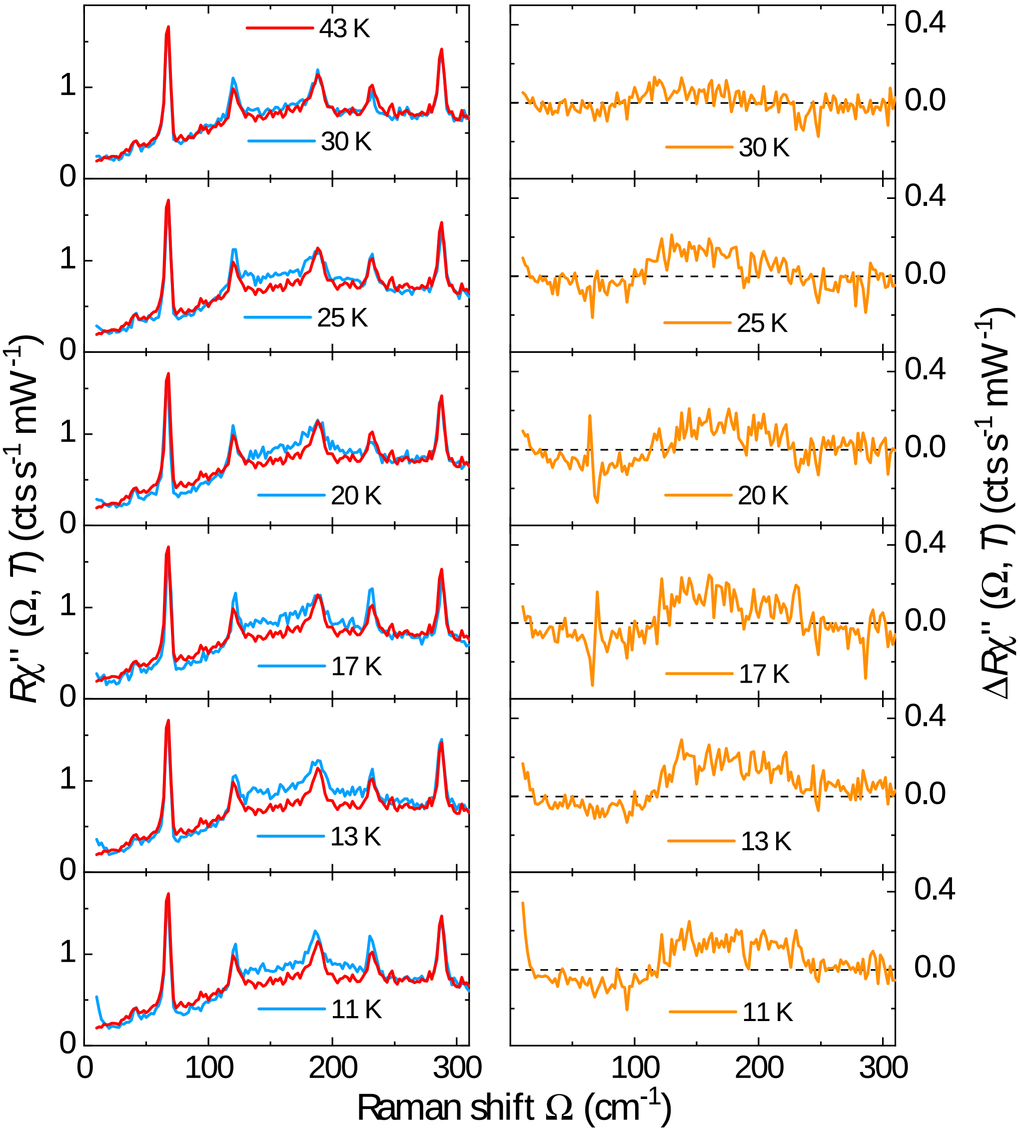

Figure 5.2: $A_{1g}$ response of $CaKFe_4As_4$ for 43 K and temperatures below $T_c$ as indicated. The raw response is shown on the left, the difference spectra on the right. From Ref. [45].

At 11 K, the difference between the normal state and the superconducting spectrum is most pronounced: as the superconducting gap opens up, the spectral weight below a threshold of $\Omega_0 = 120\ \mathrm{cm}^{-1}$ is suppressed. The intensity above the threshold increases due to the breaking of Cooper pairs superposed with a second process in which fermions are lifted above the energy gap, creating a particle-hole excitation. These are called Bogoliubov quasiparticle (BQ) excitations [133]. The gap opening in the difference spectra is characterised by $\Delta R\chi''(\Omega, T) < 0$, and pair-breaking and BQ excitations set in where $\Delta R\chi''(\Omega, T)$ changes sign. The increase in intensity for $\Omega \to 0$ results from diffuse elastic scattering from the sample's surface due to the adsorption of gas molecules. The broad feature of the A$_{1g}$ response collapses as temperature is increased towards the superconducting transition and vanishes almost entirely at 30 K.

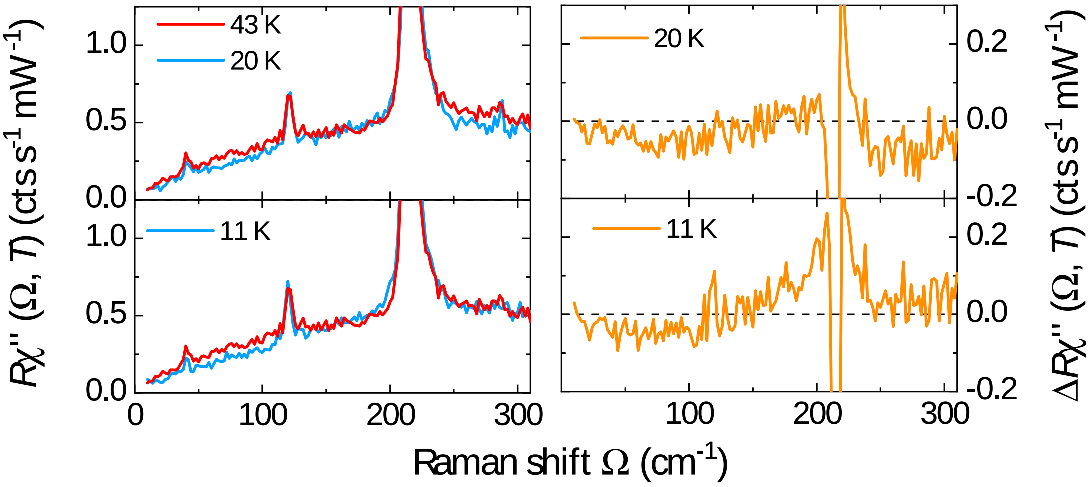

Figure 5.3: B$_{2g}$ response of CaKFe$_4$As$_4$ for 43 K and temperatures below $T_c$ as indicated. The raw response is shown on the left, the difference spectra on the right. From Ref. [45].

The B$_{2g}$ response is weaker and less pronounced than the A$_{1g}$ response as can be seen in Fig. 5.3. Nonetheless, the intersect between the normal and superconducting spectra lies at $\Omega_0 = 130\ \mathrm{cm}^{-1}$, similar to the A$_{1g}$ spectra. The pair-breaking feature extends to $\Omega_m = 250\ \mathrm{cm}^{-1}$ and reaches its maximum at approximately 215 $\mathrm{cm}^{-1}$ which coincides with the energy of the Fe phonon. Already at 20 K, the spectral redistribution is weak.

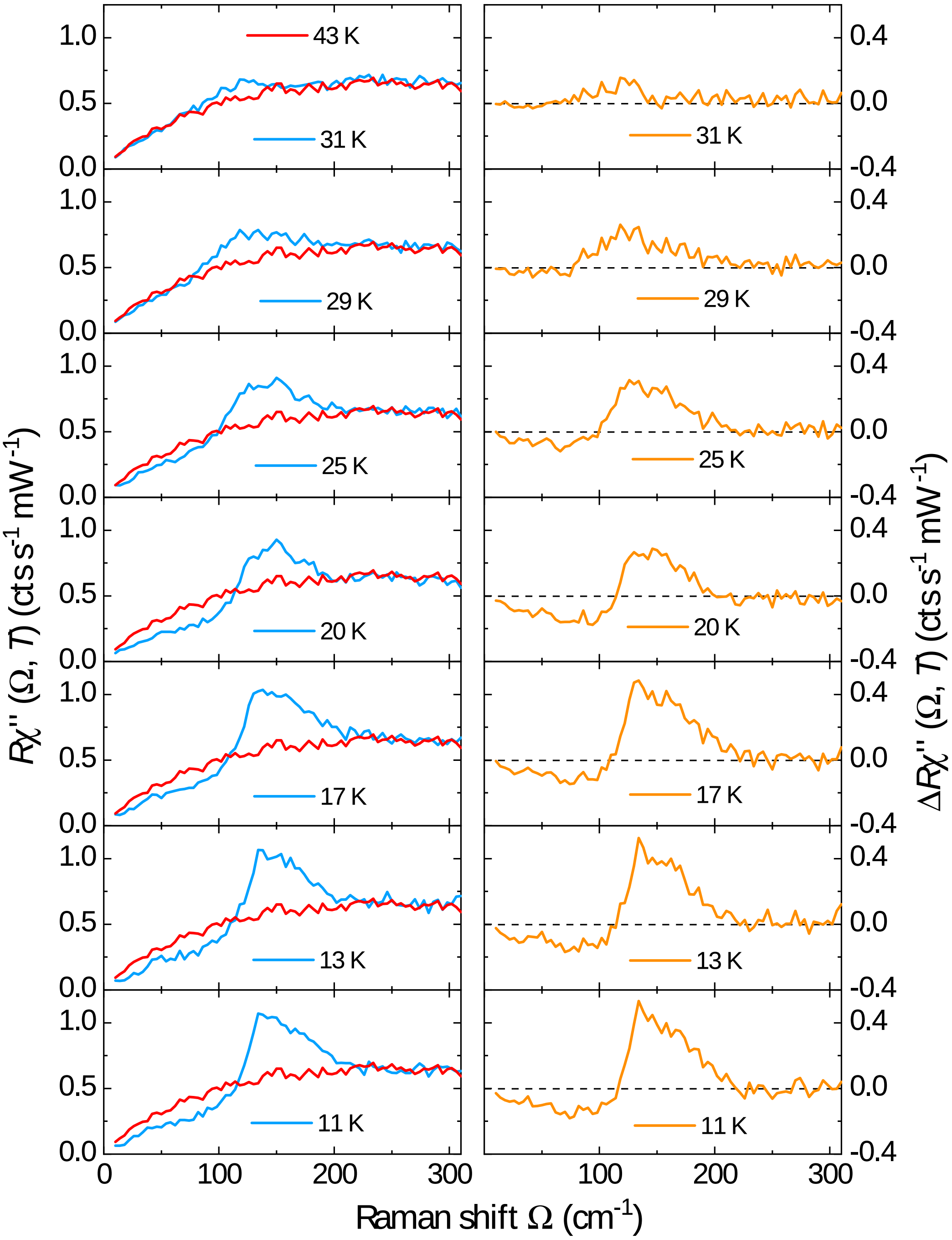

Figure 5.4: $B_{1g}$ response of $CaKFe_4As_4$ for 43 K and temperatures below $T_c$ as indicated. The raw response is shown on the left, the difference spectra on the right. Close to 50 cm$^{-1}$ there is a weak maximum in the superconducting state observable in the raw data and the difference spectra in the temperature range 11-20 K. The superconducting and normal state spectra merge with increasing temperature. From Ref. [45].

In contrast, the superconducting features in $B_{1g}$ symmetry survive up to 31 K as can be seen in Fig. 5.4. At 11 K, the cross-over energy $\Omega_0 = 116$ cm$^{-1}$ is similar to the other symmetries. However, a weak hump at 50 cm$^{-1}$ is visible up to at least 17 K. The pronounced maximum at 135 cm$^{-1}$ at 11 K decreases in intensity and visibly shifts to lower energies as temperature is increased towards 31 K. On the high-energy side there is a second structure at 165 cm$^{-1}$.

## 5.3 Pair breaking and collective modes

To summarise the results above: firstly, the superconducting features in all symmetries emerge at essentially the same energies in the interval $[\Omega_0, \Omega_m]$. Secondly, the redistribution of spectral weight in the range $\Omega_0 < \Omega < \Omega_m$ varies substantially and is entirely different from the typical shape discussed in Subsec. 3.4.1 for all symmetries. It is therefore attempted in this section to discuss this variation in the different symmetries and the subtle deviations of the gap energies from the ARPES results.

We start with the $B_{2g}$ response which shows the highest pair-breaking energy at $2\Delta_{max} \approx 215$ cm$^{-1}$: This pair-breaking energy corresponds to $\Delta_{max} = 13.3$ meV which is slightly larger than the largest average gaps derived from the ARPES data *et al.* [30] (see Tab. 2.1) on the $\beta$ and $\delta$ bands with $\Delta_{\beta,\delta} = 12$ meV. The position of the $B_{2g}$ maximum is consistent with the weak hump in $A_{1g}$ at 215 cm$^{-1}$. Therefore, the ARPES data underestimate the gap energies of the largest gaps found in the Raman experiment which was already observed in $Ba_{1-x}K_xFe_2As_2$ [27, 28], but is overall consistent with view on the experimental error depicted in Fig. 5.1 (a) and reported in Ref. [30].

The lowest gap on the $\gamma$ band with $\Delta_\gamma = 8$ meV coincides with the cross-over energy in the $A_{1g}$ symmetry. Therefore, the peak structure at 11 K in the difference spectra positioned at roughly 140 cm$^{-1}$ is again larger than the smallest gap energy found by ARPES. A signal from the $\gamma$ band is entirely missing in $B_{2g}$ symmetry. There is no clear signal in $A_{1g}$ and $B_{2g}$ symmetry of the gap on the $\alpha$ band with $\Delta_\alpha = 10.5$ meV. Consequently, the maximal gap energies found in the Raman signal are similar to optimally doped $Ba_{1-x}K_xFe_2As_2$ at approximately $9\,k_BT_c$ [28].

The signal in $A_{1g}$ symmetry is by and large compatible with the selection rules shown in Fig. 3.3. From these, it is clear, that similar contributions from all bands should be expected to the spectral weight in $A_{1g}$ symmetry. This holds true, as shown in Fig. 5.1, since the superconducting plateau in $A_{1g}$ symmetry covers the entire energy range.

The $B_{2g}$ spectra partially challenge that view, as the $B_{2g}$ spectra should show contributions from the hole and electron bands with a similar spectral weight. However, only the largest gap is weakly visible. Additionally, the signal from the $\gamma$ band is entirely missing what cannot be explained by the selection rules. Although the peak hight varies as $|\Delta|^2$ [see Ref. [94] and Eqn. 3.22], remnants of the $\gamma$ band should be visible in $B_{2g}$ symmetry. To fully explain the observed response, a phenomenological treatment as outlined in Ref. [28] is needed, including an explicit calculation of the response according to Eqn. 3.22 which, however, is beyond the scope of this work. While the $A_{1g}$ and $B_{2g}$ spectra reproduce the single particle gap energies, the $B_{1g}$ spectra cannot be explained on the basis of pair breaking alone. Firstly, in $B_{1g}$ symmetry, one should capture the full response from the gaps on the $\delta$ bands and only a marginal response from the hole bands at the $\Gamma$ point, if any according to the selection rules in Fig. 3.3. However, the peak energy at 134 $\mathrm{cm}^{-1}$ is well below the maximum gap energies in $A_{1g}$ and $B_{2g}$ symmetries and below the gap energy of the $\delta$ band [Fig. 5.1 (c)]. As the intensities from the hole bands are to be expected marginal in comparison to that of the $\delta$ bands, a scenario in which the maximum stems from the $\gamma$ band can be discarded.

Alternatively, the $B_{1g}$ signal may be considered to not originate solely from the superconducting gaps, but from final state interactions resulting in a strong peak maximum well below $2\Delta_\delta$ as discussed for $Ba_{1-x}K_xFe_2As_2$ in earlier work [24, 27, 28]. Fig. 5.5 directly compares the difference spectra of the Raman response in $B_{1g}$ symmetry of $CaKFe_4As_4$ and $Ba_{0.65}K_{0.35}Fe_2As_2$. Additionally, $2\Delta_\delta$ highlighted by an orange arrow is depicted in Fig. 5.5 (e).

The temperature dependence of the difference spectra in $CaKFe_4As_4$ clearly indicates a shoulder on the high-energy side. The comparison with the data on $Ba_{0.65}K_{0.35}Fe_2As_2$ immediately highlights the similarity of the spectral shapes. On the basis of this comparison, the maximum at 134 $\mathrm{cm}^{-1}$ in $B_{1g}$ symmetry

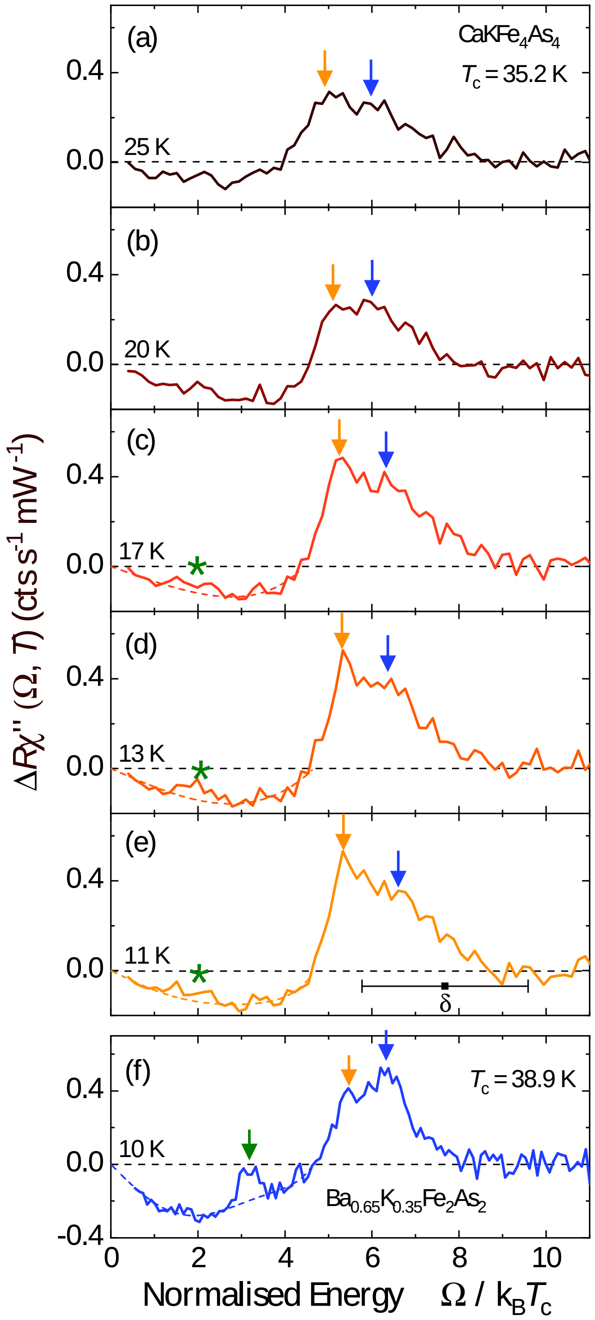

Figure 5.5: Difference spectra of the $B_{1g}$ Raman response. (a)-(e) Difference spectra of $CaKFe_4As_4$. The main peak exhibits a double structure (orange and blue arrows). A second hump is visible from 25 K down to 13 K (green asterisk). (f) Difference spectrum of $Ba_{0.65}K_{0.35}As_2Fe_2$ [24] with two BS modes at 3.1 (green arrow) and 5.2 $k_BT_c$ (orange arrow) and the remainder of the pair breaking peak at 6.2 $k_BT_c$ (blue arrow). Figure taken from Ref. [45].

is identified as a collective mode, as described in Sec. 3.4.1, resulting from a subdominant $d$-wave interaction. This subdominant interaction drains spectral weight from the pair-breaking peak [28,42,104] into a $\delta$-like excitation below the gap edge. Theoretically, this was predicted by Scalapino and Devereaux [42] and experimentally verified in $Ba_{1-x}K_xFe_2As_2$ [24].

Although the overall spectral shape in $CaKFe_4As_4$ is very similar to that of $Ba_{0.65}K_{0.35}Fe_2As_2$, one caveat has to be discussed: in $Ba_{1-x}K_xFe_2As_2$, not one but two subleading channels were found indicated by the green arrow in Fig. 5.5 (f). The faint peak at roughly 50 $cm^{-1}$ in $CaKFe_4As_4$ may be a second collective excitation. The weakness of this peak could be explained, if $CaKFe_4As_4$ was on the brink of a $d$-wave instability. This scenario, although not entirely conclusively demonstrated experimentally, is the most plausible explanation of the peak at 50 $cm^{-1}$. The nesting conditions between the electron pockets in $CaKFe_4As_4$ [see Fig. 2.7 and Ref. [30]] may in fact further enhance the sub-leading channel. The weakness of this mode, however, makes a clear identification difficult. In order to substantiate this claim, a similar analysis as in $Ba_{1-x}K_xFe_2As_2$ [24] has to be conducted.

In summary, the gap energy found in the $B_{2g}$ symmetry at 215 $cm^{-1}$ is in the same range as the gaps derived from the ARPES measurements for the $\beta$ and $\delta$ bands. The superconducting and normal state spectra merge at $\Omega_m = 230$ $cm^{-1}$ in all symmetries. The feature at 215 $cm^{-1}$ is visible in $A_{1g}$ symmetry as well. Additionally, the pair-breaking feature is plateau-like and sets in at $\Omega_0^{(A1g)} = 120\,cm^{-1}$. The plateau covers by and large the entire range of gap energies derived from ARPES [30]. Although the response of individual bands could not be resolved, the results in $A_{1g}$ symmetry are consistent with the ARPES results [30].

The $B_{1g}$ response shows a maximum at an energy lower than that in $A_{1g}$ and $B_{2g}$ symmetry. The sharp maximum at 134 $cm^{-1}$ is interpreted as a collective excitation similar to that in $Ba_{0.65}K_{0.35}Fe_2As_2$. This collective mode is a manifestation of a subdominant $d$-wave interaction resulting from a strong interaction between the electron bands. This mode drains most of the spectral weight from the pair-breaking peak leaving behind only a shoulder at 165 $cm^{-1}$. Whether or not the weak structure at $50\,cm^{-1}$ is another BS mode with even stronger coupling cannot be decided with certainty on the basis of the current results. If this interpretation could be supported further, $CaKFe_4As_4$ would be closer to a $d$-wave instability than $Ba_{1-x}K_xFe_2As_2$. The smaller $T_c$ of $CaKFe_4As_4$ argues in this direction since a strong $d$-wave pairing channel frustrates the $s$-wave ground state and reduces $T_c$.

# Chapter 6

# Quantum criticality in $Ba(Fe_{1-x}Co_x)_2As_2$

In the previous chapter fluctuations were identified as potential players in the context of superconductivity. In addition, the QCP at the critical doping $x_c$ may contribute by enhancing $T_c$. Therefore the study of fluctuations around $x_c$ is a natural continuation of the of the work on Cooper pairing in the preceding chapter. In the discussion two methods for analysing the the low energy part of the spectra will be explored. Parts of this chapter have been published in Ref. [134].

## 6.1 Spectra

In Fig. 6.1 the Raman susceptibility on underdoped $Ba(Fe_{1-x}Co_x)_2As_2$ is depicted as a function of the Raman shift $\Omega$ and temperature $T$ in the range from $T = 333$ K to $T = 26$ K $> T_c = 21.6$ K. The absorbed laser power was set at 2 mW.

In Fig. 6.1 (a), the spectra in $RR$ polarisation project out $A_{1g} + A_{2g}$ symmetry. Superimposed on the particle-hole continuum are three modes, which harden as temperature is decreased. These three modes can be identified as two $E_g$ modes at 125 cm$^{-1}$ and 260 cm$^{-1}$ and one $A_{1g}$ mode at 185 cm$^{-1}$ [135]. The $E_g$ modes are visible due to a finite projection of the polarisation of the incident light on the $c$-axis [107].

The initial slope as well as the overall intensity at low frequencies below $\Omega_\mathrm{m} = 600\ \mathrm{cm}^{-1}$ increases upon decreasing the temperature. Above approximately $\Omega_\mathrm{m}$ the spectra merge.

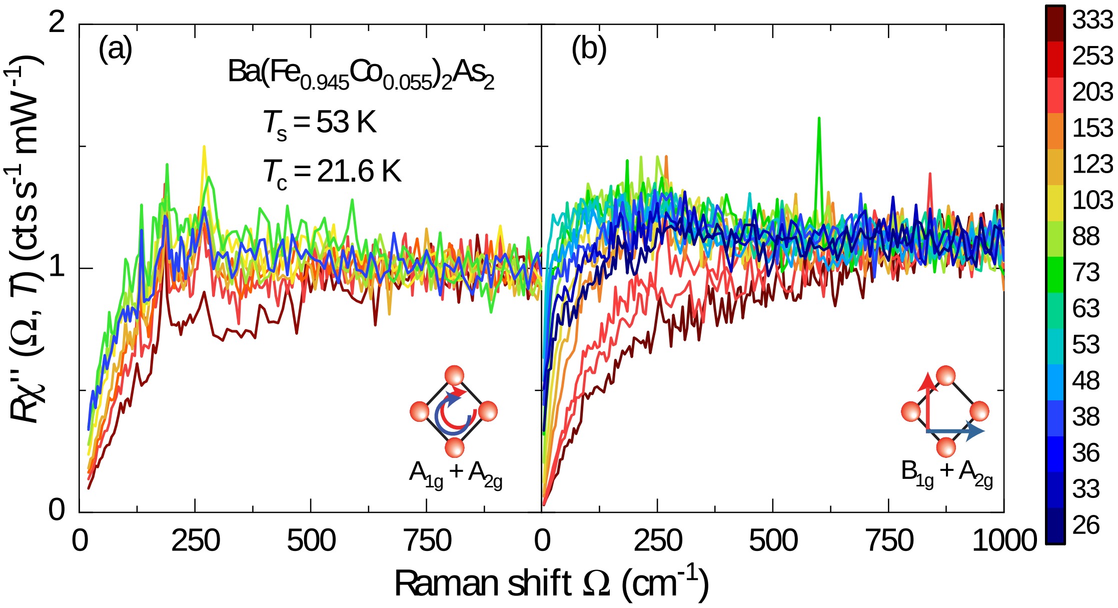

Figure 6.1: Raman response in $\mathrm{Ba(Fe_{0.945}Co_{0.055})_2As_2}$ at temperatures as indicated. (a) In $RR$ polarisation two $\mathrm{E_g}$ phonon modes at $125\,\mathrm{cm}^{-1}$ and $270\,\mathrm{cm}^{-1}$ and the $\mathrm{A_{1g}}$ mode at $185\,\mathrm{cm}^{-1}$ are present. The electronic continuum shows a weak temperature dependence at low energies and is constant for energies above $600\ \mathrm{cm}^{-1}$. (b) For $xy$ polarisation, no phonon modes are observed. The spectral weight at low frequencies increases strongly as temperature decreases down to 53 K. Below 53 K the intensity decreases in the range below $250\ \mathrm{cm}^{-1}$.

Fig. 6.1 (b) displays data from measurements with $xy$ polarisation which projects out the $\mathrm{B_{1g}} + \mathrm{A_{2g}}$ in the 1-Fe unit cell as discussed in Sec. 3.3. Upon cooling from 333 K to 53 K the spectral weight increases in the range up to $\approx 600\,\mathrm{cm}^{-1}$ and a broad peak forms which shifts continuously to lower energies upon cooling. This peak sharpens and reaches its maximum intensity at $T \sim 53\,\mathrm{K}$ below which the spectral weight decreases again. Above $600\ \mathrm{cm}^{-1}$ the spectra are temperature independent.

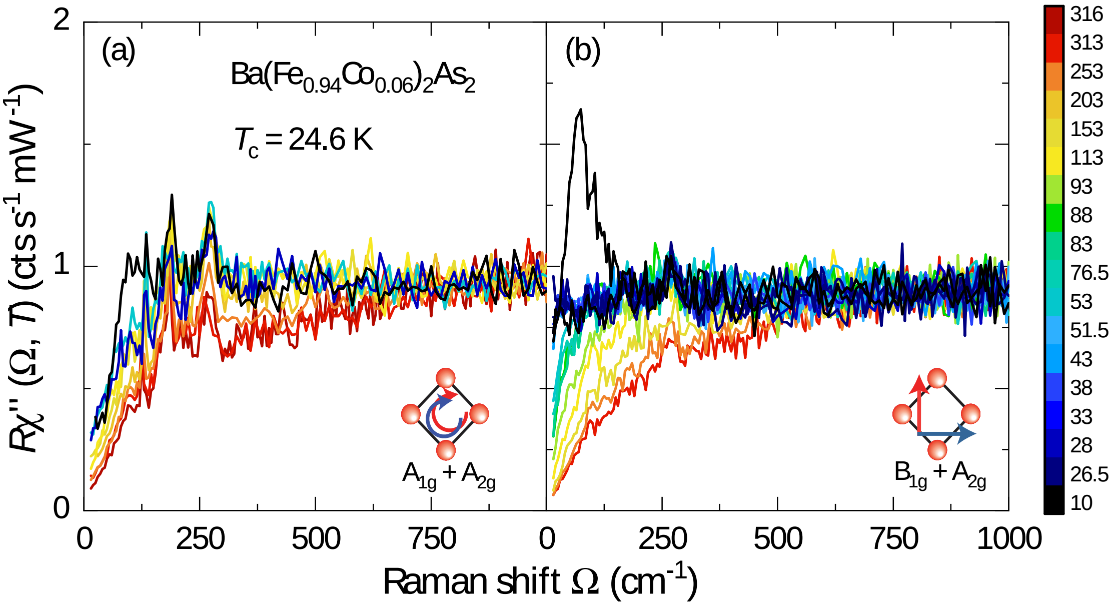

Figure 6.2: Raman response in Ba(Fe$_{0.94}$Co$_{0.06}$)$_2$As$_2$ at temperatures as indicated. (a) Phonon modes are present in $RR$ polarisation with two E$_g$ modes at 125 cm$^{-1}$ and 270 cm$^{-1}$ and the A$_{1g}$ mode at 185 cm$^{-1}$. The electronic continuum shows a weak temperature dependence at low energies and is independent of temperatures above 600 cm$^{-1}$. Superconducting features for $T < T_c$ with a maximum at 95 cm$^{-1}$ can be observed. (b) For $xy$ polarisation an increase of spectral weight is observed as temperature decreases down to 38 K below which the intensity remains constant. Superconducting features are observed for the lowest temperature measured with a maximum at 105 cm$^{-1}$. The strong peak for 10 K results from superconductivity. The spectra are independent of temperature above 600 cm$^{-1}$.

The $RR$ response for Ba(Fe$_{0.94}$Co$_{0.06}$)$_2$As$_2$ in Fig. 6.2 (a) shows in total three phonon modes: the two E$_g$ phonon modes at 125 cm$^{-1}$ and 260 cm$^{-1}$ and the A$_{1g}$ phonon mode at 185 cm$^{-1}$. The low frequency part increases upon cooling for $T > T_c = 24.6$ K. Below $T_c$ at 10 K, a feature is observed at 100 cm$^{-1}$. This stems from pair-breaking as described in Subsec. 3.4.1. The high frequency part of the spectrum starts to merge at $\Omega_m \approx 600$ cm$^{-1}$.

In Fig. 6.2 (b), $xy$ spectra are depicted with the projected symmetries being B$_{1g}$ + A$_{2g}$. At low frequencies, the spectral weight increases as temperature is decreased down to 43 K. For temperatures $T_c < T < 43$ K, the spectra remain constant. Below the critical temperature $T_c$, a peak at 100 cm$^{-1}$ is visible which results from pair-breaking features. The spectra converge above $\Omega_m \approx 600$ cm$^{-1}$.

Fig. 6.3 presents the data of the overdoped sample Ba(Fe$_{0.915}$Co$_{0.085}$)$_2$As$_2$. The $RR$ polarisation is depicted in Fig. 6.3 (a). The three phonon modes of A$_{1g}$, and E$_g$ symmetry are visible at the respective energies. The low frequency part varies with temperature as for Ba(Fe$_{0.945}$Co$_{0.055}$)$_2$As$_2$ and Ba(Fe$_{0.94}$Co$_{0.06}$)$_2$As$_2$ and the spectra converge at high frequencies. Qualitatively different is the B$_{1g}$ response in panel (b) to those of Ba(Fe$_{0.945}$Co$_{0.055}$)$_2$As$_2$ and Ba(Fe$_{0.94}$Co$_{0.06}$)$_2$As$_2$. The low frequency response is less temperature dependent than the B$_{1g}$ data of the under- and optimally doped samples. It increases monotonically towards $T_c$, similar to the low frequency behaviour of the A$_{1g}$ signal depicted panel (a).

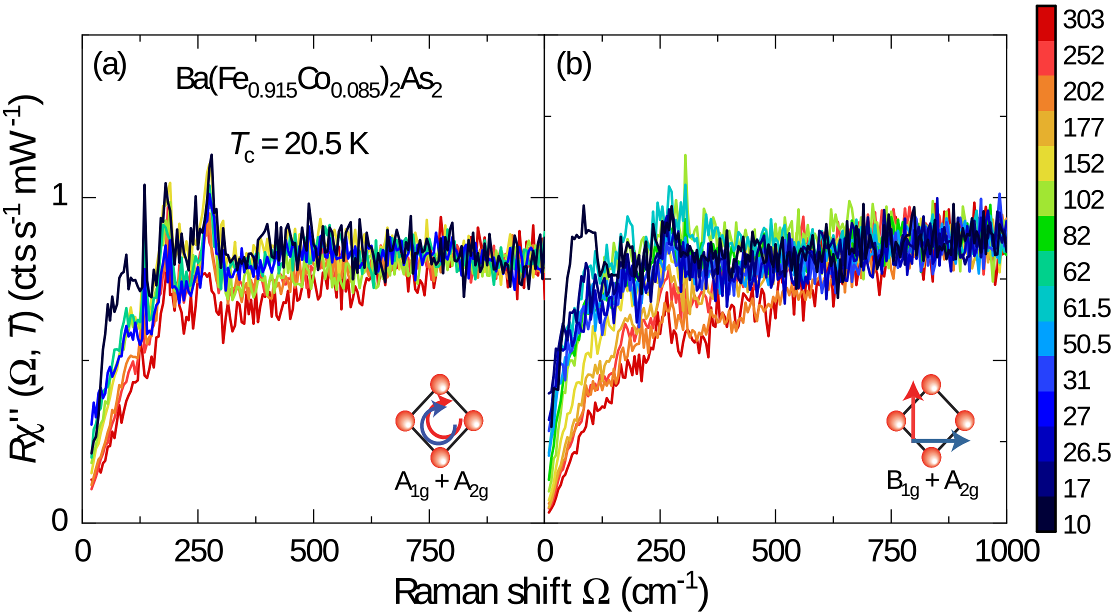

Figure 6.3: Raman response of Ba(Fe$_{0.915}$Co$_{0.085}$)$_2$As$_2$ at temperatures as indicated. (a) In $RR$ polarisation two E$_g$ phonon modes at 125 cm$^{-1}$ and 270 cm$^{-1}$ and the A$_{1g}$ mode at 185 cm$^{-1}$ are observed. The electronic continuum shows a weak temperature dependence above $T_c$. The superconducting spectrum exhibits a maximum at 95 cm$^{-1}$. (b) For $xy$ polarisation, no phonon modes are observed. The low frequency part increases towards $T > T_c$. The signal stemming from superconductivity exhibits a maximum at 85 K.

## 6.2 Analysis

Summarising the results above: The temperature dependence of the electronic continuum in $A_{1g}$ symmetry does not vary with doping. The $A_{1g}$ and $E_g$ phonons harden and sharpen with decreasing temperature for all doping concentrations. The low frequency spectral weight increases as temperature is decreased.

The low-frequency behaviour of the particle-hole continuum in $B_{1g}$ symmetry changes from $x = 0.055$ to $x = 0.060$ and finally to $x = 0.085$ qualitatively and quantitatively. The increase is strongest in Ba(Fe$_{0.945}$Co$_{0.055}$)$_2$As$_2$, where the spectral weight piles up towards 53 K. Then, the intensity decreases monotonically towards the superconducting transition. In Ba(Fe$_{0.94}$Co$_{0.06}$)$_2$As$_2$, the spectral weight increases down to 43 K as well. The intensity over the entire frequency range stays constant down to the superconducting transition at $T_c$. Only in Ba(Fe$_{0.915}$Co$_{0.085}$)$_2$As$_2$, the dichotomy between the $A_{1g}$ and $B_{1g}$ is absent, and the temperature dependence of the continua in both symmetries are similar.

The dichotomy between $A_{1g}$ and $B_{1g}$ channels has been studied in a previous work [44] for doping concentrations $x = 0$, $x = 0.025$ and $x = 0.051$. There, the low frequency pile-up of spectral weight in $B_{1g}$ symmetry was identified as a result of spin-fluctuations driving the nematic transition in underdoped Ba(Fe$_{1-x}$Co$_x$)$_2$As$_2$. Due to the similarities of the Ba(Fe$_{0.945}$Co$_{0.055}$)$_2$As$_2$ and Ba(Fe$_{0.94}$Co$_{0.06}$)$_2$As$_2$ samples with this earlier study, the current data will now be treated in the same fashion as in Ref. [44] and Ref. [97].

### 6.2.1 Relaxation rate analysis

In a first step, the bare fluctuation response shall be separated from the electronic continuum. For this it is assumed, that the $B_{1g}$ Raman response is the sum of two independent contributions,

$$\chi''_{B_{1g}}(\Omega, T) = \chi''_{\text{p-h cont}}(\Omega, T) + \chi''_{\text{fluct}}(\Omega, T) \tag{6.1}$$

i.e. of the particle-hole continuum and the superimposed fluctuation response. Our task is therefore to identify the contribution from the particle-hole excitations which can then be subtracted from the full response. The following recipe will be followed:

1. Extract the dynamic Raman relaxation rate $\Gamma(\Omega, T)$ from the experimental data in $\mathrm{A_{1g}}$ and $\mathrm{B_{1g}}$ symmetry.
2. Calculate the static relaxation rates $\Gamma^0_{\mathrm{A_{1g}}}(T)$ and $\Gamma^0_{\mathrm{B_{1g}}}(T)$.
3. Model the $\mathrm{B_{1g}}$ particle-hole continuum such that the average of the $\mathrm{A_{1g}}$ and $\mathrm{B_{1g}}$ relaxation rates track the in-plane resistivity.
4. Subtract the particle-hole continuum from the full response.

Starting with the first point, the dynamic relaxation rate may be determined by [136]

$$\Gamma(\Omega, T) = R \cdot \frac{\bar{\chi}''(\Omega, T)}{[\bar{\chi}''(\Omega, T)]^2 + [\Omega K(\Omega, T)]} \tag{6.2}$$

in which $\bar{\chi}''(\Omega, T) = \chi''(\Omega, T)/\Omega$ and $R$ is a scaling factor which is fixed by a sum rule [136]. Additionally

$$K(\Omega, T) = \frac{2}{\pi} \mathcal{P} \int_0^{\infty} \frac{\Omega' \bar{\chi}''(\Omega', T)}{\Omega'^2 - \Omega^2} \, \mathrm{d}\Omega' \tag{6.3}$$

is the Kramers-Kronig transform of $\bar{\chi}''(\Omega, T)$. Since the spectra do not converge sufficiently fast, the upper limit of the integral needs to be finite and is typically set at the band width. Fig. 6.4 (a) and (b) depict the dynamic relaxation rates $\Gamma(\Omega, T)$ as a function of temperature extracted via this method from the data shown in Fig. 6.1. The $\mathrm{A_{1g}}$ relaxation rates in panel (a) show a vanishing slope at low frequencies, deviating only at low temperatures. The overall spectral shape changes slightly over the entire temperature range by an offset proportional to the temperature. In contrast, the $\mathrm{B_{1g}}$ spectra in panel (b) show a stark temperature dependence at low frequencies, where the slope vanishes at high temperatures, but becomes finite for decreasing temperature. At high frequencies, both $\mathrm{A_{1g}}$ and $\mathrm{B_{1g}}$ relaxation rates depend on the temperature linearly. Therefore, the dichotomy between the $\mathrm{A_{1g}}$ and $\mathrm{B_{1g}}$ Raman spectra observed at low frequencies extends to the dynamic relaxation rates.

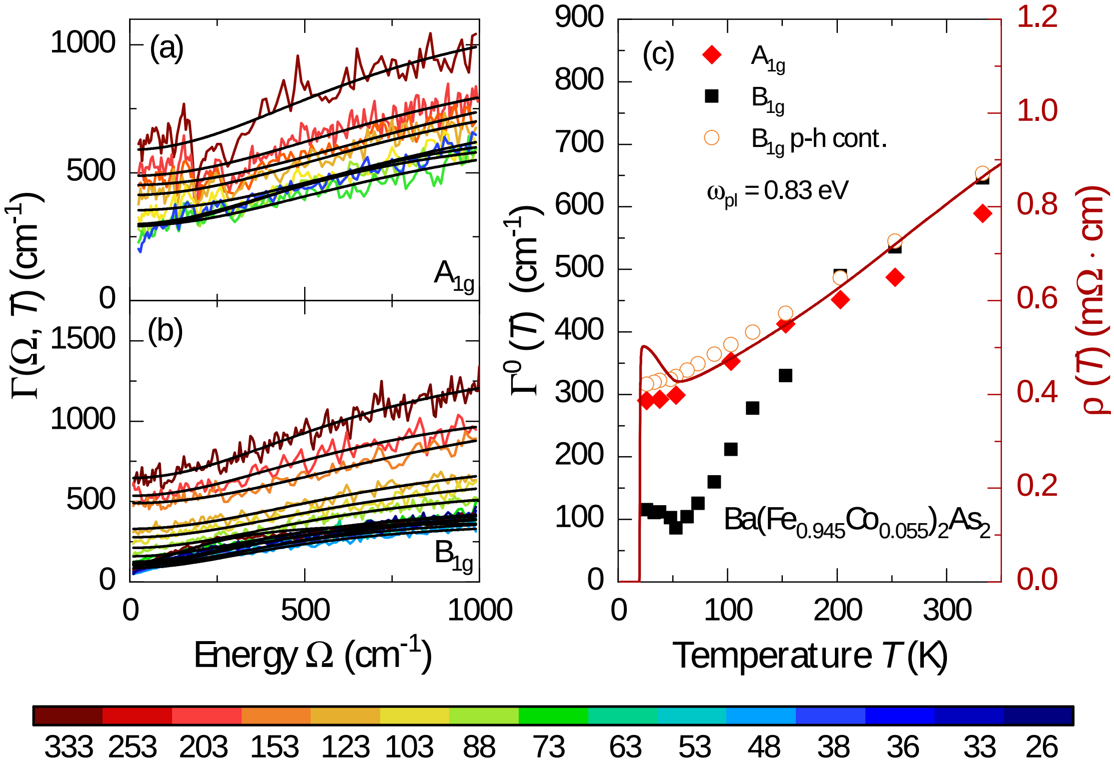

Figure 6.4: Relaxation rate analysis of Ba(Fe$_{0.945}$Co$_{0.055}$)$_2$As$_2$. (a) Dynamic relaxation rate extracted from the $A_{1g}$ data. (b) Dynamic relaxation rate of the $B_{1g}$ data. The black curves show the fits as described by Eqn. 6.5. (c) Static relaxation rate as a function of temperature from the $A_{1g}$ (red diamonds) and $B_{1g}$ (black squares) data. The dark red curve is the resistivity $\rho(T)$ taken from Ref. [22].

In order to systematically extract the $\Omega \to 0$ frequency response, the parallel resistor model is used [137–139]

$$\frac{1}{\Gamma(\Omega, T)} = \frac{1}{\Gamma^0(\Omega, T)} + \frac{1}{\Gamma^{\max}(T)}. \tag{6.4}$$

Here, two contributions to the dynamical relaxation rate $\Gamma(\Omega, T)$ are introduced, where $\Gamma^0(\Omega, T) = \alpha(T) + \beta(T)\Omega^2$ describes the low frequency part and $\Gamma^{\max}(T)$

the high frequency part. Inverting Eqn. 6.4 yields

$$\Gamma^{\text{fit}}(\Omega, T) = \frac{(\alpha(T) + \beta(T)\Omega^2) \cdot \Gamma^{\max}(T)}{\alpha(T) + \beta(T)\Omega^2 + \Gamma^{\max}(T)} \tag{6.5}$$

in which $\alpha(T)$, $\beta(T)$ and $\Gamma^{\max}(T)$ are the fit parameters. The static relaxation rate at $\Omega = 0$ is then given by

$$\Gamma^0(T) = \frac{\alpha(T) \cdot \Gamma^{\max}(T)}{\alpha(T) + \Gamma^{\max}(T)}. \tag{6.6}$$

The result is depicted in Fig. 6.4 (c) as a function of temperature. The red diamonds show the rates $\Gamma^0(T)$ extracted from the $A_{1g}$ data and the black squares those from the $B_{1g}$ data. The dark red curve describes the resistivity $\rho(T)$ as measured by Chu *et al.* [22]. In a Drude model, this resistivity is connected to the static relaxation rate via [136]

$$\Gamma^0(T) = 1.08 \cdot \rho(T) \cdot \omega_{\text{pl}}^2 \tag{6.7}$$

with the plasma frequency $\omega_{\text{pl}}$. Above 200 K, both the $A_{1g}$ and $B_{1g}$ relaxation rates track $\rho(T)$. Below a temperature $T_f \sim 150$ K, $\Gamma^0_{B_{1g}}(T)$ deviates from $\rho(T)$ and $\Gamma^0_{A_{1g}}(T)$. The $B_{1g}$ data decrease, develop a minimum around 50 K and increase only slightly upon moving towards the superconducting transition.

The same analysis was performed for the data of $Ba(Fe_{0.94}Co_{0.06})_2As_2$ and $Ba(Fe_{0.915}Co_{0.085})_2As_2$ (see appendix B.1). The results are collected in Fig. 6.5. $\Gamma^0_{B_{1g}}(T)$ starts deviating from the temperature dependence expected from the resistivity at $T_f \sim 120$ K developing a minimum at 50 K and saturating towards $T_c$ [Fig. 6.5 (b)]. For $Ba(Fe_{0.915}Co_{0.085})_2As_2$ [Fig. 6.5 (c)], $\Gamma^0_{A_{1g}}(T)$ and $\Gamma^0_{B_{1g}}(T)$ both decrease similarly as $\rho(T)$ towards $T_c$, and no deviation can be detected for the $B_{1g}$ channel.

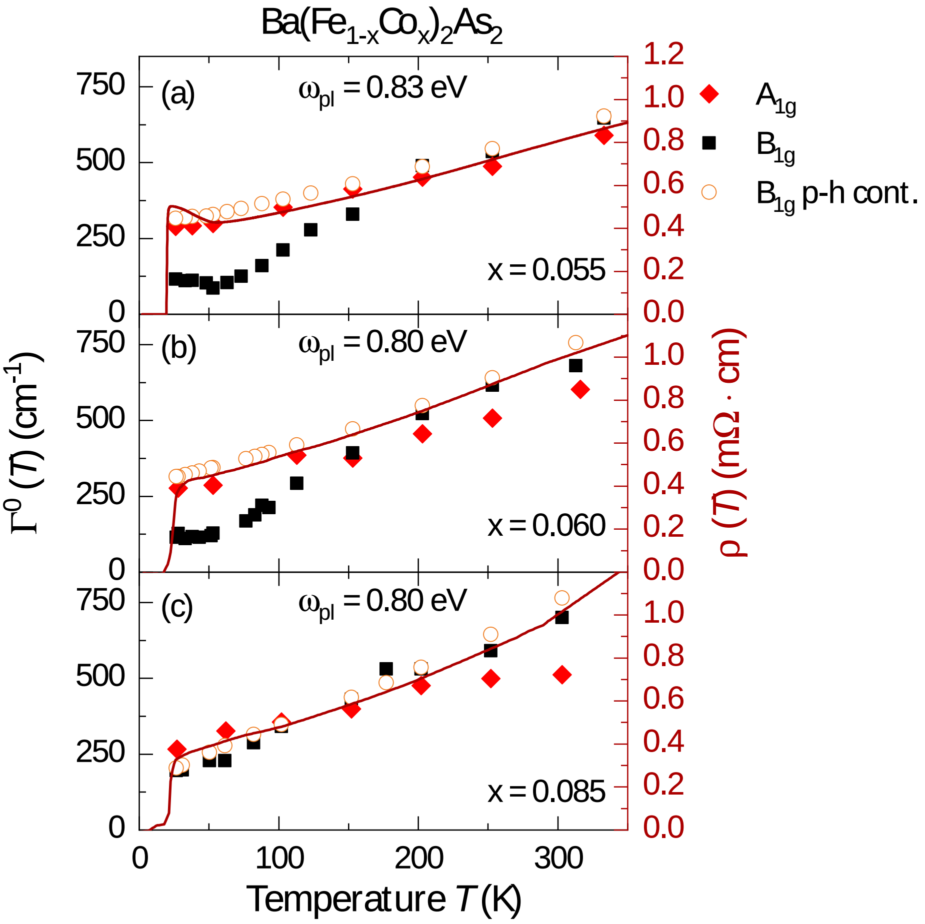

Figure 6.5: Overview of the static relaxation rates for various doping levels and in symmetries as indicated as a function of temperature. The plasma frequencies $\omega_{Pl}$ are in the expected range [140–142].

With this in mind, we start to model the particle-hole continuum given by the phenomenological function

$$\chi''_{B_{1g}}(\Omega) = a \tanh\left[\frac{\Omega}{c}\right] + b\Omega \tag{6.8}$$

which for large Ω becomes $a + b\Omega$. The fit parameters vary with temperature as $a = a1 + a2 \cdot T$ and $b = b1 + b2 \cdot T$ and $c = c1 + c2 \cdot T$. Fitting a high-temperature spectrum first to set the initial parameters, these were then optimised as follows: the static relaxation rate of the analytic approximation to the p-h continuum

[Eqn. 6.8] was calculated and set so that $(\Gamma^0_{A_{1g}}(T) + \Gamma^0_{B_{1g}}(T))/2 \approx \rho(T)$.

The last step is the subtraction of the particle-hole continuum from the full response. Exemplarily, two spectra are depicted showing Ba(Fe$_{0.945}$Co$_{0.055}$)$_2$As$_2$ and Ba(Fe$_{0.94}$Co$_{0.06}$)$_2$As$_2$ in Fig. 6.6 (a) to (d).

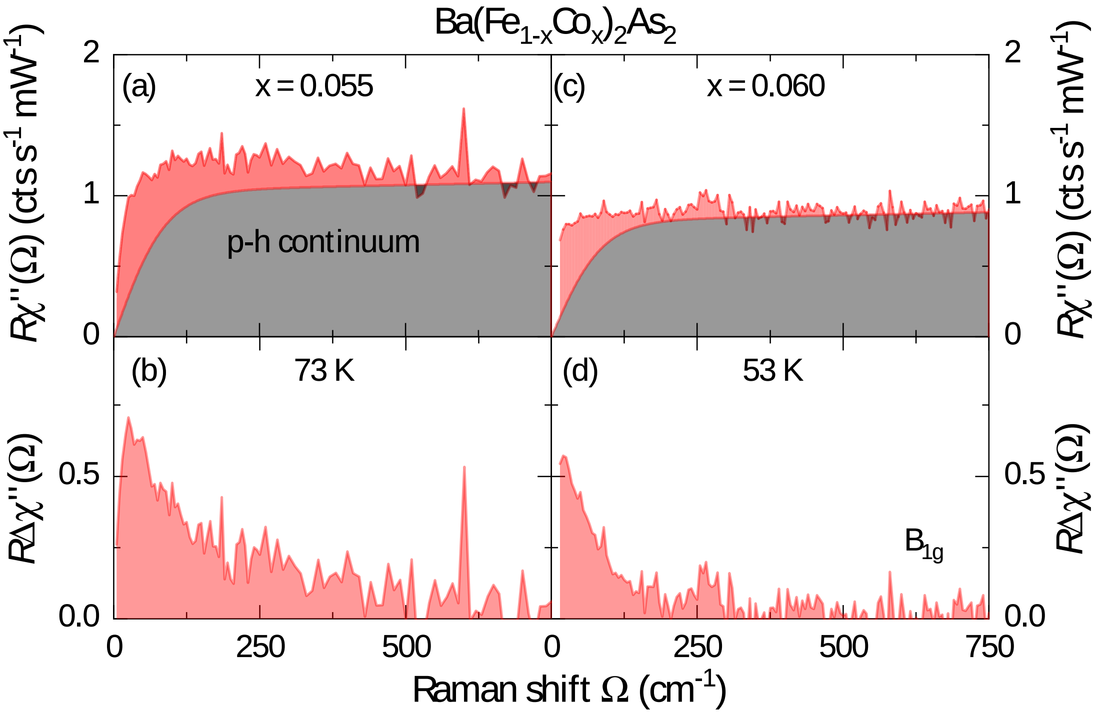

Figure 6.6: Subtraction of the particle-hole continuum from the full response for 73 K and 53 K for Ba(Fe$_{0.945}$Co$_{0.055}$)$_2$As$_2$ and Ba(Fe$_{0.94}$Co$_{0.06}$)$_2$As$_2$, respectively. In (a) and (c) the grey area represents the analytic approximation to the particle-hole continuum given by Eqn. 6.8. The subtraction yields the fluctuation response depicted in (b) and (d).

For the spectrum of underdoped Ba(Fe$_{0.945}$Co$_{0.055}$)$_2$As$_2$ [Fig. 6.6 (a)], the particle-hole continuum described by the grey area deviates from the experimental data in the low frequency regime and merges for energies above $\Omega_m \approx 500$ cm$^{-1}$. The subtraction yields the response of $R\Delta\chi''(\Omega)$ in Fig. 6.6 (b) in which $\Delta\chi''(\Omega \rightarrow 0) = 0$ and a sharp maximum is visible at 25 cm$^{-1}$. Above this energy, the intensity decreases and converges to zero above $\Omega_m$.

The spectra of optimally doped Ba(Fe$_{0.94}$Co$_{0.06}$)$_2$As$_2$ is in agreement with the particle-hole continuum for a larger range, starting at 100 cm$^{-1}$. At low frequencies, the response increases sharply towards $\Omega \to 0$. This is qualitatively different to Ba(Fe$_{0.945}$Co$_{0.055}$)$_2$As$_2$. After being separated from the p-h continuum the low-energy response will be analysed further.

### 6.2.2 Aslamazov-Larkin fluctuations

The spectral shape of $\Delta\chi''(\Omega)$ for Ba(Fe$_{0.945}$Co$_{0.055}$)$_2$As$_2$ is analysed using the analytic expression of Eqn. 3.29 [Sec. 3.4.2]. The procedure to fit the data with this function is followed as described by Caprara *et al.* [43]: first, the spectral shape for the data at one temperature is reproduced by adjusting the mass $m(T)$, the vertex strength $\Lambda_0^2$ and the cut-off frequency $\Omega_0$, where this cut-off is given by a typical phonon frequency [43]. The remaining spectra are then fitted by varying only the mass and keeping $\Lambda_0^2$ and $\Omega_0$ fixed.

Fig. 6.7 (a) and (b) shows the experimental spectra along with the analytic functions in which $\Omega_0$ was set at 350 cm$^{-1}$ consistent with earlier studies [23, 44, 132]. One can distinguish two regimes: (i) the intensity of the fluctuation response increases steadily upon cooling for temperatures above 53 K [Fig. 6.7 (a)]. The response develops from a broad hump at 153 K into a well defined peak which exhibits a maximum at 53 K at an energy of 25 cm$^{-1}$. (ii) The second regime for temperatures below 53 K shows, that the intensity decreases again [Fig. 6.7 (b)]. However, the peak does not vanish and maintains approximately one half of its spectral weight down to 26 K.

The spectra at temperatures $T \geq 53$ K were fitted by varying the mass $m(T)$. For the temperature range $T \leq 48$ K, the spectral shape could not be reproduced any more by only varying the mass $m(T)$. The scaling factor $\Lambda$ had to be varied in order to match the spectral shape.

Since the function in Eqn. 3.29 is defined down to $\Omega = 0$ the initial slope can be readily extracted as

$$\tau_{\mathrm{AL}} \equiv \lim_{\Omega\to 0} \frac{\partial \Delta\chi''_{\mathrm{AL}}(\Omega, T)}{\partial \Omega} \tag{6.9}$$

As can be seen in panel (d), $\tau_{\mathrm{AL}}$ becomes maximal for 53 K and decreases below 48 K but does not vanish down to 26 K.

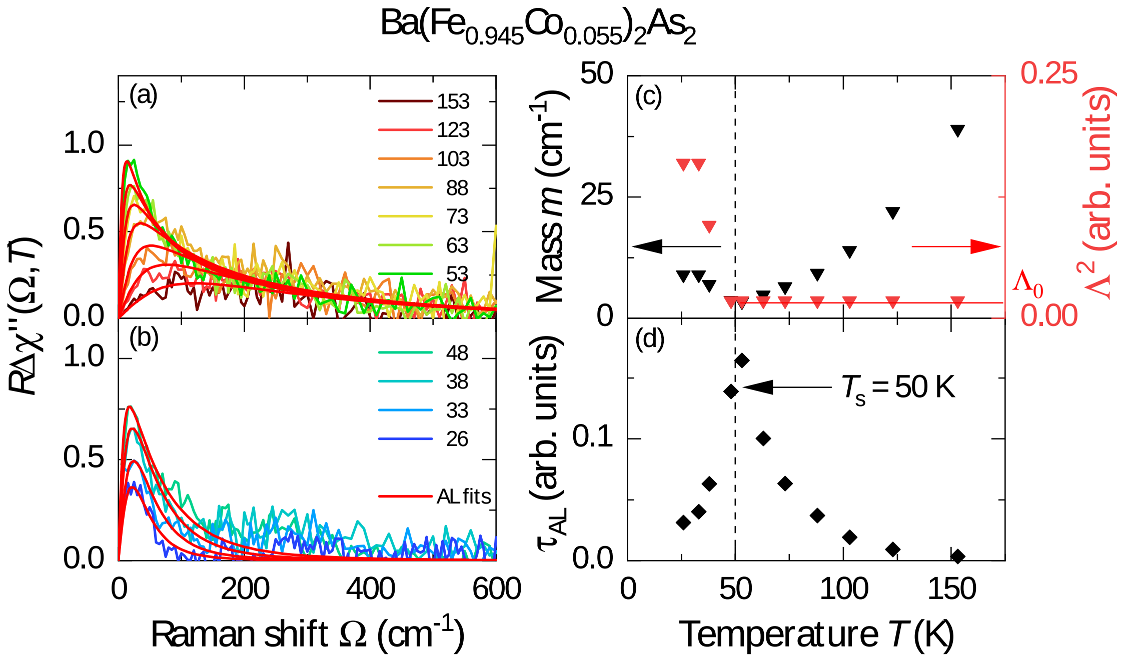

Figure 6.7: Analysis of the fluctuation response in $Ba(Fe_{0.945}Co_{0.055})_2As_2$. (a) The fluctuation response above $T_s$ increases from a broad hump at 154 K into a well defined peak at 53 K, where the intensity become maximal. (b) Below $T_s$, the peak loses intensity, but does not vanish. The straight lines indicate the analytic spectral functions derived from the Aslamazov-Larkin diagrams. (c) The mass $m$ and the scaling factor $\Lambda_0^2$ corresponding to the AL-functions. (d) The initial slope for $\Omega \to 0$ which develops a maximum at 53 K. The dashed line indicates the structural transition temperature $T_s$.

For $Ba(Fe_{0.94}Co_{0.06})_2As_2$, the situation is different. Fig. 6.8 (a) and (b) show the fluctuation contribution. In contrast to the data for $Ba(Fe_{0.945}Co_{0.055})_2As_2$, the hump at high temperatures is not as broad. Upon cooling, the peak sharpens down to 53 K. Below 53 K, the decrease on the high energy side is temperature dependent in that the fall off becomes even steeper. The red lines are the fits by Eqn. 3.29 with the corresponding masses as shown in panel (c). The cut-off had to be set to $\Omega_0 = 85\ \mathrm{cm}^{-1}$ for all temperatures in order to sufficiently reproduce the spectra. In contrast to the results of $Ba(Fe_{0.945}Co_{0.055})_2As_2$, the mass decreases down to the lowest temperature measured without any saturation and extrapolates linearly to $T_s = 0$. The relaxation time $\tau_{AL}$ increases monotonically towards $T_c$. Below $T_c$ the analysis cannot be continued because of the opening of the superconducting gap.

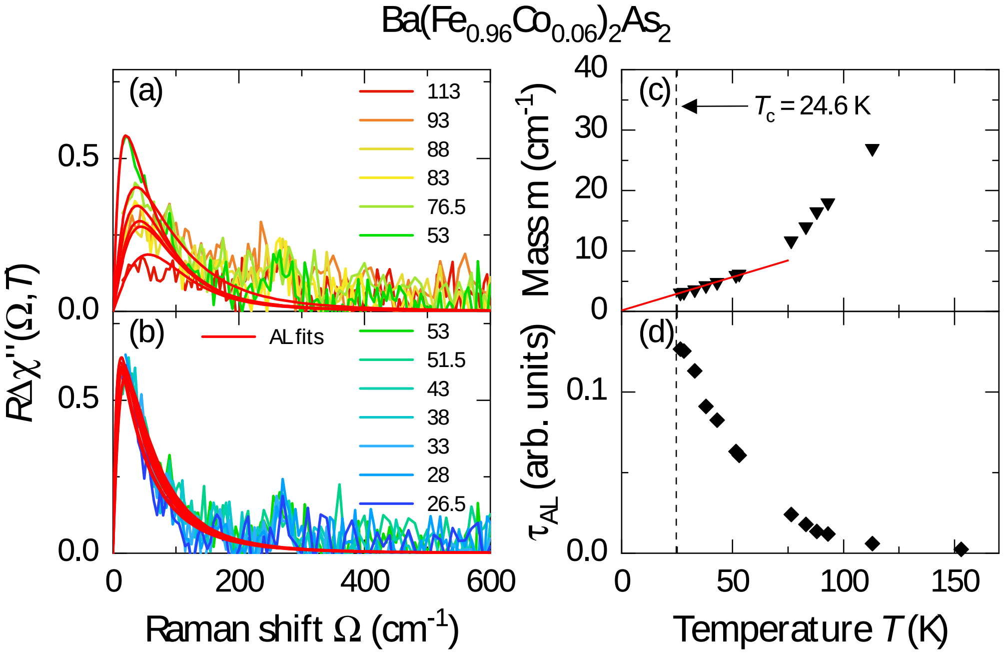

Figure 6.8: Analysis of the fluctuation response in Ba(Fe$_{0.94}$Co$_{0.06}$)$_2$As$_2$. (a) The fluctuations become first visible at 113 K and develop into a sharp peak upon cooling towards 53 K which rapidly falls off as frequency is increased. (b) Below 53 K, the spectra show a weak temperature dependence where the cut-off becomes slightly sharper. The red lines represent fits using Eqn. 3.29. (c) The mass $m(T)$ decreases monotonically and can be extrapolated to zero for low temperatures (red line). (d) The relaxation time $\tau$ increases monotonically towards low temperatures.

### 6.2.3 Imaginary-time dynamics

From the real frequency dynamics, it is possible to extract the imaginary time dynamics, as will be outlined in this section.

Quantities involving the imaginary time are usually not scrutinised in experimental studies. In contrast, theoreticians deploy the transformation $t \longrightarrow -\mathrm{i}t = \tau$ regularly [143, 144] in quantum field theoretical calculations. A pedagogical introduction is given in Ref. [145]. There the substitution $\tau = -\mathrm{i}t$ in the time-dependent Schrödinger equation makes it possible to directly simulate the ground state of the system. Thus, simulations are simplified by the introduction of $\tau$. A problem occurs, when one tries to infer real-time dynamics from the results on the imaginary time axis in order to compare simulations with experiments. This problem is sometimes circumvented by using an analytic continuation, as mentioned in Sec. 3.2 for the derivation of the Raman response.

Lederer *et al.* [134] showed, that one can calculate the imaginary time ordered correlation function $\tilde{\Lambda}(\tau)$ via

$$\tilde{\Lambda}(\tau) = \frac{1}{2\pi} \int \mathrm{d}\Omega \, \chi''(\Omega, T) \, \frac{\exp\left[(\tau - \beta/2)\,\Omega\right]}{\sinh\left[\beta\Omega/2\right]}. \tag{6.10}$$

from the imaginary part of an experimentally derived response function $\chi''(\Omega, T)$ as, for instance, measured by Raman spectroscopy. Here, $\beta = 1/k_{\mathrm{B}}T$ is the inverse temperature and $\tau$ is the imaginary time. $\tau$ is proportional to the inverse temperature $\beta$ and runs in the interval $(0, \beta)$. Example transforms are depicted in Fig. 6.9 (b) where data was published in Ref. [44, 97]. In panel (a) the $B_{1g}$ Raman response of undoped $BaFe_2As_2$ is given for temperatures as indicated. At 325 K, the spectrum is dominated by particle-hole excitations. In the vicinity of the structural phase transition at $T_{\mathrm{s}}$, the low-frequency pile up is maximal and collapses below $T_{\mathrm{s}}$ forming a gap associated with the SDW phase. The full transformation according to Eqn. 6.10 in Fig. 6.9 (b) is depicted as a function of the dimensionless quantity $r = \tau/\beta$.

The possibility to calculate this quantity provides us with an additional tool to investigate the low frequency Raman response dominated by fluctuations. This is because for the longest imaginary time $\tau \sim \beta/2$ given by the Matsubara condition for Fermions, $\omega_n = \pi(2n + 1)/\beta$, Eqn. 6.10 reduces to

$$\tilde{\Lambda}(\beta/2, T) = \frac{1}{2\pi} \int \mathrm{d}\Omega \, \frac{\chi''(\Omega, T)}{\sinh[\beta\Omega/2]}. \tag{6.11}$$

The important point is the factor $1/\sinh[\beta\Omega/2]$ which is depicted in Fig. 6.9 (a) as dashed lines for the indicated temperatures. It resembles a temperature dependent cut-off which collects the spectral contribution for energies of the order of the temperature, $\Omega \sim T$, thereby cutting off the high frequency part of the spectrum.

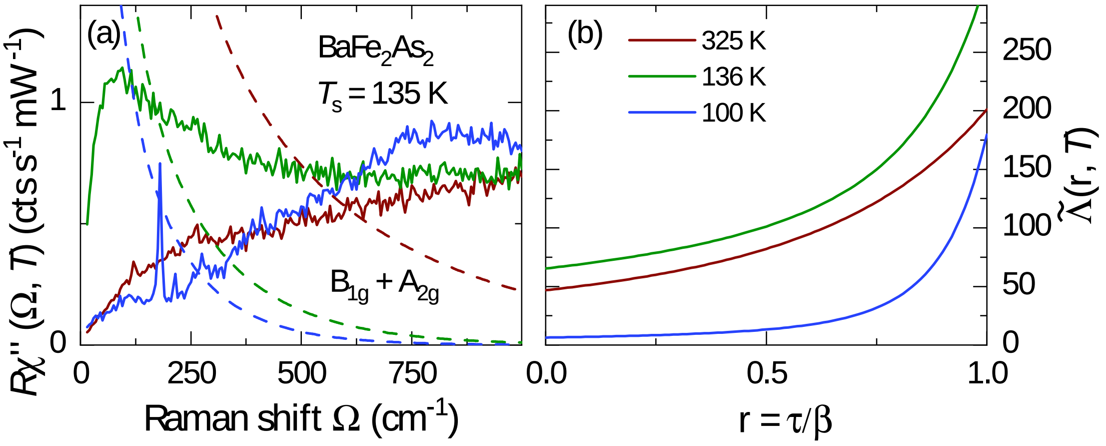

Figure 6.9: Example transformations from real to imaginary frequencies. (a) Raman response of $BaFe_2As_2$ in $B_{1g}$ symmetry. At $T = 325$ K, the continuum is flat. The pile up of spectral weight at low frequencies for $T = 136\text{ K} > T_s$ above the nematic transition collapses below $T_s$, forming the SDW gap. The otherwise forbidden $A_{1g}$ mode is visible in $B_{1g}$ due to the presumably magnetic ordering breaking the Z2 symmetry. From [44]. The dashed lines indicate the cut-off functions for the corresponding temperatures. (b) Imaginary time ordered correlation function $\tilde{\Lambda}(r, T)$ from the experimental Raman data where $r = \tau/\beta$ is a dimensionless quantity. At $\tau = \beta/2$ or $r = 1/2$, this correlation function encapsulates the Raman response for frequencies $\Omega \sim T$.

The quantity $\beta\tilde{\Lambda}(\beta/2, T)$ has an upper boundary in the static susceptibility $\chi'(0, T)$ as derived from the Kramers-Kronig transformation of $\chi''(\Omega, T)$ via

$$\chi'^0(T) \equiv \chi'(0, T) = \frac{1}{\pi} \int d\Omega \, \frac{\chi''(\Omega, T)}{\Omega}. \tag{6.12}$$

The static susceptibility is related to the nematic susceptibility [121]. The relation between $\tilde{\Lambda}^{\beta/2}(T)$ and $\chi'^0(T)$ is easy to see if one considers the series expansion $\sinh[\beta\Omega/2] \approx \beta\Omega/2 + \ldots$ and therefore

$$\tilde{\Lambda}^{\beta/2}(T) \equiv \beta\tilde{\Lambda}(\beta/2, T) \leq \frac{1}{\pi} \int d\Omega \, \frac{\chi''(\Omega, T)}{\Omega} = \chi'(0, T). \tag{6.13}$$

As a second remark, it is noted that the exact calculation of the static susceptibility from the KK transformation is only possible if $\chi''(\Omega)$ converges as $\Omega^{-\epsilon}$ with $\epsilon > 0$ or faster for high frequencies. Otherwise, the integration gives a logarithmically growing contribution to the integral in lowest order, as $\int 1/\Omega$ does not converge. In this case, one needs to introduce an upper cut-off which is not easily justified. In contrast, $1/\sinh[\beta\Omega/2]$ of $\tilde{\Lambda}^{\beta/2}(T)$ converges to zero exponentially fast for high frequencies. Therefore no cut-off is needed. To compare these methods, we apply both transformations to data of underdoped $\mathrm{Ba(Fe_{1-x}Co_x)_2As_2}$ previously under investigation [44].

The transformations calculated from the Raman spectra with Eqn. 6.11 are depicted in Fig. 6.10. $\tilde{\Lambda}^{\beta/2}(T)$ and $\chi'^{0}(T)$ show a similar high-temperature behaviour in $\mathrm{A_{1g}}$ and $\mathrm{B_{1g}}$ symmetry for all doping concentrations. $\tilde{\Lambda}^{\beta/2}_{\mathrm{B_{1g}}}(T)$ and $\chi'^{0}_{\mathrm{B_{1g}}}(T)$ deviate from the $\mathrm{A_{1g}}$ signals at approximately $T_\mathrm{f}$. Upon cooling towards the nematic transition $T_\mathrm{s}$, the $\mathrm{A_{1g}}$ signal stays constant whereas both $\chi'^{0}_{\mathrm{B_{1g}}}(T)$ and $\tilde{\Lambda}^{\beta/2}_{\mathrm{B_{1g}}}(T)$ develop a maximum at $T_\mathrm{s}$ for all doping concentrations. A discontinuity at the magnetic transition temperature $T_\mathrm{SDW}$ can be observed as well for $\tilde{\Lambda}^{\beta/2}(T)$, albeit it is weak for $x = 0.051$. $\tilde{\Lambda}^{\beta/2}_{\mathrm{A_{1g}}}(T)$ vanishes for $T \rightarrow 0$, whereas $\chi'^{0}_{\mathrm{A_{1g}}}(T)$ stays roughly constant over the entire temperature range.

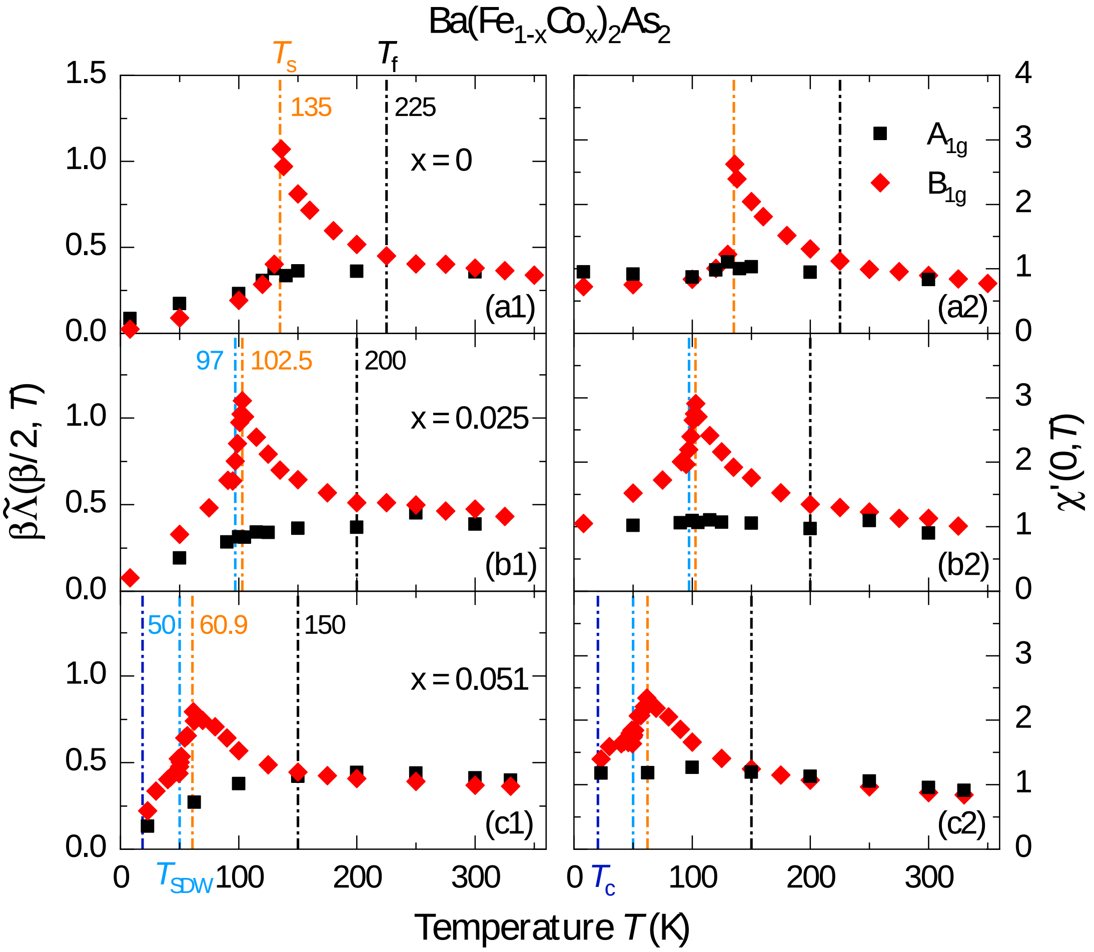

Figure 6.10: Comparison between $\tilde{\Lambda}^{\beta/2}(T)$ (left) and $\chi'(0,T)$ (right) of $Ba(Fe_{1-x}Co_x)_2As_2$ for doping concentrations as indicated with the structural transition temperature $T_s$ and the magnetic transition temperature $T_{SDW}$. The black squares represent the results in $A_{1g}$ symmetry and the red diamonds those in $B_{1g}$ symmetry.

The $\tilde{\Lambda}^{\beta/2}_{A_{1g}}(T)$ and $\tilde{\Lambda}^{\beta/2}_{B_{1g}}(T)$ both vanish for $T \rightarrow 0$, whereas $\chi'^{0}_{A_{1g}}(T)$ and $\chi'^{0}_{B_{1g}}(T)$ remain finite even for low temperatures.

The same analysis is used for the doping concentrations $x = 0.055$, $x = 0.060$ and $x = 0.085$. The results are shown in Fig. 6.11. For $x = 0.055$ [Fig. 6.10 (a1) and (a2)], the $B_{1g}$ signal deviates from the $A_{1g}$ signal at around 153 K for both methods. The signals in $B_{1g}$ symmetry becomes maximal at 53 K what is consistent with a nematic transition temperature $T_s = (50 \pm 2)$ K.

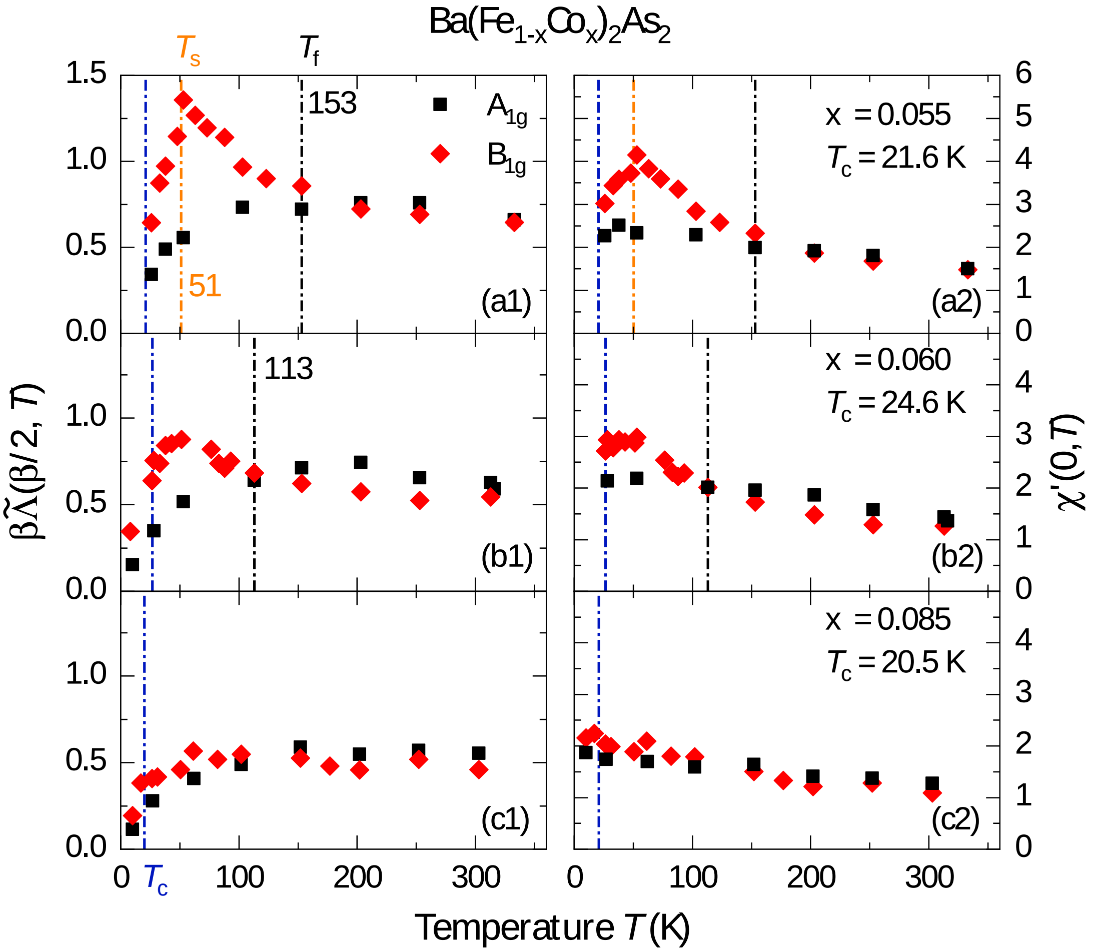

Figure 6.11: Comparison between $\beta\Lambda(\beta/2, T)$ (left) and $\chi'(0, T)$ (right) of $Ba(Fe_{1-x}Co_x)_2As_2$ for doping concentrations as indicated with the structural transition temperature $T_s$ and the magnetic transition temperature $T_{SDW}$. The black squares represent the results in $A_{1g}$ symmetry and the red diamonds those in $B_{1g}$ symmetry.

At optimal doping [panels (b1) and (b2)], the $B_{1g}$ and $A_{1g}$ signals start to deviate from $T_f = 113\,K$ downwards. $\tilde{\Lambda}^{\beta/2}_{A_{1g}}(T)$ goes to zero and $\chi'^{0}_{A_{1g}}(T)$ increases over the entire temperature range. $\tilde{\Lambda}^{\beta/2}_{B_{1g}}(T)$ increases towards 50 K and decreases for decreasing temperature, but does not match $\tilde{\Lambda}^{\beta/2}_{A_{1g}}(T)$ even at the lowest temperatures. $\chi'^{0}_{B_{1g}}(T)$ increases down to 50 K where it saturates.

For the results on the overdoped side, no significant difference between the

$A_{1g}$ and $B_{1g}$ signals can be observed. $\tilde{\Lambda}^{\beta/2}_{A_{1g}}(T)$ and $\tilde{\Lambda}^{\beta/2}_{B_{1g}}(T)$ approach zero for low temperature. $\chi'^{0}_{A_{1g}}(T)$ and $\chi'^{0}_{B_{1g}}(T)$ increase towards zero temperature.

## 6.3 Discussion

The analysis above shows that the temperature dependence of the Raman data in $B_{1g}$ symmetry can be explained in terms of a fluctuation response sitting on top of a particle-hole continuum. To discuss the possible origins of this fluctuation response further, the qualitative change from $Ba(Fe_{0.945}Co_{0.055})_2As_2$ to $Ba(Fe_{0.94}Co_{0.06})_2As_2$ is outlined in the following.

For $Ba(Fe_{0.945}Co_{0.055})_2As_2$, the results for $T > T_s$ are qualitatively similar to those shown in Ref. [44]. The relaxation rate analysis [Fig. 6.4] clearly shows the dichotomy between $A_{1g}$ and $B_{1g}$ symmetry setting in at the fluctuation temperature $T_f = (153 \pm 20)$ K. While $\Gamma^0_{A_{1g}}(T)$ resembles the in-plane resistivity down to $T_s$, $\Gamma^0_{B_{1g}}(T)$ deviates for $T < T_f$ and develops a minimum at 53 K.

For $Ba(Fe_{0.94}Co_{0.06})_2As_2$, the deviation between the $A_{1g}$ and $B_{1g}$ relaxation rates sets in at$T_f = (133 \pm 20)$ K. However, here the relaxation rate does not develop a distinct minimum. Instead, it decreases further towards $T_c$. This first difference hints towards the absence of a nematic phase transition above $T_c$.

The second difference is revealed by the subtraction of the particle-hole continuum. The spectral shape $R\Delta\chi''(\Omega, T)$ of $Ba(Fe_{0.945}Co_{0.055})_2As_2$ has a maximum at 100 $cm^{-1}$ for 153 K which hardens down to $\Omega \sim 25$ $cm^{-1}$ above the nematic phase transition. The data can be fitted with the analytic function derived from AL-fluctuation-like diagrams using the same cut-off $\Omega_0 = 350$ $cm^{-1}$ as for the underdoped compounds [97]. In contrast, the fluctuation response of $Ba(Fe_{0.94}Co_{0.06})_2As_2$ is more narrow, even at high temperatures. The visible peak maximum moves from 50 $cm^{-1}$ at 113 K down to 10 $cm^{-1}$ at 53 K. From the data, one cannot say, if it moves even further down in energy, as the experimental limitation is reached at 5-10 $cm^{-1}$. Nonetheless, the procedure with the AL-description works for a smaller cut-off of $\Omega_0 = 85$ $cm^{-1}$ for all temperatures. The peak maximum lies at most at $(10 \pm 5)$ $cm^{-1}$ which is a factor of 2 lower than for $Ba(Fe_{0.945}Co_{0.055})_2As_2$.

The analysis indicates that Ba(Fe$_{0.945}$Co$_{0.055}$)$_2$As$_2$ undergoes a nematic phase transition around $T_\mathrm{s} \sim 50\,\mathrm{K}$. The general behaviour is consistent with previous studies and we therefore adopt the spin-fluctuation picture for Ba(Fe$_{0.945}$Co$_{0.055}$)$_2$As$_2$. For optimal doping in Ba(Fe$_{0.94}$Co$_{0.06}$)$_2$As$_2$, no other phase transition can be observed above $T_\mathrm{c}$. In the following, it is argued, that the fluctuations are associated with a quantum critical point (QCP). In order to pin down the quantum critical point, we start with the temperature dependence of the mass $m(T,x)$ used in the AL-fits. We deploy [62]

$$m(T,x) = m_0(x) + a(T - T_\mathrm{s})^{2\nu(x)} \tag{6.14}$$

in which $m_0(x)$ is the residual mass at the nematic phase transition and $\nu(x)$ the critical exponent. In the case of a nematic quantum critical point, one should be able to find that the transition temperature at the critical doping $x_c$ approaches zero $T_\mathrm{s} \rightarrow 0$ and that the mass therefore scales with $m(T,x_c) \propto T^{2\nu}$ [62].

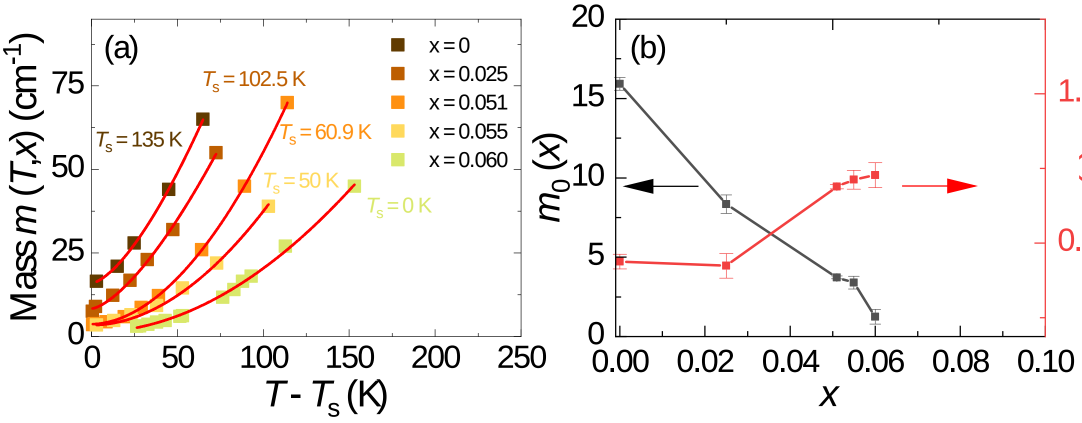

Figure 6.12: (a) Temperature dependent mass $m(T,x)$ for doping concentrations as indicated. The red curves represent fits with Eqn. 6.14. The results of $x = 0$, $x = 0.025$, $x = 0.051$ were taken from Ref. [62]. (b) The residual mass $m_0(x)$ derived from the fit decreases with increased doping. The critical exponent $\nu(x)$ increases from $\nu(0) = 0.75$ to almost unity at $\nu(x_c = 0.060) = 0.98$ for optimally doped Ba(Fe$_{0.94}$Co$_{0.06}$)$_2$As$_2$.

The fits with Eqn. 6.14 are depicted in Fig. 6.12 (a) as red lines with the nematic transition temperature of Ba(Fe$_{0.94}$Co$_{0.06}$)$_2$As$_2$ at $T_\mathrm{s} = 0$. Both, the results of $Ba(Fe_{0.945}Co_{0.055})_2As_2$ and $Ba(Fe_{0.94}Co_{0.06})_2As_2$ are reproduced well. The doping dependence of the residual mass $m_0(x)$ and the critical exponent $\nu(x)$ are depicted in Fig. 6.12 (b). $m_0(x)$ decreases monotonically as a function of doping $x$, whereas the critical exponent $\nu(x)$ increases and almost reaches unity at $x_c$. Additionally, the initial slope $\tau_{AL}(T, x)$ is depicted in Fig. 6.13. The initial slope increases as a function of doping suggesting, that the magnitude of fluctuations increases.

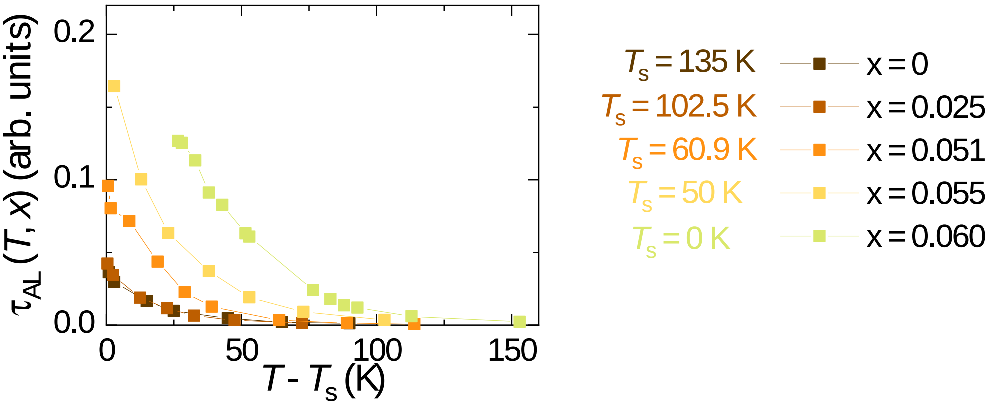

Figure 6.13: Initial slope $\tau(x)$ from the AL-fits which increases as a function of doping and is largest for the optimally doped $Ba(Fe_{0.94}Co_{0.06})_2As_2$.

The last two arguments for the quantum critical fluctuations originate from the imaginary time formalism. A QMC simulation of $\tilde{\Lambda}(\beta/2)$ for a nematic quantum critical point by Sam Lederer [146] suggests, that $\tilde{\Lambda}(\beta/2)$ diverges with $T \to 0$. However, pinning down this divergence in the experiment proofs to be challenging, as the numerical cut-off of $\tilde{\Lambda}(\beta/2)$ requires knowledge of the response below the experimental cut-off at $\Omega \approx 10$ cm$^{-1}$. This prevents a clear divergence of $\tilde{\Lambda}^{\beta/2}_{B_{1g}}(T)$ for $T \to 0$ at optimal doping $x_c$ and results in a hump for $T > T_c$. In the absence of any other phase transition apart from superconductivity in $Ba(Fe_{0.94}Co_{0.06})_2As_2$, this is associated with the fluctuations from a zero temperature phase transition.

Furthermore, a more qualitative argument enables us to make a suggestion about the spectral shape of the Raman response. Close to a QCP, the bosonic correlator reads [134]

$$\tilde{\Lambda}(\tau) = A\left[\frac{1}{|\tau|^{\nu}} + \frac{1}{|\beta - \tau|^{\nu}}\right] \tag{6.15}$$

where $A$ is a constant, $\tau$ the imaginary time and $\beta$ the inverse temperature. From this, one derives the expression for the imaginary part of the response function $\chi''(\Omega)$,

$$\chi''(\Omega) = \frac{A}{T^{1-\nu}} F(\beta\Omega) \tag{6.16}$$

where $F(\beta\Omega)$ is the scaling function:

$$F(\beta\Omega) = \frac{\pi\beta\Omega}{\Gamma(\nu)}\left|\frac{1}{\beta\Omega}\right|^{2-\nu} \left[1 - \exp\left[-|\beta\Omega|\right]\right] \tag{6.17}$$

with the Gamma function $\Gamma(\nu)$. From the mass we derive the critical exponent $\nu \approx 1$. For energies $T << \Omega << \Omega_c$ where $\Omega_c$ is an ultraviolet cut-off, Eqn. 6.16 yields a power-law behaviour,

$$\chi''(\Omega) \sim \frac{\Omega}{|\Omega|^{2-\nu}}. \tag{6.18}$$

For $\nu \sim 1$, $\chi''(\Omega)$ is a constant which describes the raw data for temperatures $T < 53\,\mathrm{K}$. To conclude, the fluctuation response in $\mathrm{Ba(Fe_{0.945}Co_{0.055})_2As_2}$ fits in with previous results. The signal stems most likely from spin-fluctuations. The fluctuation response in $\mathrm{Ba(Fe_{0.94}Co_{0.06})_2As_2}$ is best explained with the occurrence of quantum critical fluctuations. As the nematic transition temperature at optimal doping can be estimated to approach zero from the doping dependence of the mass [see Fig. 6.12], the corresponding QCP can be classified as a nematic quantum critical point. To illustrate the interplay of fluctuations and superconductivity, consider the phase diagram of $\mathrm{Ba(Fe_{1-x}Co_x)_2As_2}$ in Fig. 6.14.

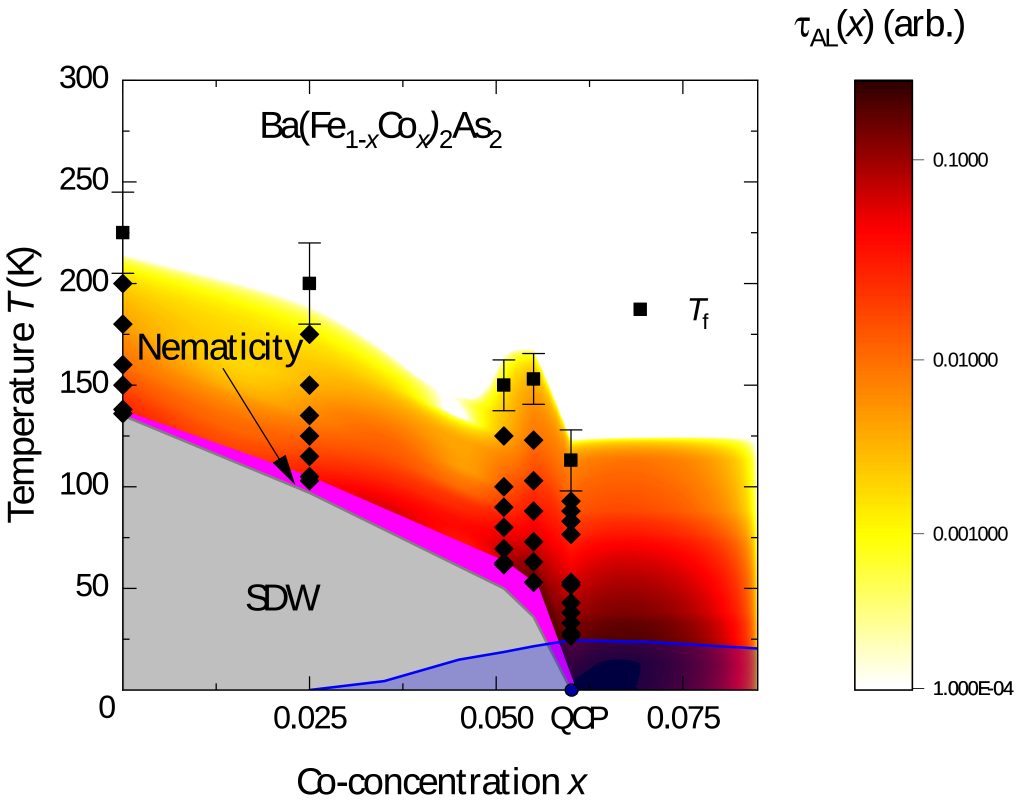

Figure 6.14: Phase diagram of $Ba(Fe_{1-x}Co_x)_2As_2$. The grey area is the region of the spin-density-wave, the magenta stripe corresponds to the nematic phase and the transparent blue area to superconductivity. The colour gradient indicates the fluctuations and relates to the magnitude of $\tau_{AL}(x)$ [black diamonds from Fig. 6.13 (b)] which increases towards optimal doping at the putative QCP (blue dot) and decreases on the overdoped side. The data for $x \leq 0.051$ were published in Ref. [44].

The area coloured in shades of red indicates the value of $\tau_{AL}(x)$ which was extrapolated from the data in Fig. 6.13, and particularly in the region beneath the superconducting dome. The data were extrapolated on the overdoped side where $T_c$ decreases by considering, that the fluctuations vanish in $Ba(Fe_{0.915}Co_{0.085})_2As_2$. The strength of fluctuations increases towards and is largest at optimal doping where $T_c$ is largest. This concomitant doping dependence of $T_c$ and $\tau_{AL}(x)$ may indicate, that critical fluctuations play a role in the formation of Cooper pairs in superconducting $Ba(Fe_{1-x}Co_x)_2As_2$.

# Chapter 7

# Summary

Cooper pairing in unconventional superconductors remains one of the major challenges in condensed matter physics. The relevant interactions are much harder to pin down than in conventional systems. It is the purpose of this thesis to access the related interactions by Raman spectroscopy. For the analysis of the low-energy spectra a novel method is developed, applied and tested. Critical fluctuations of spin or charge are studied and identified in $Ba(Fe_{1-x}Co_x)_2As_2$ and may contribute to the pairing, at least close to optimal doping. The spectra of $CaKFe_4As_4$ suggest the existence of a similar hierarchy of pairing channels as in $Ba_{1-x}K_xFe_2As_2$.

In stoichiometric $CaKFe_4As_4$, the electronic continuum was studied above and below the superconducting transition temperature $T_c$ in three polarisation configurations projecting $A_{1g}$, $B_{1g}$ and $B_{2g}$ symmetries with individual sensitivities in momentum space. Below $T_c$, a redistribution of spectral weight from below to above the gap energy was observed in all three symmetries. The spectral shapes vary across the symmetries. The weakest redistribution was found in $B_{2g}$ symmetry having the intensity maximum at an energy close to the largest superconducting gaps derived from angle-resolve photoemission spectroscopy (ARPES). The superconducting feature in the $A_{1g}$ signal is broad and shows contributions from all bands in agreement with the Raman selection rules. In contrast, a well-defined peak appears in $B_{1g}$ symmetry at 134 $cm^{-1}$. This energy is substantially lower than expected from the results in $A_{1g}$ and $B_{2g}$

symmetry. On the high-energy side of the $B_{1g}$ peak there is a hump at an energy roughly corresponding to the energy gap on the electron pockets. In analogy to $Ba_{0.65}K_{0.35}Fe_2As_2$ the maximum at 134 $cm^{-1}$ was interpreted in terms of a Bardasis-Schrieffer (BS) exciton resulting from a competing sub-leading $d_{x^2-y^2}$-wave interaction. The weak hump at 50 $cm^{-1}$ well below the peak maximum was tentatively assigned to a second BS mode. The low absolute energy and small spectral weight suggest a substantially higher binding energy indicating, that $CaKFe_4As_4$ may even be closer to a $d$-wave instability than $Ba_{0.65}K_{0.35}Fe_2As_2$.

The symmetries of the ground state and of the sub-leading channels argue for unconventional pairing in the pnictides but do not specify any origin of the respective instabilities. As fluctuations indicate an enhanced susceptibility and have been identified to boost $T_c$, the temperature and symmetry dependence of the fluctuations was studied in $Ba(Fe_{1-x}Co_x)_2As_2$. In three superconducting samples having $x = 0.055$, 0.060 and 0.085 the response was measured in detail below 500 $cm^{-1}$. The low-frequency part in $A_{1g}$ spectra increases monotonically with decreasing temperature as expected from the resistivity. In contrast, the $B_{1g}$ signals of $Ba(Fe_{0.945}Co_{0.055})_2As_2$ and $Ba(Fe_{0.94}Co_{0.06})_2As_2$ change drastically below the onset temperature of fluctuations $T_f$. In $Ba(Fe_{0.915}Co_{0.085})_2As_2$, the temperature dependence of the $B_{1g}$ and $A_{1g}$ signal are similar, and the low-energy parts track the resistivity. This indicates that the fluctuations are superimposed on the particle-hole continuum and vanish in the range $0.060 < x \leq 0.085$. The bare fluctuation response can be isolated and reproduced using a model function on the basis of Aslamazov-Larkin (AL) diagrams. The temperature dependence of the model function facilitates the derivation of the nematic transition temperature in $Ba(Fe_{0.945}Co_{0.055})_2As_2$ to be $T_s = (50 \pm 2)$ K.

The low-frequency spectra are further analysed by deriving the response for imaginary times from the real frequency Raman data. The method is applied in the doping range $0 \leq x \leq 0.085$ and revealed signatures of fluctuations for $x \leq 0.060$ but not for $Ba(Fe_{0.915}Co_{0.085})_2As_2$. For $x = 0.06$ the nematic transition temperature is determined to approach zero arguing for the existence of a nematic QCP in $Ba(Fe_{1-x}Co_x)_2As_2$. The fluctuation strength as well as $T_c$ enhancement towards optimal doping and decrease for $x > 0.06$ indicate a possible contribution of critical fluctuations to the Cooper pairing in $Ba(Fe_{1-x}Co_x)_2As_2$.

# Appendix A

# Phonons in $CaKFe_4As_4$

This appendix completes the analysis of the $CaKFe_4As_4$ Raman data. First, the possible eigenvectors are presented in comparison to those in $BaFe_2As_2$ [135]. Then, the phonon lines are identified in the Raman spectra. The temperature dependences of the phonons in $A_{1g}$ symmetry are analysed by extracting the peak energy $\Omega_c(T)$ and the linewidth $\Gamma(T)$.

At least two phonon modes observed in $A_{1g}$ symmetry show signs of a finite electron-phonon coupling (EPC). The total EPC constant $\lambda$ of the Raman-active phonons in $CaKFe_4As_4$ was estimated.

## A.1 Number of phonons and eigenvectors

The primitive unit cell of $CaKFe_4As_4$ is twice as large as that of $BaFe_2As_2$. This, in turn doubles the number of Raman-active phonons in $CaKFe_4As_4$. This can be well understood with the following argument: the base vectors which project the unit cell onto themselves are $(a/2, b/2, c/2)$ and $(a, b, c)$ in $BaFe_2As_2$ and $CaKFe_4As_4$, respectively. In-phase vibrational modes occur, if, and only if, the atoms of these unit cells are projected onto themselves. In the case of the $CaKFe_4As_4$, this disentangles the As(1) and As(2) as well as the Fe planes giving rise to two additional $A_{1g}$ and two additional $E_g$ modes.

Using the Bilbao server [147] one can extract the number of Raman-active phonons from the Wyckoff positions of the atoms. The results are collected in

Tab. A.1 and Tab. A.2 for $BaFe_2As_2$ and $CaKFe_4As_4$, respectively.

Table A.1: Raman-active phonons in $BaFe_2As_2$. Wyckoff positions taken from [4].

| Wyckoff position | atom | $A_{1g}$ | $A_{2g}$ | $B_{1g}$ | $B_{2g}$ | $E_g$ |
|---|---|---|---|---|---|---|
| 2a | Ba | - | - | - | - | - |
| 4d | Fe | - | - | 1 | - | 1 |
| 4e | As | 1 | - | - | - | 1 |

Table A.2: Raman-active phonons in $CaKFe_4As_4$. Adapted from Ref. [47]. Wyckoff positions from Ref. [30].

| Wyckoff position | atom | $A_{1g}$ | $A_{2g}$ | $B_{1g}$ | $B_{2g}$ | $E_g$ |
|---|---|---|---|---|---|---|
| 1a | Ca | - | - | - | - | - |
| 1d | K | - | - | - | - | - |
| 4i | Fe | 1 | - | 1 | - | 2 |
| 2g | As(1) | 1 | - | - | - | 1 |
| 2h | As(2) | 1 | - | - | - | 1 |

Fig. A.1 shows the $B_{1g}$ phonon which stems from the displacement of the out-of-phase vibrations of the Fe atoms in each layer. The $B_{1g}$ phonon branch does not change from $I4/mmm$ to $P4/mmm$.

Fig. A.2 shows the displacement of the As atoms changing from $BaFe_2As_2$ in (a) to $CaKFe_4As_4$ in (b)-(d). While $BaFe_2As_2$ allows only for the eigenvectors as indicated, $CaKFe_4As_4$ frees up the As(1) layers to move either in-phase or out-of-phase with the As(2) layers. We will denote the former as $A_{1g}^{(As(1))}$ and the latter as $A_{1g}^{(As(2))}$ mode.

Additionally, the Fe atoms of each layer may vibrate in-phase giving rise to the third mode denoted as $A_{1g}^{(Fe)}$. Fig. A.3 shows the displacement of the Fe and As layers which result in phonons of $E_g$ symmetry. There are two $E_g$ phonons in $BaFe_2As_2$. The same argument as above ($CaKFe_4As_4$ unit cell is twice as large as the $BaFe_2As_2$ unit cell) applies, which results in the four $E_g$ modes in $CaKFe_4As_4$.

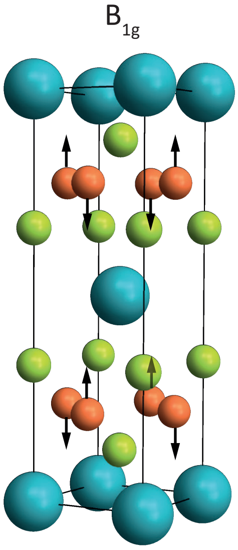

Figure A.1: $B_{1g}$ phonon branch for $CaKFe_4As_4$ and $BaFe_2As_2$. The Fe atoms vibrate out-of-phase.

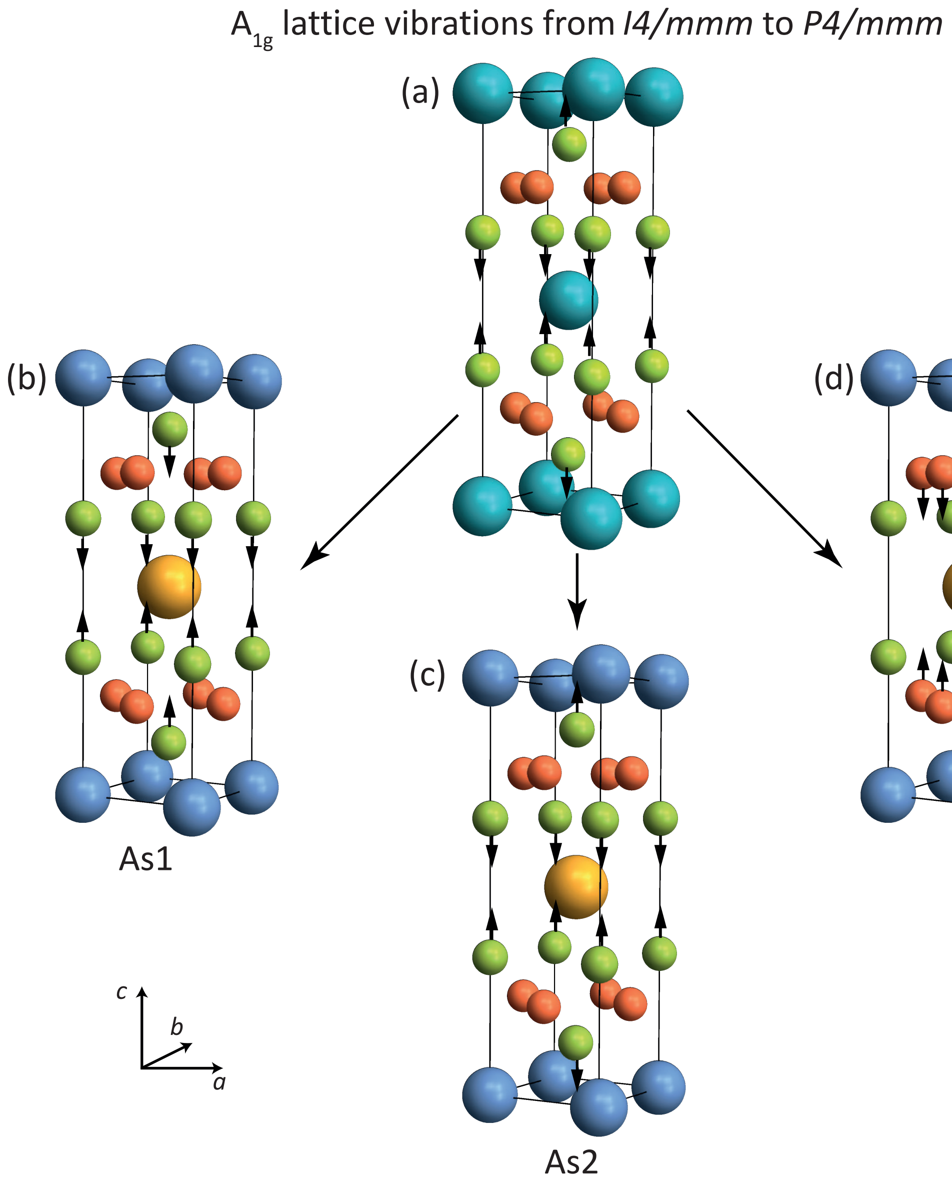

Figure A.2: Raman active $A_{1g}$ modes in $BaFe_2As_2$ and $CaKFe_4As_4$ vibrating along the c-axis. The black arrows indicate the atom displacement. (a) The vibrations of $A_{1g}$ symmetry in $BaFe_2As_2$ split up into (b) in-phase vibrational modes of As(1) and As(2) atoms and (c) out-of-phase As(1) and As(2) vibrations. (d) An additional $A_{1g}$ mode resulting from the Fe displacement.

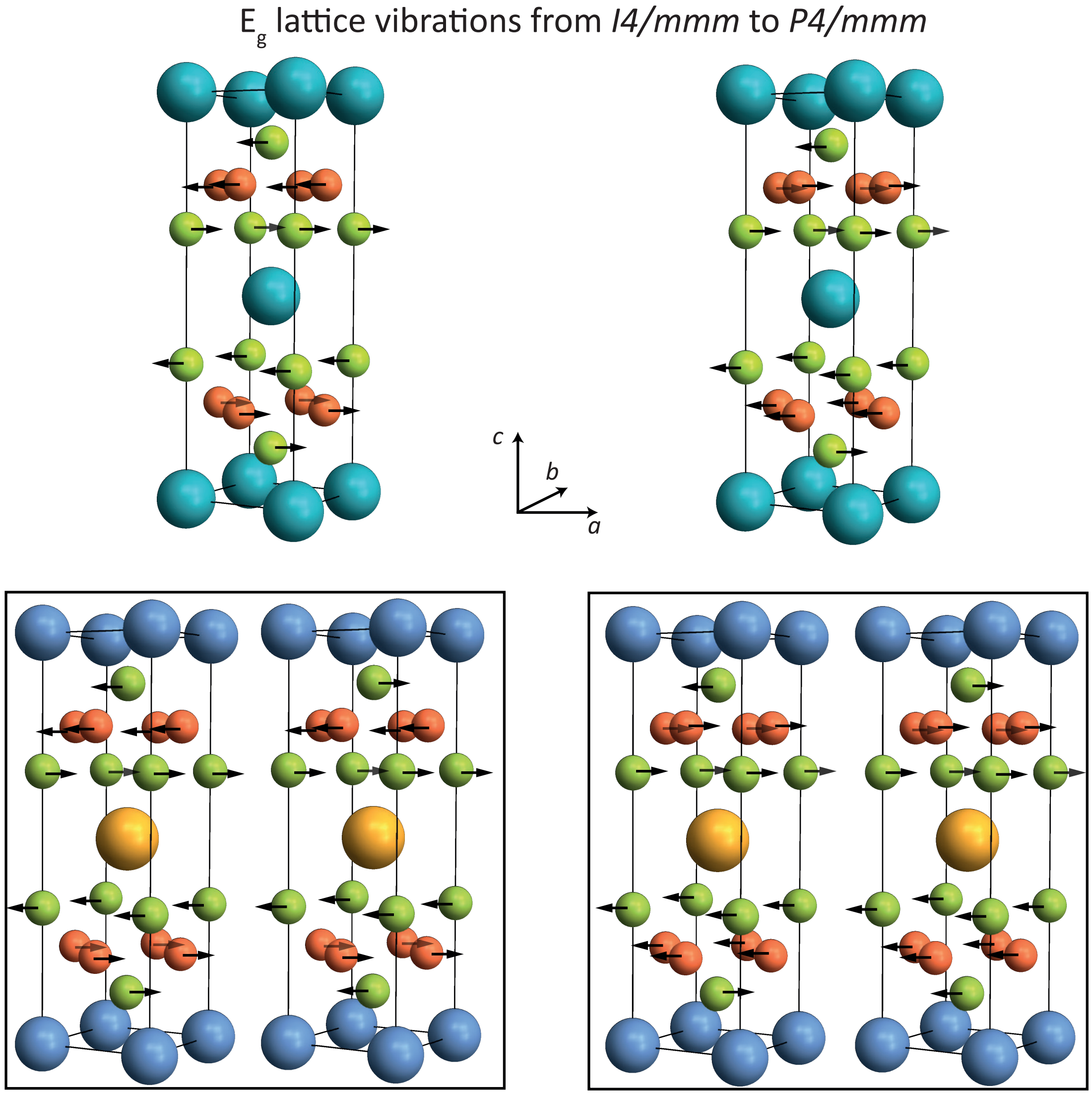

Figure A.3: Raman-active $E_g$ modes in $BaFe_2As_2$ and $CaKFe_4As_4$. Fe and As atoms are displaced as indicated by the black arrows in the $a$-$b$-plane.

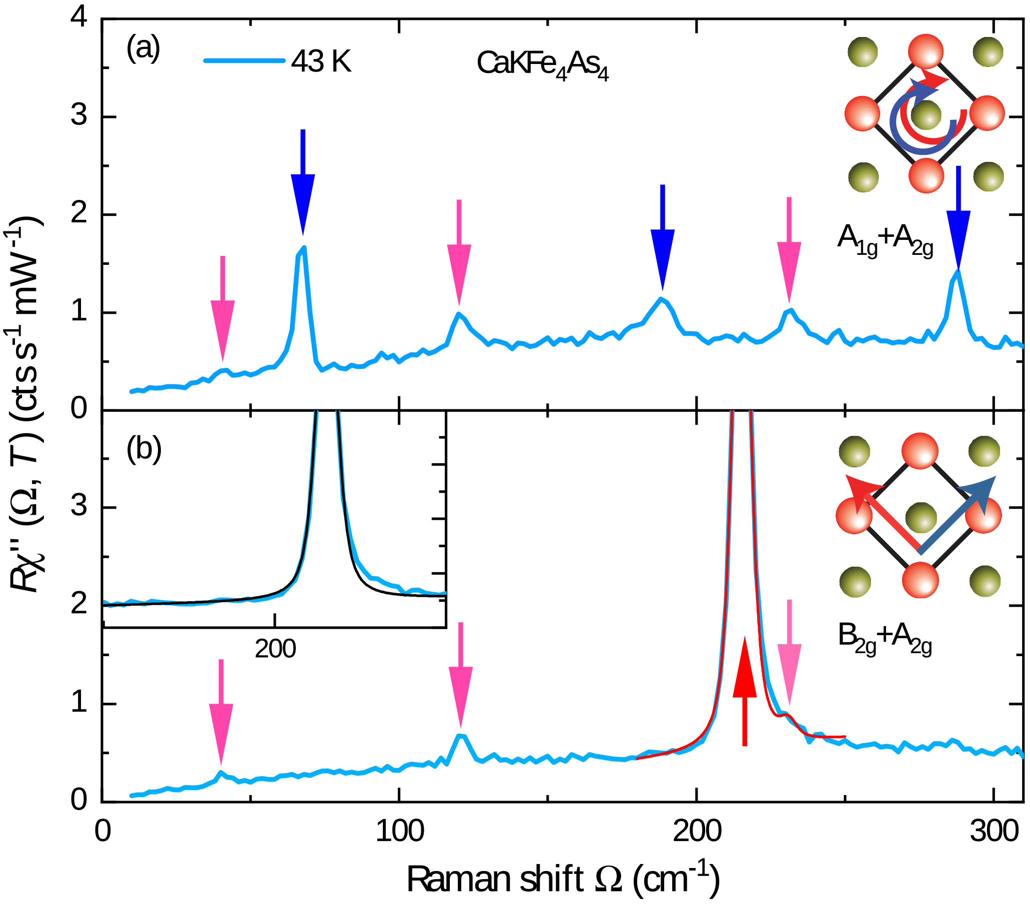

Figure A.4: Raman-active phonons in CaKFe$_4$As$_4$ at 43 K. (a) The blue and magenta arrows indicate the six $RR$ phonon lines in $A_{1g}$ and $E_g$ symmetry, respectively. (b) In $x'y'$ polarisation, the upward red arrow shows the $B_{1g}$ phonon. The red line corresponds to a two-peak Voigt fit. The black curve in the inset is a one-peak Voigt of the $B_{1g}$ phonon line. The crystallographic unit cell is depicted along with the polarisation configurations for $RR$ and $x'y'$ in the upper and lower panel, respectively. Taken from Ref. [45].

## A.2 Raman active modes

The Raman-active phonon lines in CaKFe$_4$As$_4$ are displayed in Fig. A.4, exemplary for 43 K. Their resonance frequencies were extracted with least-square fits and are summarised in Table A.3. In Fig. A.4 (a) six phonon modes can be seen with

*RR* polarisation. Three of these six phonon lines occur only for *RR* polarisation and are therefore ascribed $A_{1g}$ symmetry. The in-phase *c*-axis vibrational modes corresponding to the As(1) and As(2) planes (*cf.* Subsec. A.1) are located at 67.6 $cm^{-1}$ and 187.9 $cm^{-1}$. The third mode is located at 288 $cm^{-1}$ and results from the in-phase vibration of the Fe atoms along the *c*-axis.

Table A.3: Phonon frequencies in $CaKFe_4As_4$ at 43 K as derived from the fit functions.

| pol | unit | $E_g^{(1)}$ | $A_{1g}^{(As(1))}$ | $E_g^{(2)}$ | $A_{1g}^{(As(2))}$ | $B_{1g}^{(Fe)}$ | $E_g^{(3)}$ | $A_{1g}^{(Fe)}$ |
|---|---|---|---|---|---|---|---|---|
| *RR* | $cm^{-1}$ | 40.4 | 67.6 | 120.9 | 187.9 |  | 231.9 | 287.5 |
|  | meV | 5.0 | 8.4 | 15.0 | 23.3 | 26.7 | 28.8 | 35.6 |
| $x'y'$ | $cm^{-1}$ | 40.5 |  | 120.9 |  | 215.2 | 231.1 |  |

For $x'y'$ polarisation (Fig. A.4 (b)) we find the strongest phonon line at 215 $cm^{-1}$. This corresponds to the out-of-phase vibration of the Fe atoms along the *c*-axis. In the crystallographic 2-Fe unit cell this is $B_{1g}$ symmetry. Three modes are visible for both *RR* and $x'y'$ polarisations. As both polarisations yield a finite projection onto the *z*-axis, these lines are assigned $E_g$ symmetry. The $E_g$ phonons result from Fe and As atoms moving parallel to the FeAs planes. The $E_g$ mode at 232 $cm^{-1}$ does not show up as a clear peak in $x'y'$ polarisation due to its proximity to the $B_{1g}$ phonon. However, an analysis with a two-peak Voigt function in Fig. A.4 (b) in red is more convincing than a one-peak Voigt function in the inset (black).

The fourth $E_g$ phonon was not observed, either because of too low intensity or because it occurs at higher energies than the ones observed.

The temperature dependence of the peak energy and the line width were extracted for the *RR* data with the Voigt fit which results from the convolution of a Gaussian with Lorentzian function:

$$y(\Omega) = y_0 + m \cdot \Omega + A \frac{2 \ln 2}{\pi^{3/2}} \frac{\Gamma_L}{\Gamma_G^2} \int_{-\infty}^{\infty} \frac{e^{-t^2}}{\left(\sqrt{\ln 2}\frac{\Gamma_L}{\Gamma_G}\right)^2 + \left(\sqrt{4 \ln 2}\frac{\Omega - \Omega_c}{\Gamma_G} - t\right)^2} \mathrm{d}t \tag{A.1}$$

The electronic background is approximated with the linear term $y_0 + m \cdot \Omega$. $\Gamma_L$ is the width of the Lorentzian and $\Gamma_G$ the width of the Gaussian function. $\Gamma_G$ is determined by the resolution of the spectrometer. For $\lambda_{\text{exc}} = 575$ cm$^{-1}$, this is $\Gamma_G = 4.85$ cm$^{-1}$. The Full-Width-Half-Maximum (FWHM) is defined as

$$FWHM = 0.5346\Gamma_L + \sqrt{0.2166\,\Gamma_L^2 + \Gamma_G^2} \tag{A.2}$$

The $\mathrm{A}_{1g}^{(\mathrm{As}(1))}$ and $\mathrm{A}_{1g}^{(\mathrm{As}(2))}$ modes were better fitted with a convolution of a Gaussian with a Fano function. These are discussed in the next section.

The result for the $\mathrm{E}_{g}^{(1)}$, $\mathrm{E}_{g}^{(2)}$, $\mathrm{E}_{g}^{(3)}$ and $\mathrm{A}_{1g}^{(\mathrm{Fe})}$ modes are depicted in Figs. A.5-A.8. Overall, the peak energy $\Omega_c$ increases upon cooling. The linewidth $\Gamma_L$ decreases for all modes except for the $\mathrm{E}_{g}^{(3)}$ mode. Here, the resolution may have played a role

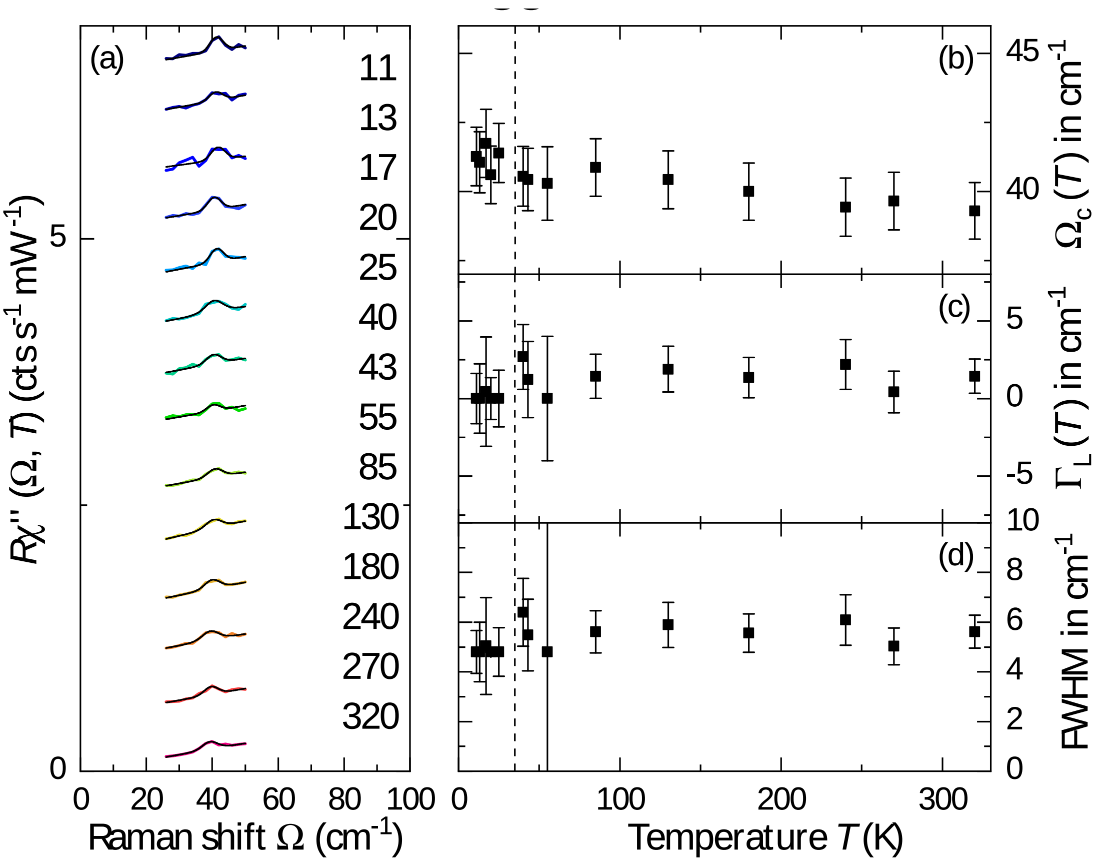

Figure A.5: Analysis of the $E_g^{(1)}$ mode. (a) Spectra in *RR* polarisation for temperatures as indicated. The black lines show the Voigt fit. (b) The resonance frequency $\Omega_c$ as a function of temperature shows the hardening of the lattice as one tunes to lower temperatures. (c) The Lorentzian line-width $\Gamma_L$ decreases for decreasing temperature. The resolution was at the limit of the spectrometer. (d) The Full-Width-Half-Maximum of the Voigt shows, that the width of the spectra is dominated by the resolution of the spectrometer due to the small intrinsic linewidth of the phonon.

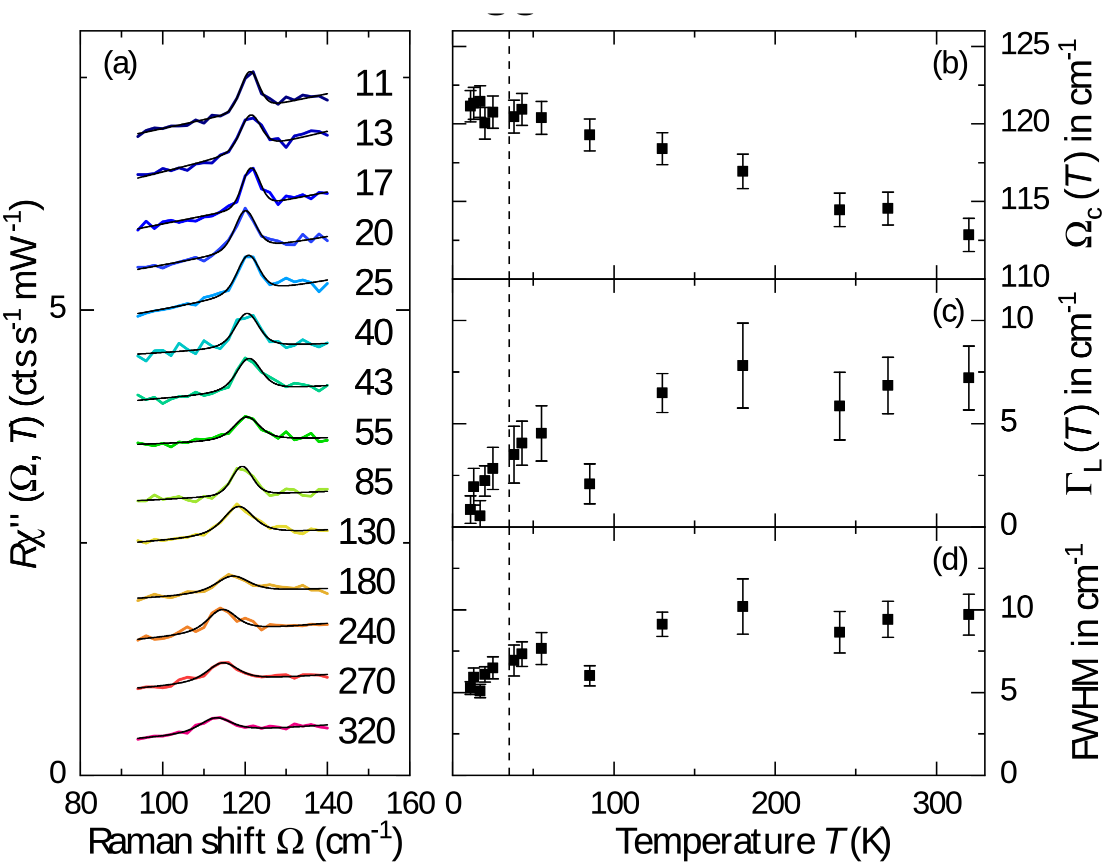

Figure A.6: Analysis of the $E_g^{(2)}$ mode. (a) Spectra in *RR* polarisation for temperatures as indicated. The black lines show the Voigt fit. (b) The resonance frequency as a function of temperature shows the hardening of the lattice as one tunes to lower temperatures. (c) The Lorentzian line-width $\Gamma_L$ decreases for decreasing temperature. (d) The Full-Width-Half-Maximum of the Voigt fit.

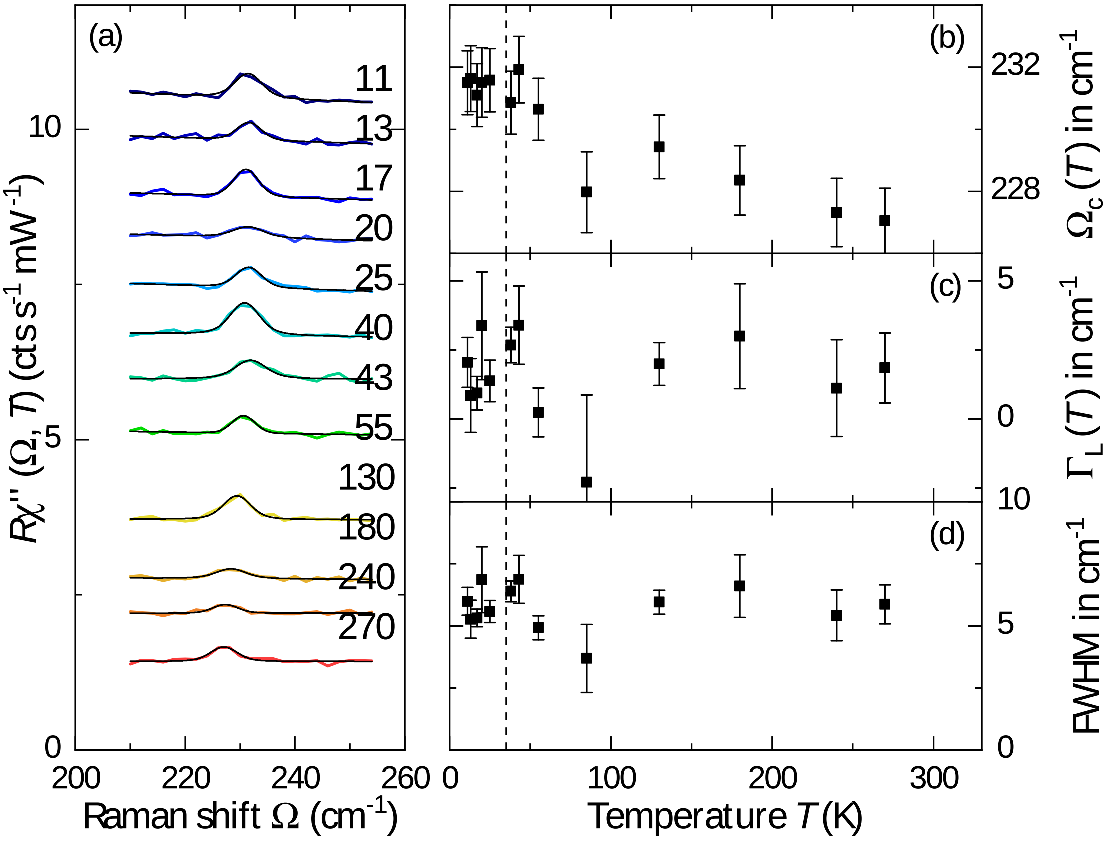

Figure A.7: Analysis of the $E_g^{(3)}$ mode. (a) Spectra in *RR* polarisation for temperatures as indicated. The black lines show the Voigt fit. (b) The resonance frequency as a function of temperature shows the hardening of the lattice as one tunes to lower temperatures. (c) The Lorentzian line-width $\Gamma_L$ decreases for decreasing temperature. (d) The Full-Width-Half-Maximum of the Voigt fit.

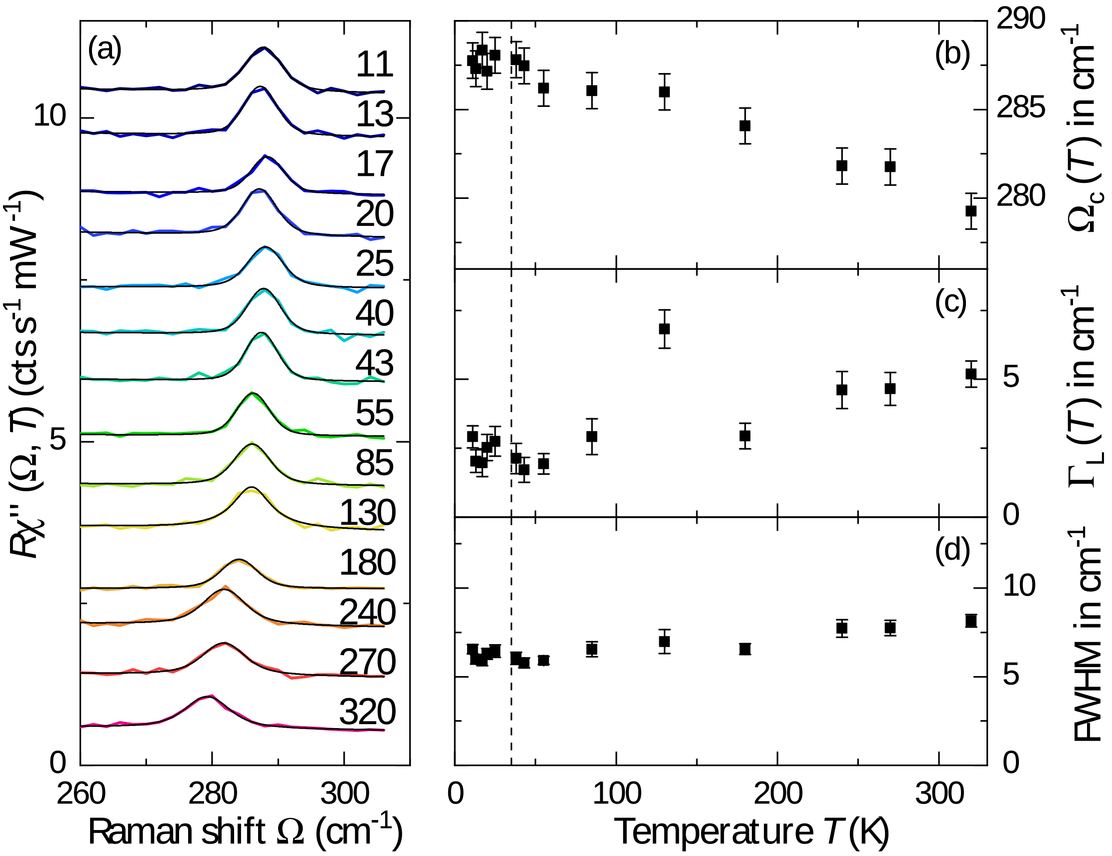

Figure A.8: Analysis of the $A_{1g}^{(Fe)}$ mode. (a) Spectra in *RR* polarisation for temperatures as indicated. The black lines show the Voigt fit. (b) The resonance frequency as a function of temperature shows the hardening of the lattice as one tunes to lower temperatures. (c) The Lorentzian line-width $\Gamma_L$ decreases for decreasing temperature. The resolution was at the limit of the spectrometer. (d) The Full-Width-Half-Maximum of the Voigt.

## A.3 Electron-phonon coupling

Separated from the discussion in chapter 5 is the analysis of the phonon modes and the electron-phonon coupling (EPC) here. This is initially owed to the marginal effect which one expects from the EPC on superconductivity in the pnictides. Nonetheless, as the 1144 compounds, although being very similar to the $BaFe_2As_2$ systems, are relatively new, it is worthwhile to check if the paradigm of a very weak EPC holds for $CaKFe_4As_4$ as well.

### A.3.1 Analysis

The two $A_{1g}$ modes which provide hints for an EPC are the $A_{1g}^{(As(1))}$ and $A_{1g}^{(As(2))}$ mode. The $A_{1g}^{(As(1))}$ mode exhibits an asymmetry for all temperatures (Fig. A.9 (a)). The intrinsic lineshape corresponds to a Fano resonance [148]. In a slighty modified form, this is given by [149]

$$F(\Omega') = \left|\frac{A}{q^2-1}\right| \frac{2}{\Gamma_L \pi} \left[\frac{(q+\Omega')^2}{1+\Omega'^2} - 1\right] \tag{A.3}$$

with the area $A$, the asymmetry parameter $q$, the Lorentzian width $\Gamma_L$ and $\Omega' = 2(\Omega - \Omega_c)/\Gamma_L$, modulo a linear background.

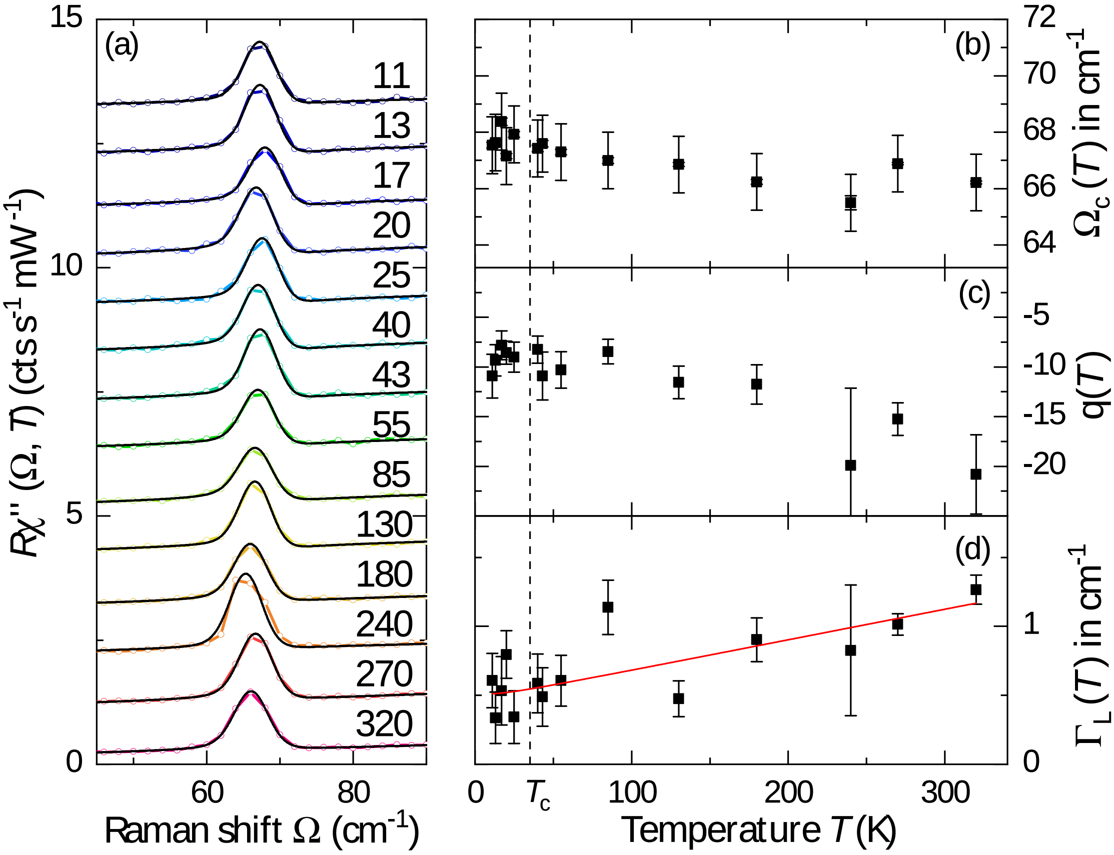

Figure A.9: Analysis of the $A_{1g}^{(As(1))}$ mode. (a) Spectra in *RR* polarisation for temperatures as indicated. The black lines show the fit function in which a Fano is convoluted with a Gaussian. The following values were extracted from the fit function: (b) The resonance frequency as a function of temperature shows the hardening of the lattice as one tunes to lower temperatures. (c) The asymmetry factor $q$ decreases as the temperature decreases. (d) The Lorentzian line-width $\Gamma_L$ decreases for decreasing temperature. The red curve corresponds to the temperature dependence from anharmonic decay.

From the temperature dependence of $\Gamma_L$, one can extract the dimensionless phonon-phonon coupling $\lambda_{\mathrm{ph-ph}}$ via [150,151]:

$$\Gamma(T) = \Gamma_{0,L}\left[1 + \frac{2\lambda_{\mathrm{ph-ph}}}{\exp\left[\frac{\hbar\Omega_0}{2k_{\mathrm{B}}T}\right]}\right] \tag{A.4}$$

Here $\Gamma_{0,L}$ is the zero temperature linewidth and $\Omega_0$ the zero temperature frequency. From Fig. A.9, we estimate $\Gamma_{0,L} = 0.51\,\mathrm{cm}^{-1}$ and $\Omega_0 = 67.9\,\mathrm{cm}^{-1}$. Leaving the phonon-phonon coupling as the only free parameter, the fit of the linewidth delivers $\lambda_{\mathrm{ph-ph}} = 0.11$. The fact that the $\mathrm{A}_{1\mathrm{g}}^{(\mathrm{As}(1))}$ mode exhibits a Fano lineshape is indicative of a coupling to the electronic continuum. Therefore, one may estimate the electron-phonon coupling from the phonon-phonon coupling via $\lambda^2_{\mathrm{el-ph}} \propto \lambda_{\mathrm{ph-ph}}$ [152]. One then finds $\lambda_{\mathrm{el-ph}} \sim 0.32$.

The coupling of the $\mathrm{A}_{1\mathrm{g}}^{(\mathrm{As}(2))}$ mode to the continuum manifests as a Fano lineshape as well. Additionally, this mode does not narrow as temperature decreases, but broadens, specifically for $T < T_c$. We use this to get a figure on the contribution $\lambda_i$ to the total electron-phonon coupling with [153, 154]

$$\lambda_i = \frac{d_i}{\pi\, N(E_F)} \frac{\Delta\Gamma_{0,i}}{\Omega^2_{0,i}} \tag{A.5}$$

where $\Delta\Gamma_{0,i}$ is the linewidth broadening [150, 155, 156] and $N(E_F)$ the density of states at the Fermi energy $E_F$ per spin. $d_i$ is the mode degeneracy. For $\mathrm{A}_{1\mathrm{g}}$ symmetry, this is equal to unity. For a rough estimate of $\Delta\Gamma_L$, the linewidth of the $\mathrm{A}_{1\mathrm{g}}^{(\mathrm{As}(2))}$ mode is compared with the $\mathrm{A}_{1\mathrm{g}}$ mode of undoped $\mathrm{BaFe_2As_2}$. This is done by extracting the phonon-phonon coupling $\lambda_{\mathrm{ph-ph}}$ for the $\mathrm{A}_{1\mathrm{g}}$ phonon of the $\mathrm{BaFe_2As_2}$. This is used to estimate the $\Gamma_{0,L}$ value of the $\mathrm{A}_{1\mathrm{g}}^{(\mathrm{As}(2))}$ mode in $\mathrm{CaKFe_4As_4}$ in the absence of broadening. This value is $\Gamma^{\mathrm{anharm}}_{0,L} = 5.03\,\mathrm{cm}^{-1}$. The extrapolation of the data, on the other hand, gives us $\Gamma^{\mathrm{extra}}_{0,L} = 12.41\,\mathrm{cm}^{-1}$ and the difference therefore is $\Delta\Gamma_0 = 7.4\,\mathrm{cm}^{-1}$. The contribution of the $\mathrm{A}_{1\mathrm{g}}^{(\mathrm{As}(2))}$ mode to the electron-phonon coupling is then $\lambda_i = 0.12$ which gives us a total $\lambda = 0.45$.

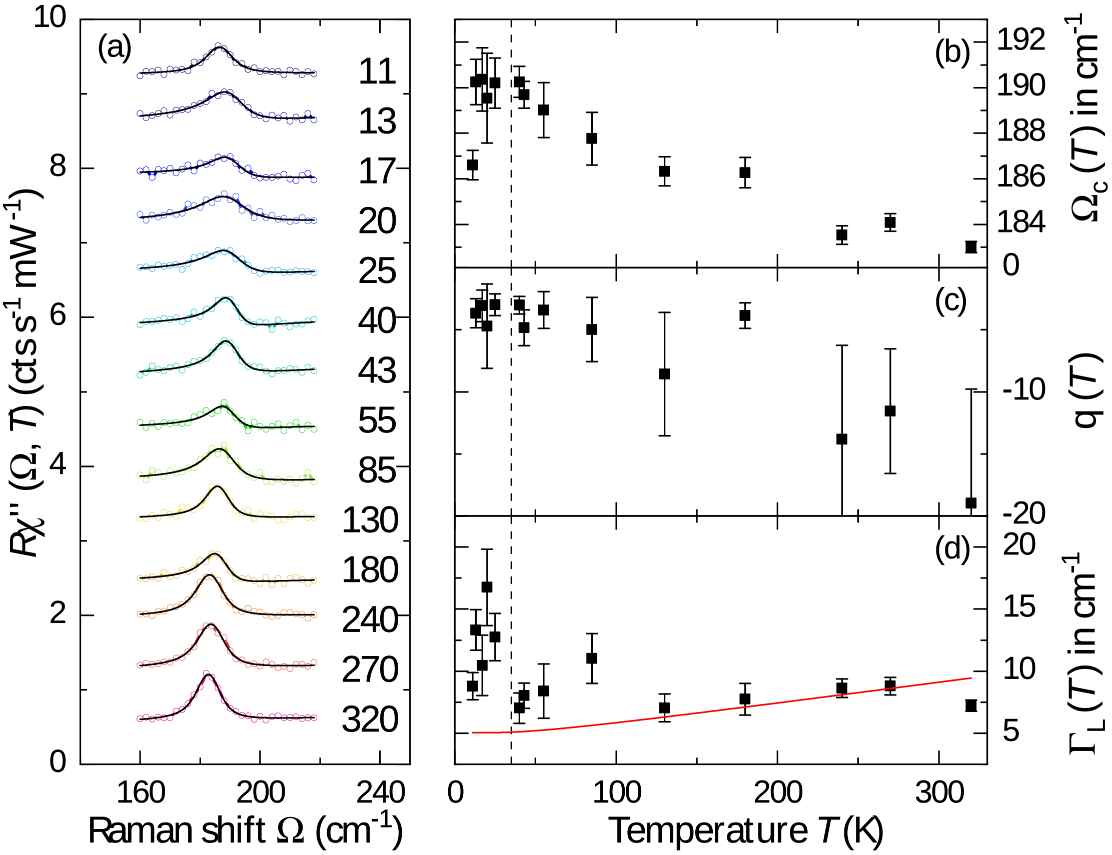

Figure A.10: Analysis of the $A_{1g}^{(As(2))}$ mode. (a) Spectra in *RR* polarisation for temperatures as indicated. The black lines show the fit function in which a Fano is convoluted with a Gaussian. The following values were extracted from the fit function: (b) The resonance frequency as a function of temperature shows the hardening of the lattice as one tunes to lower temperatures. (c) The asymmetry factor $q$ decreases as the temperature decreases. (d) The Lorentzian line-width $\Gamma_L$ stays constant in the range $T > T_c$ and increases for $T < T_c$. The red curve corresponds to the temperature dependence from anharmonic decay in which the phonon-phonon interaction was derived from undoped $BaFe_2As_2$ for comparative reasons and to extract the linewidth broadening.

To estimate $T_c$, we plug this value into the modified McMillan formula [157,158]

$$T_c = \frac{\Omega_{\log}}{1.2\,k_B} \exp\left[-\frac{1.04\,(1+\lambda))}{\lambda - \mu^*\,(1+0.62\lambda)}\right] \tag{A.6}$$

in which $\mu^*$ is the pseudo potential and $\Omega_{\log}$ is the logarithmic average over all phonon frequencies contributing to the electron-phonon coupling. It should be clarified, that Eqn. A.6 is a crude approximation, since the value for the pseudopotential $\mu^*$ is not easy to come by. If the Coulomb repulsion is uniform in the FeSC, the pseudopential ranges from 0.15 to 0.2 [26]. On the other hand, if the unrenormalised Coulomb interaction is different for interband and intraband interactions, it may be reduced and therefore $\mu$ may be reduced [26]. In the absence of additional data on the pseudopotential, $\mu$ was considered to be in the range from 0.1 [153] to 0.2. With the above $\lambda$, the order of the critical temperature from EPC is $T_c \sim 0.05 - 1.3$ K. Even in the extreme case of $\mu^* = 0$, the transition temperature would reach $T_c \sim 4.8\,\mathrm{K}$.

### A.3.2 Conclusion

As expected, the EPC derived from the Raman-active phonons cannot explain the $T_c$ in $CaKFe_4As_4$. However, this does not mean, that the role of phonons in the superconducting pairing can be entirely ruled out. This becomes clear by considering the case of FeSe thin films on $SrTiO_3$ in which $T_c$ is enhanced by at least a factor of 8. Here, the enhancement of $T_c$ in the thin film may be caused due to coupling to the oxygen phonons of the substrate [159].

This mechanism may extend to bulk systems as well. A recent study on the cuprate superconductor Bi-2122 [160] showed an enhancement effect of the electron-electron interaction and the electron-phonon coupling which may increase $T_c$ in these materials. While the analysis above is far from claiming a similar effect in $CaKFe_4As_4$, it may be fruitful to scrutinise the EPC of the Raman-active phonons in future studies. The elusiveness of explanations of high temperature superconductors may result from a too simplified picture which might have to be replaced by a more complex approach of intertwining coupling mechanisms, ranging from EPC to spin fluctuations and quantum critical phenomena.

# Appendix B

# $\mathrm{Ba(Fe_{1-x}Co_x)_2As_2}$

## B.1 Relaxation rates for x = 0.06 and x = 0.085

The dynamic relaxation rates of $\mathrm{Ba(Fe_{0.94}Co_{0.06})_2As_2}$ and $\mathrm{Ba(Fe_{0.915}Co_{0.085})_2As_2}$ are shown in Fig. B.1 and Fig. B.2. From these, the static relaxation rates depicted in 6.5 (b) and (c) were derived. The calculation of the relaxation rates is described in Sec. 6.2.1. The straight lines in the respective figures correspond to the fit of the data with the parallel resistor model of Eqn. 6.5.

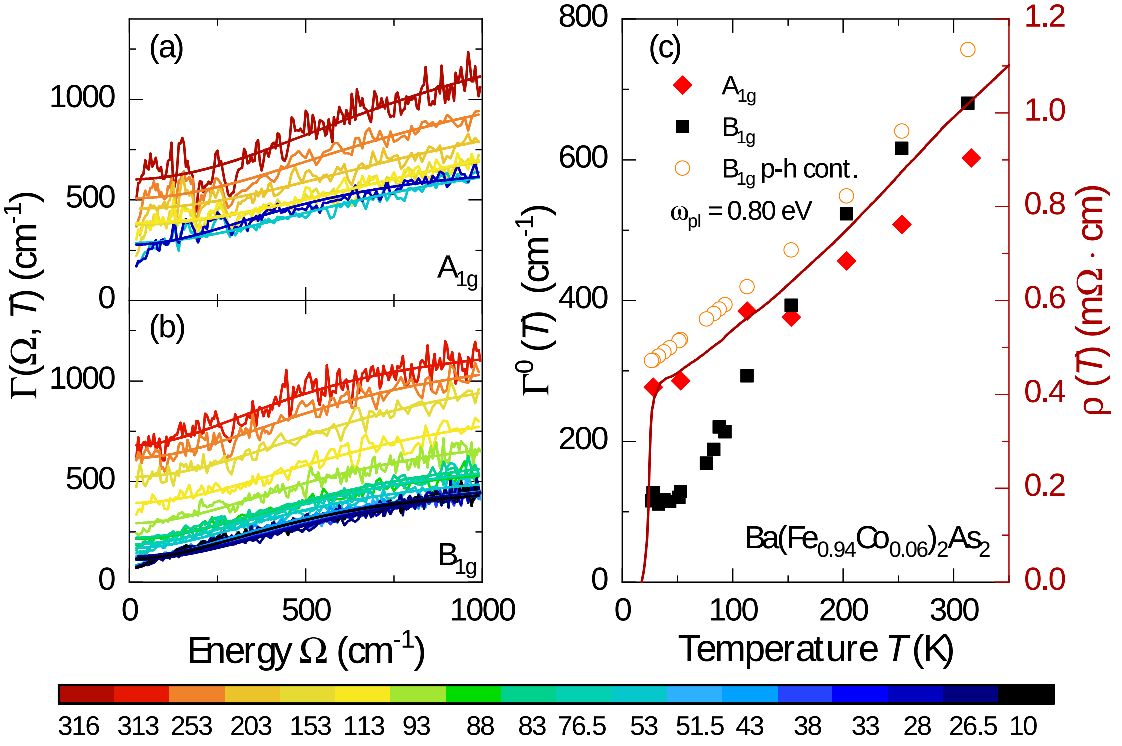

Figure B.1: Relaxation rate analysis of Ba(Fe$_{0.94}$Co$_{0.06}$)$_2$As$_2$. (a) Dynamic relaxation rate of the data in $A_{1g}$ symmetry. (b) Dynamic relaxation rate of the data in $B_{1g}$ symmetry. The straight lines are the fits from the parallel resistor model. (c) The static relaxation rates derived from the PRM as a function of temperature in $B_{1g}$ as black diamonds and $A_{1g}$ with red diamonds along with the resistivity $\rho(T)$ from Ref. [22].

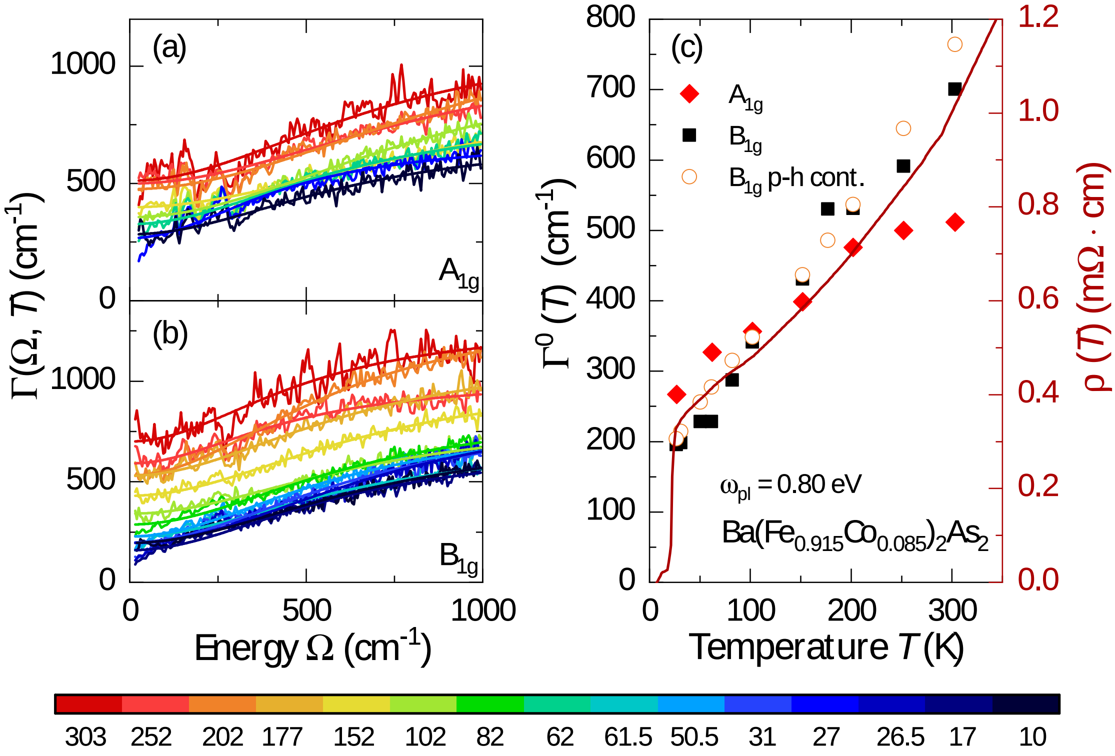

Figure B.2: Relaxation rate analysis of Ba(Fe$_{0.915}$Co$_{0.085}$)$_2$As$_2$. (a) Dynamic relaxation rate of the data in A$_{1g}$ symmetry. (b) Dynamic relaxation rate of the data in B$_{1g}$ symmetry. The straight lines are the fits from the parallel resistor model. (c) The static relaxation rates derived from the PRM as a function of temperature in B$_{1g}$ as black diamonds and A$_{1g}$ with red diamonds along with the resistivity $\rho(T)$ from Ref. [22].

# Bibliography

[1] R. P. Fenyman. *The Pleasureof Finding Things Out*. Perseus books (1999).

[2] Y. Kamihara, H. Hiramatsu, M. Hirano, R. Kawamura, H. Yanagi, T. Kamiya, and H. Hosono. Iron-Based Layered Superconductor: LaOFeP. *Journal of the American Chemical Society* **128**, 10012 (2006).

[3] M. Johannes. Viewpoint: The iron age of superconductivity. `https://physics.aps.org/articles/v1/28#` (2008). Accessed: 2019-10-01.

[4] M. Rotter, M. Tegel, and D. Johrendt. Superconductivity at 38 K in the Iron Arsenide $Ba_{1-x}K_xFe_2As_2$. *Phys. Rev. Lett.* **101**, 107006 (2008).

[5] H. Takahashi, K. Igawa, K. Arii, Y. Kamihara, M. Hirano, and H. Hosono. Superconductivity at 43 K in an iron-based layered compound $LaO_{1-x}F_xFeAs$. *Nature* **453**, 376 (2008).

[6] X. H. Chen, T. Wu, G. Wu, R. H. Liu, H. Chen, and D. F. Fang. Superconductivity at 43 K in $SmFeAsO_{1-x}F_x$. *Nature* **453**, 761 (2008).

[7] F.-C. Hsu, J.-Y. Luo, K.-W. Yeh, T.-K. Chen, T.-W. Huang, P. M. Wu, Y.-C. Lee, Y.-L. Huang, Y.-Y. Chu, D.-C. Yan, and M.-K. Wu. Superconductivity in the PbO-type structure alpha-FeSe. *Proceedings of the National Academy of Sciences of the United States of America* **105**, 14262 (2008).

[8] Y. Kamihara, T. Watanabe, M. Hirano, and H. Hosono. Iron-Based Layered Superconductor $La[O_{1-x}F_x]FeAs$ ($x = 0.05 - 0.12$) with $T_c = 26$ K. *Journal of the American Chemical Society* **130**, 3296 (2008).

[9] Z.-A. Ren, J. Yang, W. Lu, W. Yi, X.-L. Shen, Z.-C. Li, G.-C. Che, X.-L. Dong, L.-L. Sun, F. Zhou, and Z.-X. Zhao. Superconductivity in the iron-based F-doped layered quaternary compound Nd[$O_{1-x}F_x$]FeAs. *EPL (Europhysics Letters)* **82**, 57002 (2008).

[10] J. G. Bednorz and K. A. Müller. Possible highTc superconductivity in the Ba-La-Cu-O system. *Zeitschrift für Physik B Condensed Matter* **64**, 189 (1986).

[11] D. W. Murphy, S. Sunshine, R. B. van Dover, R. J. Cava, B. Batlogg, S. M. Zahurak, and L. F. Schneemeyer. New superconducting cuprate perovskites. *Phys. Rev. Lett.* **58**, 1888 (1987).

[12] P. J. Hirschfeld. Using gap symmetry and structure to reveal the pairing mechanism in Fe-based superconductors. *C. R. Physique* **17**, 197 (2016). Iron-based superconductors / Supraconducteurs à base de fer.

[13] I. I. Mazin, D. J. Singh, M. D. Johannes, and M. H. Du. Unconventional Superconductivity with a Sign Reversal in the Order Parameter of $LaFeAsO_{1-x}F_x$. *Phys. Rev. Lett.* **101**, 057003 (2008).

[14] K. Kuroki, S. Onari, R. Arita, H. Usui, Y. Tanaka, H. Kontani, and H. Aoki. Unconventional Pairing Originating from the Disconnected Fermi Surfaces of Superconducting $LaFeAsO_{1-x}F_x$. *Phys. Rev. Lett.* **101**, 087004 (2008).

[15] A. F. Kemper, T. A. Maier, S. Graser, H.-P. Cheng, P. J. Hirschfeld, and D. J. Scalapino. Sensitivity of the superconducting state and magnetic susceptibility to key aspects of electronic structure in ferropnictides. *New Journal of Physics* **12**, 073030 (2010).

[16] S. Graser, T. A. Maier, P. J. Hirschfeld, and D. J. Scalapino. Near-degeneracy of several pairing channels in multiorbital models for the Fe pnictides. *New Journal of Physics* **11**, 025016 (2009).

[17] S. Maiti, M. M. Korshunov, T. A. Maier, P. J. Hirschfeld, and A. V. Chubukov. Evolution of symmetry and structure of the gap in iron-based superconductors with doping and interactions. *Phys. Rev. B* **84**, 224505 (2011).

[18] S. Maiti, M. M. Korshunov, T. A. Maier, P. J. Hirschfeld, and A. V. Chubukov. Evolution of the Superconducting State of Fe-Based Compounds with Doping. *Phys. Rev. Lett.* **107**, 147002 (2011).

[19] A. E. Böhmer, P. Burger, F. Hardy, T. Wolf, P. Schweiss, R. Fromknecht, M. Reinecker, W. Schranz, and C. Meingast. Nematic Susceptibility of Hole-Doped and Electron-Doped $BaFe_2As_2$ Iron-Based Superconductors from Shear Modulus Measurements. *Phys. Rev. Lett.* **112**, 047001 (2014).

[20] M. Rotter, M. Tegel, D. Johrendt, I. Schellenberg, W. Hermes, and R. Pöttgen. Spin-density-wave anomaly at 140 K in the ternary iron arsenide $BaFe_2As_2$. *Phys. Rev. B* **78**, 020503 (2008).

[21] A. S. Sefat, R. Jin, M. A. McGuire, B. C. Sales, D. J. Singh, and D. Mandrus. Superconductivity at 22 K in Co-Doped $BaFe_2As_2$ Crystals. *Phys. Rev. Lett.* **101**, 117004 (2008).

[22] J.-H. Chu, J. G. Analytis, C. Kucharczyk, and I. R. Fisher. Determination of the phase diagram of the electron-doped superconductor $Ba(Fe_{1-x}Co_x)_2As_2$. *Phys. Rev. B* **79**, 014506 (2009).

[23] T. Böhm. *The case for spin-fluctuation induced pairing in* $Ba_{1-x}K_xFe_2As_2$. Ph.D. thesis, Technical University of Munich (2017). Doktorarbeit, Böhm, Thomas.

[24] T. Böhm, F. Kretzschmar, A. Baum, M. Rehm, D. Jost, R. Hosseinian Ahangharnejhad, R. Thomale, C. Platt, T. A. Maier, W. Hanke, B. Moritz, T. P. Devereaux, D. J. Scalapino, S. Maiti, P. J. Hirschfeld, P. Adelmann, T. Wolf, H.-H. Wen, and R. Hackl. Microscopic origin of Cooper pairing in the iron-based superconductor $Ba_{1-x}K_xFe_2As_2$. *npj Quantum Materials* **3**, 48 (2018).

[25] F. Wang and D.-H. Lee. The Electron-Pairing Mechanism of Iron-Based Superconductors. *Science* **332**, 200 (2011).

[26] P. J. Hirschfeld, M. M. Korshunov, and I. I. Mazin. Gap symmetry and structure of Fe-based superconductors. *Reports on Progress in Physics* **74**, 124508 (2011).

[27] F. Kretzschmar, B. Muschler, T. Böhm, A. Baum, R. Hackl, H.-H. Wen, V. Tsurkan, J. Deisenhofer, and A. Loidl. Raman-Scattering Detection of Nearly Degenerate $s$-Wave and $d$-Wave Pairing Channels in Iron-Based $Ba_{0.6}K_{0.4}Fe_2As_2$ and $Rb_{0.8}Fe_{1.6}As_2$ Superconductors. *Phys. Rev. Lett.* **110**, 187002 (2013).

[28] T. Böhm, A. F. Kemper, B. Moritz, F. Kretzschmar, B. Muschler, H.-M. Eiter, R. Hackl, T. P. Devereaux, D. J. Scalapino, and H.-H. Wen. Balancing Act: Evidence for a Strong Subdominant $d$-Wave Pairing Channel in $Ba_{0.6}K_{0.4}Fe_2As_2$. *Phys. Rev. X* **4**, 041046 (2014).

[29] A. Iyo, K. Kawashima, T. Kinjo, T. Nishio, S. Ishida, H. Fujihisa, Y. Gotoh, K. Kihou, H. Eisaki, and Y. Yoshida. New-Structure-Type Fe-Based Superconductors: $CaAFe_4As_4$ (A = K, Rb, Cs) and $SrAFe_4As_4$ (A = Rb, Cs). *Journal of the American Chemical Society* **138**, 3410 (2016). PMID: 26943024.

[30] D. Mou, T. Kong, W. R. Meier, F. Lochner, L.-L. Wang, Q. Lin, Y. Wu, S. L. Bud'ko, I. Eremin, D. D. Johnson, P. C. Canfield, and A. Kaminski. Enhancement of the Superconducting Gap by Nesting in $CaKFe_4As_4$: A New High Temperature Superconductor. *Phys. Rev. Lett.* **117**, 277001 (2016).

[31] P. K. Biswas, A. Iyo, Y. Yoshida, H. Eisaki, K. Kawashima, and A. D. Hillier. Signature of multigap nodeless superconductivity in $CaKFe_4$ $As_4$. *Phys. Rev. B* **95**, 140505 (2017).

[32] R. Yang, Y. Dai, B. Xu, W. Zhang, Z. Qiu, Q. Sui, C. C. Homes, and X. Qiu. Anomalous phonon behavior in superconducting $CaKFe_4As_4$: An optical study. *Phys. Rev. B* **95**, 064506 (2017).

[33] W. R. Meier, Q.-P. Ding, A. Kreyssig, S. L. Bud'ko, A. Sapkota, K. Kothapalli, V. Borisov, R. Valentí, C. D. Batista, P. P. Orth, R. M. Fernandes, A. I. Goldman, Y. Furukawa, A. E. Böhmer, and P. C. Canfield. Hedgehog

spin-vortex crystal stabilized in a hole-doped iron-based superconductor. *npj Quantum Materials* **3**, 5 (2018).

[34] Q.-P. Ding, W. R. Meier, J. Cui, M. Xu, A. E. Böhmer, S. L. Bud'ko, P. C. Canfield, and Y. Furukawa. Hedgehog Spin-Vortex Crystal Antiferromagnetic Quantum Criticality in CaK$(Fe_{1-x}Ni_x)_4As_4$ Revealed by NMR. *Phys. Rev. Lett.* **121**, 137204 (2018).

[35] Y. Wang, A. Abanov, B. L. Altshuler, E. A. Yuzbashyan, and A. V. Chubukov. Superconductivity near a Quantum-Critical Point: The Special Role of the First Matsubara Frequency. *Phys. Rev. Lett.* **117**, 157001 (2016).

[36] S. Sachdev. *Quantum Phase Transitions*. Cambridge University Press, Cambridge (2000). `https://www.cambridge.org/core/books/quantum-phase-transitions/3EA84C384AC775700DF71BA6FEEF96A4`.

[37] S. Lederer, Y. Schattner, E. Berg, and S. A. Kivelson. Enhancement of Superconductivity near a Nematic Quantum Critical Point. *Phys. Rev. Lett.* **114**, 097001 (2015).

[38] F. Ning, K. Ahilan, T. Imai, A. S. Sefat, R. Jin, M. A. McGuire, B. C. Sales, and D. Mandrus. Spin Susceptibility, Phase Diagram, and Quantum Criticality in the Eelctron-Doped High Tc Superconductor $Ba(Fe_{1-x}Co_x)_2As_2$. *Journal of the Physical Society of Japan* **78**, 013711 (2009).

[39] F. L. Ning, K. Ahilan, T. Imai, A. S. Sefat, M. A. McGuire, B. C. Sales, D. Mandrus, P. Cheng, B. Shen, and H.-H. Wen. Contrasting Spin Dynamics between Underdoped and Overdoped $Ba(Fe_{1-x}Co_x)_2As_2$. *Phys. Rev. Lett.* **104**, 037001 (2010).

[40] C. Bernhard, C. N. Wang, L. Nuccio, L. Schulz, O. Zaharko, J. Larsen, C. Aristizabal, M. Willis, A. J. Drew, G. D. Varma, T. Wolf, and C. Niedermayer. Muon spin rotation study of magnetism and superconductivity in $Ba(Fe_{1-x}Co_x)_2As_2$ single crystals. *Phys. Rev. B* **86**, 184509 (2012).

[41] A. P. Dioguardi, J. Crocker, A. C. Shockley, C. H. Lin, K. R. Shirer, D. M. Nisson, M. M. Lawson, N. apRoberts Warren, P. C. Canfield, S. L. Bud'ko,

S. Ran, and N. J. Curro. Coexistence of Cluster Spin Glass and Superconductivity in Ba(Fe$_{1-x}$Co$_x$)$_2$As$_2$ for 0.060≤$x$≤0.071. *Phys. Rev. Lett.* **111**, 207201 (2013).

[42] D. J. Scalapino and T. P. Devereaux. Collective $d$-wave exciton modes in the calculated Raman spectrum of Fe-based superconductors. *Phys. Rev. B* **80**, 140512 (2009).

[43] S. Caprara, C. Di Castro, M. , and D. Suppa. Charge-Fluctuation Contribution to the Raman Response in Superconducting Cuprates. *Phys. Rev. Lett.* **95**, 117004 (2005).

[44] F. Kretzschmar, T. Böhm, U. Karahasanović, B. Muschler, A. Baum, D. Jost, J. Schmalian, S. Caprara, M. Grilli, C. Di Castro, J. H. Analytis, J.-H. Chu, I. R. Fisher, and R. Hackl. Critical spin fluctuations and the origin of nematic order in Ba(Fe$_{1-x}$Co$_x$)$_2$As$_2$. *Nature Phys.* **12**, 560 (2016).

[45] D. Jost, J.-R. Scholz, U. Zweck, W. R. Meier, A. E. Böhmer, P. C. Canfield, N. Lazarević, and R. Hackl. Indication of subdominant d-wave interaction in superconducting CaKFe$_4$As$_4$. *Phys. Rev. B* **98**, 020504 (2018).

[46] J. C. Slater. Atomic Radii in Crystals. *The Journal of Chemical Physics* **41**, 3199 (1964).

[47] J.-R. Scholz. *Raman scattering study of the superconducting pairing in CaKFe$_4$As$_4$*. Master's thesis, Technical University of Munich (2017). Masterarbeit, Scholz, Jan-Robin.

[48] I. R. Shein and A. L. Ivanovskii. Electronic structure of new oxygen-free 38-K superconductor Ba$_{1-x}$K$_x$Fe$_2$As$_2$ in comparison with BaFe$_2$As$_2$ from the first principles. *JETP Letters* **88**, 107 (2008).

[49] J. Paglione and R. L. Greene. High-temperature superconductivity in iron-based materials. *Nature Physics* **6**, 645 EP (2010). Review Article.

[50] D. V. Evtushinsky, D. S. Inosov, V. B. Zabolotnyy, A. Koitzsch, M. Knupfer, B. Büchner, M. S. Viazovska, G. L. Sun, V. Hinkov, A. V. Boris, C. T. Lin,

B. Keimer, A. Varykhalov, A. A. Kordyuk, and S. V. Borisenko. Momentum dependence of the superconducting gap in $Ba_{1-x}K_xFe_2As_2$. *Phys. Rev. B* **79**, 054517 (2009).

[51] J. Fink, S. Thirupathaiah, R. Ovsyannikov, H. A. Dürr, R. Follath, Y. Huang, S. de Jong, M. S. Golden, Y.-Z. Zhang, H. O. Jeschke, R. Valentí, C. Felser, S. Dastjani Farahani, M. Rotter, and D. Johrendt. Electronic structure studies of $BaFe_2As_2$ by angle-resolved photoemission spectroscopy. *Phys. Rev. B* **79**, 155118 (2009).

[52] Y. Yin, M. Zech, T. L. Williams, X. F. Wang, G. Wu, X. H. Chen, and J. E. Hoffman. Scanning Tunneling Spectroscopy and Vortex Imaging in the Iron Pnictide Superconductor $BaFe_{1.8}Co_{0.2}As_2$. *Phys. Rev. Lett.* **102**, 097002 (2009).

[53] S. Graser, A. F. Kemper, T. A. Maier, H.-P. Cheng, P. J. Hirschfeld, and D. J. Scalapino. Spin fluctuations and superconductivity in a three-dimensional tight-binding model for $BaFe_2As_2$. *Phys. Rev. B* **81**, 214503 (2010).

[54] F. Lochner, F. Ahn, T. Hickel, and I. Eremin. Electronic properties, low-energy Hamiltonian, and superconducting instabilities in $CaKFe_4As_4$. *Phys. Rev. B* **96**, 094521 (2017).

[55] K. Terashima, Y. Sekiba, J. H. Bowen, K. Nakayama, T. Kawahara, T. Sato, P. Richard, Y.-M. Xu, L. J. Li, G. H. Cao, Z.-A. Xu, H. Ding, and T. Takahashi. Fermi surface nesting induced strong pairing in iron-based superconductors. *Proceedings of the National Academy of Sciences* **106**, 7330 (2009).

[56] T. Sudayama, Y. Wakisaka, K. Takubo, R. Morinaga, T. J. Sato, M. Arita, H. Namatame, M. Taniguchi, and T. Mizokawa. Band Structure of the Heavily-Electron-Doped FeAs-Based $Ba(Fe,Co)_2As_2$ Superconductor Suppresses Antiferromagnetic Correlations. *Phys. Rev. Lett.* **104**, 177002 (2010).

[57] Y. Zhang, F. Chen, C. He, B. Zhou, B. P. Xie, C. Fang, W. F. Tsai, X. H. Chen, H. Hayashi, J. Jiang, H. Iwasawa, K. Shimada, H. Namatame, M. Taniguchi, J. P. Hu, and D. L. Feng. Orbital characters of bands in the iron-based superconductor $BaFe_{1.85}Co_{0.15}As_2$. *Phys. Rev. B* **83**, 054510 (2011).

[58] W. R. Meier, T. Kong, U. S. Kaluarachchi, V. Taufour, N. H. Jo, G. Drachuck, A. E. Böhmer, S. M. Saunders, A. Sapkota, A. Kreyssig, M. A. Tanatar, R. Prozorov, A. I. Goldman, F. F. Balakirev, A. Gurevich, S. L. Bud'ko, and P. C. Canfield. Anisotropic thermodynamic and transport properties of single-crystalline $CaKFe_4As_4$. *Phys. Rev. B* **94**, 064501 (2016).

[59] S. Avci, O. Chmaissem, D. Y. Chung, S. Rosenkranz, E. A. Goremychkin, J. P. Castellan, I. S. Todorov, J. A. Schlueter, H. Claus, A. Daoud-Aladine, D. D. Khalyavin, M. G. Kanatzidis, and R. Osborn. Phase diagram of $Ba_{1-x}K_xFe_2As_2$. *Phys. Rev. B* **85**, 184507 (2012).

[60] M. G. Kim, R. M. Fernandes, A. Kreyssig, J. W. Kim, A. Thaler, S. L. Bud'ko, P. C. Canfield, R. J. McQueeney, J. Schmalian, and A. I. Goldman. Character of the structural and magnetic phase transitions in the parent and electron-doped $BaFe_2As_2$ compounds. *Phys. Rev. B* **83**, 134522 (2011).

[61] C. R. Rotundu and R. J. Birgeneau. First- and second-order magnetic and structural transitions in $bafe_{2(1-x)}co_{2x}as_2$. *Phys. Rev. B* **84**, 092501 (2011).

[62] T. Böhm, R. H. Ahangharnejhad, D. Jost, A. Baum, B. Muschler, F. Kretzschmar, P. Adelmann, T. Wolf, H.-H. Wen, J.-H. Chu, I. R. Fisher, and R. Hackl. Superconductivity and fluctuations in $Ba_{1-p}K_pFe_2As_2$ and $Ba(Fe_{1-n}Co_n)_2As_2$. *phys. status solidi (b)* **254**, 1600308 (2017).

[63] R. M. Fernandes, A. V. Chubukov, and J. Schmalian. What drives nematic order in iron-based superconductors? *Nature Physics* **10**, 97 EP (2014). Review Article.

[64] H. Kontani, T. Saito, and S. Onari. Origin of orthorhombic transition, magnetic transition, and shear-modulus softening in iron pnictide superconductors: Analysis based on the orbital fluctuations theory. *Phys. Rev. B* **84**, 024528 (2011).

[65] S.-H. Baek, D. V. Efremov, J. M. Ok, J. S. Kim, J. van den Brink, and B. Büchner. Orbital-driven nematicity in FeSe. *Nature Materials* **14**, 210 EP (2014). Article.

[66] H. Kontani and Y. Yamakawa. Linear Response Theory for Shear Modulus $C_{66}$ and Raman Quadrupole Susceptibility: Evidence for Nematic Orbital Fluctuations in Fe-based Superconductors. *Phys. Rev. Lett.* **113**, 047001 (2014).

[67] Y. Gallais, R. M. Fernandes, I. Paul, L. Chauvière, Y.-X. Yang, M.-A. Méasson, M. Cazayous, A. Sacuto, D. Colson, and A. Forget. Observation of Incipient Charge Nematicity in $Ba(Fe_{1-x}Co_x)_2As_2$. *Phys. Rev. Lett.* **111**, 267001 (2013).

[68] V. K. Thorsmølle, M. Khodas, Z. P. Yin, C. Zhang, S. V. Carr, P. Dai, and G. Blumberg. Critical quadrupole fluctuations and collective modes in iron pnictide superconductors. *Phys. Rev. B* **93**, 054515 (2016).

[69] Z.-X. Shen, D. S. Dessau, B. O. Wells, D. M. King, W. E. Spicer, A. J. Arko, D. Marshall, L. W. Lombardo, A. Kapitulnik, P. Dickinson, S. Doniach, J. DiCarlo, T. Loeser, and C. H. Park. Anomalously large gap anisotropy in the a-b plane of $Bi_2Sr_2CaCu_2O_{8+\delta}$. *Phys. Rev. Lett.* **70**, 1553 (1993).

[70] A. Damascelli, Z. Hussain, and Z.-X. Shen. Angle-resolved photoemission studies of the cuprate superconductors. *Rev. Mod. Phys.* **75**, 473 (2003).

[71] A. Chubukov. Pairing Mechanism in Fe-Based Superconductors. *Annual Review of Condensed Matter Physics* **3**, 57 (2012).

[72] K. Nakayama, T. Sato, P. Richard, Y.-M. Xu, Y. Sekiba, S. Souma, G. F. Chen, J. L. Luo, N. L. Wang, H. Ding, and T. Takahashi. Superconducting gap symmetry of $Ba_{0.6}K_{0.4}Fe_2As_2$ studied by angle-resolved photoemission spectroscopy. *EPL (Europhysics Letters)* **85**, 67002 (2009).

[73] M. Yoshizawa, D. Kimura, T. Chiba, S. Simayi, Y. Nakanishi, K. Kihou, C.-H. Lee, A. Iyo, H. Eisaki, M. Nakajima, and S.-i. Uchida. Structural Quantum Criticality and Superconductivity in Iron-Based Superconductor $Ba(Fe_{1-x}Co_x)_2As_2$. *Journal of the Physical Society of Japan* **81**, 024604 (2012).

[74] H.-H. Kuo, J.-H. Chu, J. C. Palmstrom, S. A. Kivelson, and I. R. Fisher. Ubiquitous signatures of nematic quantum criticality in optimally doped Fe-based superconductors. *Science* **352**, 958 (2016).

[75] N. F. Berk and J. R. Schrieffer. Effect of Ferromagnetic Spin Correlations on Superconductivity. *Phys. Rev. Lett.* **17**, 433 (1966).

[76] D. Fay and J. Appel. Coexistence of $p$-state superconductivity and itinerant ferromagnetism. *Phys. Rev. B* **22**, 3173 (1980).

[77] P. Monthoux and D. Pines. Spin-fluctuation-induced superconductivity and normal-state properties of $YBa_2Cu_3O_7$. *Phys. Rev. B* **49**, 4261 (1994).

[78] A. Abanov, A. V. Chubukov, and J. Schmalian. Quantum-critical theory of the spin-fermion model and its application to cuprates: Normal state analysis. *Advances in Physics* **52**, 119 (2003).

[79] P. Monthoux, D. Pines, and G. G. Lonzarich. Superconductivity without phonons. *Nature* **450**, 1177 EP (2007). Review Article.

[80] S. Sachdev. Where is the quantum critical point in the cuprate superconductors? *physica status solidi (b)* **247**, 537 (2010).

[81] N. D. Mathur, F. M. Grosche, S. R. Julian, I. R. Walker, D. M. Freye, R. K. W. Haselwimmer, and G. G. Lonzarich. Magnetically mediated superconductivity in heavy fermion compounds. *Nature* **394**, 39 (1998).

[82] R. Zhou, Z. Li, J. Yang, D. L. Sun, C. T. Lin, and G.-q. Zheng. Quantum criticality in electron-doped $BaFe_{2-x}Ni_xAs_2$. *Nature Communications* **4**, 2265 EP (2013). Article.

[83] I. M. Hayes, R. D. McDonald, N. P. Breznay, T. Helm, P. J. W. Moll, M. Wartenbe, A. Shekhter, and J. G. Analytis. Scaling between magnetic field and temperature in the high-temperature superconductor $BaFe_2(As_{1-x}P_x)_2$. *Nature Physics* **12**, 916 EP (2016).

[84] S. Raghu, G. Torroba, and H. Wang. Metallic quantum critical points with finite BCS couplings. *Phys. Rev. B* **92**, 205104 (2015).

[85] M. A. Metlitski, D. F. Mross, S. Sachdev, and T. Senthil. Cooper pairing in non-fermi liquids. *Phys. Rev. B* **91**, 115111 (2015).

[86] A. V. Chubukov. Andrey Chubukov - Superconductivity near a quantum critical point - boson-fermion models. `https://www.youtube.com/watch?v=ViiLneolDfo` (2017).

[87] F. J. Dyson. The *S* Matrix in Quantum Electrodynamics. *Phys. Rev.* **75**, 1736 (1949).

[88] J. Schwinger. On the Green's Functions of Quantized Fields. I. *Proceedings of the National Academy of Science* **37**, 452 (1951).

[89] J.-H. She, B. J. Overbosch, Y.-W. Sun, Y. Liu, K. E. Schalm, J. A. Mydosh, and J. Zaanen. Observing the origin of superconductivity in quantum critical metals. *Phys. Rev. B* **84**, 144527 (2011).

[90] A. Smekal. Zur Quantentheorie der Dispersion. *Naturwissenschaften* **11**, 873 (1923).

[91] H. A. Kramers and W. Heisenberg. Über die Streuung von Strahlung durch Atome. *Zeitschrift für Physik* **31**, 681 (1925).

[92] C. V. RAMAN and K. S. KRISHNAN. The Negative Absorption of Radiation. *Nature* **122**, 12 (1928).

[93] G. S. Landsberg and L. I. Mandelstam. Eine neue Erscheinung bei der Lichtzerstreuung in Krystallen. *Naturwissenschaften* **16**, 557 (1928).

[94] T. P. Devereaux and R. Hackl. Inelastic light scattering from correlated electrons. *Rev. Mod. Phys.* **79**, 175 (2007).

[95] W. M. Tolles, J. W. Nibler, J. R. McDonald, and A. B. Harvey. A Review of the Theory and Application of Coherent Anti-Stokes Raman Spectroscopy (CARS). *Applied Spectroscopy* **31**, 253 (1977).

[96] A. M. Zheltikov. Coherent anti-Stokes Raman scattering: from proof-of-the-principle experiments to femtosecond CARS and higher order wave-mixing generalizations. *Journal of Raman Spectroscopy* **31**, 653 (2000).

[97] F. Kretzschmar. *Nematic Fluctuations, Fermiology and the Pair Breaking Potential in Iron-Based Superconductors*. Dissertation, Technische Universität München (2015).

[98] D. Pines and P. Nozières. *The Theory of Quantum Liquids*. Number Bd. 1 in The Theory of Quantum Liquids. W.A. Benjamin (1966). `https://books.google.at/books?id=dcIRAQAAIAAJ`.

[99] F. A. Blum. Inelastic light scattering from semiconductor plasmas in a magnetic field. *Phys. Rev. B* **1**, 1125 (1970).

[100] T. P. Devereaux, A. Virosztek, and A. Zawadowski. Multiband electronic Raman scattering in bilayer superconductors. *Phys. Rev. B* **54**, 12523 (1996).

[101] R. Kubo. The fluctuation-dissipation theorem. *Reports on Progress in Physics* **29**, 255 (1966).

[102] P. B. Allen. Fermi-surface harmonics: A general method for nonspherical problems. Application to Boltzmann and Eliashberg equations. *Phys. Rev. B* **13**, 1416 (1976).

[103] M. V. Klein and S. B. Dierker. Theory of raman scattering in superconductors. *Phys. Rev. B* **29**, 4976 (1984).

[104] H. Monien and A. Zawadowski. Theory of Raman scattering with final-state interaction in high-$T_c$ BCS superconductors: Collective modes. *Phys. Rev. B* **41**, 8798 (1990).

[105] B. S. Shastry and B. I. Shraiman. Raman Scattering in Mott-Hubbard Systems. *International Journal of Modern Physics B* **05**, 365 (1991).

[106] T. P. Devereaux. Theory for the effects of impurities on the Raman spectra of superconductors. *Phys. Rev. B* **45**, 12965 (1992).

[107] A. Baum. *Interrelation of lattice, charge, and spin degrees of freedom in iron based systems*. Ph.D. thesis, Technical University of Munich, The address of the publisher (2018). Doktorarbeit, Baum, Andreas Christoph.

[108] I. I. Mazin, T. P. Devereaux, J. G. Analytis, J.-H. Chu, I. R. Fisher, B. Muschler, and R. Hackl. Pinpointing gap minima in $Ba(Fe_{0.94}Co_{0.06})_2As_2$ via band-structure calculations and electronic Raman scattering. *Phys. Rev. B* **82**, 180502 (2010).

[109] T. P. Devereaux. Theory for the effects of impurities on the raman spectra of superconductors. ii. temperature dependence and influence of final-state interactions. *Phys. Rev. B* **47**, 5230 (1993).

[110] T. P. Devereaux and D. Einzel. Electronic Raman scattering in superconductors as a probe of anisotropic electron pairing. *Phys. Rev. B* **51**, 16336 (1995).

[111] T. P. Devereaux, D. Einzel, B. Stadlober, R. Hackl, D. H. Leach, and J. J. Neumeier. Electronic Raman scattering in high-$T_c$ superconductors: A probe of $d_{x^2-y^2}$ pairing. *Phys. Rev. Lett.* **72**, 396 (1994).

[112] D. Branch and J. P. Carbotte. Raman electronic continuum in a spin-fluctuation model for superconductivity. *Phys. Rev. B* **52**, 603 (1995).

[113] G. R. Boyd, T. P. Devereaux, P. J. Hirschfeld, V. Mishra, and D. J. Scalapino. Probing the pairing symmetry of the iron pnictides with electronic Raman scattering. *Phys. Rev. B* **79**, 174521 (2009).

[114] A. Bardasis and J. R. Schrieffer. Excitons and Plasmons in Superconductors. *Phys. Rev.* **121**, 1050 (1961).

[115] A. V. Chubukov, I. Eremin, and M. M. Korshunov. Theory of raman response of a superconductor with extended $s$-wave symmetry: Application to the iron pnictides. *Phys. Rev. B* **79**, 220501 (2009).

[116] L. Aslamasov and A. Larkin. The influence of fluctuation pairing of electrons on the conductivity of normal metal. *Physics Letters A* **26**, 238 (1968).

[117] S. Takada and E. Sakai. Fluctuation Conductivity in One-Dimensional Incommensurate Peierls System. *Progress of Theoretical Physics* **59**, 1802 (1978).

[118] M. Grilli, S. Caprara, C. D. Castro, T. Enss, R. Hackl, B. Muschler, and W. Prestel. Spectral signatures of critical charge and spin fluctuations in cuprates. *Physica B: Condensed Matter* **404**, 3070 (2009).

[119] S. Onari and H. Kontani. Self-consistent Vertex Correction Analysis for Iron-based Superconductors: Mechanism of Coulomb Interaction-Driven Orbital Fluctuations. *Phys. Rev. Lett.* **109**, 137001 (2012).

[120] M. Khodas, A. V. Chubukov, and G. Blumberg. Collective modes in multiband superconductors: Raman scattering in iron selenides. *Phys. Rev. B* **89**, 245134 (2014).

[121] Y. Gallais and I. Paul. Charge nematicity and electronic Raman scattering in iron-based superconductors. *Comptes Rendus Physique* **17**, 113 (2016). Iron-based superconductors / Supraconducteurs à base de fer.

[122] A. Hinojosa, J. Cai, and A. V. Chubukov. Raman resonance in iron-based superconductors: The magnetic scenario. *Phys. Rev. B* **93**, 075106 (2016).

[123] U. Karahasanovic, F. Kretzschmar, T. Böhm, R. Hackl, I. Paul, Y. Gallais, and J. Schmalian. Manifestation of nematic degrees of freedom in the raman response function of iron pnictides. *Phys. Rev. B* **92**, 075134 (2015).

[124] W. Prestel. *Study of the Interaction Processes in Cuprate Superconductors by a Quantitative Comparison of Spectroscopic Experiments*. Dissertation, Technische Universität München (2012).

[125] W. R. Meier, T. Kong, S. L. Bud'ko, and P. C. Canfield. Optimization of the crystal growth of the superconductor $CaKFe_4As_4$ from solution in the FeAs-$CaFe_2As_2$-$KFe_2As_2$ system. *Phys. Rev. Materials* **1**, 013401 (2017).

[126] F. Hardy, P. Adelmann, T. Wolf, H. v. Löhneysen, and C. Meingast. Large Anisotropic Uniaxial Pressure Dependencies of $T_c$ in Single Crystalline $Ba(Fe_{0.92}Co_{0.08})_2As_2$. *Phys. Rev. Lett.* **102**, 187004 (2009).

[127] F. Hardy, T. Wolf, R. A. Fisher, R. Eder, P. Schweiss, P. Adelmann, H. v. Löhneysen, and C. Meingast. Calorimetric evidence of multiband supercon-

ductivity in Ba(Fe$_{0.925}$Co$_{0.075}$)$_2$As$_2$ single crystals. *Phys. Rev. B* **81**, 060501 (2010).

[128] F. Venturini. *Raman Scattering Study of Electronic Correlations in Cuprates: Observation of an Unconventional Metal-Insulator Transition*. Ph.D. thesis, Technical University of Munich, The address of the publisher (2003). Doktorarbeit, Venturini, Francesca.

[129] A. Abrikosov. The magnetic properties of superconducting alloys. *Journal of Physics and Chemistry of Solids* **2**, 199 (1957).

[130] C. P. Bean. Magnetization of Hard Superconductors. *Phys. Rev. Lett.* **8**, 250 (1962).

[131] C. P. Bean. Magnetization of High-Field Superconductors. *Rev. Mod. Phys.* **36**, 31 (1964).

[132] D. Jost. *Spin fluctuations and superconductivitiy in Fe-based compounds*. Master's thesis, Technical University of Munich (Master's thesis, Technische Universität München, 2016).

[133] S. A. Kivelson and D. S. Rokhsar. Bogoliubov quasiparticles, spinons, and spin-charge decoupling in superconductors. *Phys. Rev. B* **41**, 11693 (1990).

[134] S. Lederer, D. Jost, T. Böhm, R. Hackl, E. Berg, and S. Kivelson. Measuring the imaginary time dynamics of quantum materials. *arXiv e-prints* arXiv:1907.10182 (2019).

[135] A. Baum, Y. Li, M. Tomić, N. Lazarević, D. Jost, F. Löffler, B. Muschler, T. Böhm, J.-H. Chu, I. R. Fisher, R. Valentí, I. I. Mazin, and R. Hackl. Interplay of lattice, electronic, and spin degrees of freedom in detwinned BaFe$_2$As$_2$: A Raman scattering study. *Phys. Rev. B* **98**, 075113 (2018).

[136] M. Opel, R. Nemetschek, C. Hoffmann, R. Philipp, P. F. Müller, R. Hackl, I. Tüttő, A. Erb, B. Revaz, E. Walker, H. Berger, and L. Forró. Carrier relaxation, pseudogap, and superconducting gap in high-T$_c$ cuprates: A Raman scattering study. *Phys. Rev. B* **61**, 9752 (2000).

[137] N. E. Hussey, J. C. Alexander, and R. A. Cooper. Optical response of high-$T_c$ cuprates: Possible role of scattering rate saturation and in-plane anisotropy. *Phys. Rev. B* **74**, 214508 (2006).

[138] H. Wiesmann, M. Gurvitch, H. Lutz, A. Ghosh, B. Schwarz, M. Strongin, P. B. Allen, and J. W. Halley. Simple Model for Characterizing the Electrical Resistivity in $A-15$ Superconductors. *Phys. Rev. Lett.* **38**, 782 (1977).

[139] M. Gurvitch. Ioffe-Regel criterion and resistivity of metals. *Phys. Rev. B* **24**, 7404 (1981).

[140] M. Nakajima, S. Ishida, K. Kihou, Y. Tomioka, T. Ito, Y. Yoshida, C. H. Lee, H. Kito, A. Iyo, H. Eisaki, K. M. Kojima, and S. Uchida. Evolution of the optical spectrum with doping in $Ba(Fe_{1-x}Co_x)_2As_2$. *Phys. Rev. B* **81**, 104528 (2010).

[141] A. Sanna, F. Bernardini, G. Profeta, S. Sharma, J. K. Dewhurst, A. Lucarelli, L. Degiorgi, E. K. U. Gross, and S. Massidda. Theoretical investigation of optical conductivity in $Ba(Fe_{1-x}Co_x)_2As_2$. *Phys. Rev. B* **83**, 054502 (2011).

[142] A. Dusza, A. Lucarelli, F. Pfuner, J.-H. Chu, I. R. Fisher, and L. Degiorgi. Anisotropic charge dynamics in detwinned $Ba(Fe_{1-x}Co_x)_2As_2$. *Europhysics Letters* **93**, 37002 (2011).

[143] V. S. Popov. Imaginary-time method in quantum mechanics and field theory. *Physics of Atomic Nuclei* **68**, 686 (2005).

[144] A. Altland and B. Simons. *Condensed Matter Field Theory*. Cambridge University Press, Cambridge (2006).

[145] M. A. Lee and K. E. Schmidt. Green's Function Monte Carlo. *Computers in Physics* **6**, 192 (1992).

[146] S. Lederer. private communication.

[147] E. Kroumova, M. Aroyo, J. Perez-Mato, A. Kirov, C. Capillas, S. Ivantchev, and H. Wondratschek. Bilbao Crystallographic Server : Useful Databases and Tools for Phase-Transition Studies. *Phase Transitions* **76**, 155 (2003).

[148] U. Fano. Effects of Configuration Interaction on Intensities and Phase Shifts. *Phys. Rev.* **124**, 1866 (1961).

[149] S. Schippers. Analytical expression for the convolution of a Fano line profile with a gaussian. *Journal of Quantitative Spectroscopy and Radiative Transfer* **219**, 33 (2018).

[150] P. G. Klemens. Anharmonic Decay of Optical Phonons. *Phys. Rev.* **148**, 845 (1966).

[151] A. Baum, A. Milosavljević, N. Lazarević, M. M. Radonjić, B. Nikolić, M. Mitschek, Z. I. Maranloo, M. Šćepanović, M. Grujić-Brojčin, N. Stojilović, M. Opel, A. Wang, C. Petrovic, Z. V. Popović, and R. Hackl. Phonon anomalies in FeS. *Phys. Rev. B* **97**, 054306 (2018).

[152] W. Spengler, R. Kaiser, A. N. Christensen, and G. Müller-Vogt. Raman scattering, superconductivity, and phonon density of states of stoichiometric and nonstoichiometric TiN. *Phys. Rev. B* **17**, 1095 (1978).

[153] C. M. Varma, J. Zaanen, and K. Raghavachari. Superconductivity in the Fullerenes. *Science* **254**, 989 (1991).

[154] P. Zhou, K.-A. Wang, P. C. Eklund, G. Dresselhaus, and M. S. Dresselhaus. Raman-scattering study of the electron-phonon interaction in $M_3C_{60}$ (M=K,Rb). *Phys. Rev. B* **48**, 8412 (1993).

[155] J. Menéndez and M. Cardona. Temperature dependence of the first-order Raman scattering by phonons in Si, Ge, and $\alpha$-Sn: Anharmonic effects. *Phys. Rev. B* **29**, 2051 (1984).

[156] S. F. Wu, P. Richard, X. B. Wang, C. S. Lian, S. M. Nie, J. T. Wang, N. L. Wang, and H. Ding. Raman scattering investigation of the electron-phonon coupling in superconducting Nd(O,F)$BiS_2$. *Phys. Rev. B* **90**, 054519 (2014).

[157] W. L. McMillan. Transition Temperature of Strong-Coupled Superconductors. *Phys. Rev.* **167**, 331 (1968).

[158] P. B. Allen and R. C. Dynes. Transition temperature of strong-coupled superconductors reanalyzed. *Phys. Rev. B* **12**, 905 (1975).

[159] J. J. Lee, F. T. Schmitt, R. G. Moore, S. Johnston, Y.-T. Cui, W. Li, M. Yi, Z. K. Liu, M. Hashimoto, Y. Zhang, D. H. Lu, T. P. Devereaux, D.-H. Lee, and Z.-X. Shen. Interfacial mode coupling as the origin of the enhancement of $T_c$ in FeSe films on $SrTiO_3$. *Nature* **515**, 245 EP (2014).

[160] Y. He, M. Hashimoto, D. Song, S.-D. Chen, J. He, I. M. Vishik, B. Moritz, D.-H. Lee, N. Nagaosa, J. Zaanen, T. P. Devereaux, Y. Yoshida, H. Eisaki, D. H. Lu, and Z.-X. Shen. Rapid change of superconductivity and electron-phonon coupling through critical doping in Bi-2212. *Science* **362**, 62 (2018).

# List of publications

1. S. Lederer, **D. Jost**, T. Böhm, R. Hackl, E. Berg, S. Kivelson.
   Measuring the imaginary time dynamics of quantum materials.
   *arxiv: 1907.10182, submitted to Phys. Rev. B* (2019).

2. T. Böhm, F. Kretzschmar, A. Baum, M. Rehm, **D. Jost**, R. Hosseinian Ahangharnejhad, R. Thomale, C. Platt, T. A. Maier, W. Hanke, B. Moritz, T. P. Devereaux, D. J. Scalapino, S. Maiti, P. J. Hirschfeld, P. Adelmann, T. Wolf, Hai-Hu Wen, R. Hackl.
   Microscopic origin of Cooper pairing in the iron-based superconductor $Ba_{1-x}K_xFe_2As_2$.
   *npj Quantum Materials* **3**, 48 (2018).

3. A. Baum, Y. Li, M. Tomić, N. Lazarević, **D. Jost**, F. Löffler, B. Muschler, T. Böhm, J.-H. Chu, I. R. Fisher, R. Valentí, I. I. Mazin, R. Hackl.
   Interplay of lattice, electronic, and spin degrees of freedom in detwinned $BaFe_2As_2$: A Raman scattering study.
   *Phys. Rev. B* **98**, 075113 (2018).

4. **D. Jost**, J.-R. Scholz, U. Zweck, W. R. Meier, A. E. Böhmer, P. C. Canfield, N. Lazarević, R. Hackl.
   Indication of subdominant $d$-wave interaction in superconducting $CaKFe_4As_4$.
   *Phys. Rev. B* **98**, 020504(R) (2018).

5. N. Chelwani, D. Hoch, **D. Jost**, B. Botka, J.-R. Scholz, R. Richter, M. Theodoridou, F. Kretzschmar, T. Böhm, K. Kamarás, R. Hackl.
   Off-axis parabolic mirror optics for polarized Raman spectroscopy at low temperature.
   *Appl. Phys. Lett.* **110**, 193504 (2017).

6. T. Böhm, R. Hosseinian Ahangharnejhad, **D. Jost**, A. Baum, B. Muschler, F. Kretzschmar, P. Adelmann, T. Wolf, Hai-Hu Wen, I. R. Fisher, and R. Hackl.
   Superconductivity and fluctuations in $Ba_{1-p}K_pFe_2As_2$ and $Ba(Fe_{1-n}Co_n)_2As_2$.
   *physica status solidi (b)* **254**, 1600308 (2017).

7. F. Kretzschmar, T. Böhm, U. Karahasanović, B. Muschler, A. Baum, **D. Jost**, J. Schmalian, S. Caprara, M. Grilli, C. Di Castro, J. G. Analytis, J.-H. Chu, I. R. Fisher, and R. Hackl.
   Critical spin fluctuations and the origin of nematic order in $Ba(Fe_{1-x}Co_x)_2As_2$.
   *Nat. Phys.* **12**, 560-563 (2016).

# Acknowledgements

I want to thank

- **Professor Rudolf Gross** who provided support to secure my funding at the Friedrich-Ebert-Stiftung. I learnt quite a lot from minuting his exams, about physics and how to ask good questions.
- **PD Dr. Rudi Hackl** for introducing me to inelastic light scattering and to the many remarkable people I have had the pleasure to meet in the last few years.
- the **Friedrich-Ebert-Stiftung** for the funding through the doctoral scholarship.
- **Prof. Tom Devereaux** and his family for their hospitality during our visit at Stanford and enlightening discussions.
- **Prof. Steven A. Kivelson** for sharing his results prior to publication and for introducing me to the imaginary time formalism.
- **Dr. Samuel Lederer** for his patient explanations and the effective collaboration.
- **Dr. Brian Moritz** for his efforts to explain quantum Monte Carlo to me in an easy way, and the valuable after-conference activities.
- **Prof. Dietrich Einzel** whom I bothered with more than one question on several occasions and who found always time to answer them.

- **Prof. Paul Canfield**, **William R. Meier** and **Dr. Anna E. Böhmer** who provided the $CaKFe_4As_4$ crystals.
- **Prof. Ian Fisher**, **Johanna Palmstrom** and **Matthias Saneyuki Ikeda** who provided the $Ba(Fe_{1-x}Co_x)_2As_2$ crystals.
- **Dr. Stephan Geprägs** who never hesitated to grow a thin film to help us out and who had frequently a friendly ear for all my sorrows.
- **Dr. Andreas Baum**, **Dr. Thomas Böhm**, **Dr. Nenad Lazarević** and **Dr. Nitin Chelwani** for the discussions of a variety of lab-related and not-lab-related subjects, and particularly **Andi** for proofreading this thesis.
- **Dieter Guratzsch**, **Dr. Matthias Opel** and **Daniel Schwienbacher** for helping out with all the computer issues.
- **Emel Dönertas** for smoothing all the administrative hassle.
- **Sybilla Plöderl** and **Maria Botta** who were always very kind to me, even when I had a bad day.
- **Jan-Robin Scholz**, **Ulrike Zweck**, **Pablo Cova-Farina** and **Leander Peis** for doing the hard work in the lab and teaching me a lot about physics and myself. And **Jan** for proofreading the thesis not once, but twice!
- the "Helium-Halle", **Peter Binkert**, **Jan Naundorf** and **Harald Schwaiger**, for providing the cryogenics and assistance without much complication whenever it was necessary.
- **all the students** at the WMI for the relaxed and cooperative atmosphere.
- my **entire family**, particularly my mother and my siblings.
- **Janina** for her relentless patience and her enduring support. You never fail to amaze me.

So Long, and Thanks for All the Fish.